X-ray nanoprobe and electron beam investigations of kesterite and chalcogenide thin film solar cells

Dissertation

zur Erlangung des akademischen Grades
doctor rerum naturalium (Dr. rer. nat.)

vorgelegt dem Rat der Physikalisch-Astronomischen Fakultät der
Friedrich-Schiller-Universität Jena

von M.Sc. Maurizio Ritzer
geboren am 17.08.1992 in Gelnhausen

1. Gutachter: Prof. Dr. Carsten Ronning, Friedrich-Schiller-Universität Jena

2. Gutachter: Prof. Dr. Roland Scheer, Martin-Luther-Universität Halle-Wittenberg

3. Gutachterin: Prof. Dr. Susanne Siebentritt, Universität Luxemburg

Tag der Abgabe: 28.10.2020
Tag der Disputation: 22.02.2021

Zusammenfassung

Die Photovoltaik gilt als eine der zukunftsweisenden Technologien, um die fossilen Energieträger zu ersetzen und den Ausstoß von Treibhausgasen zu reduzieren. Der Großteil des Solarmarktes wird bis heute von Si-basierten Solarzellen abgedeckt, welche sich vor allem durch ihren hohen Wirkungsgrad auszeichnen. Allerdings ist die Herstellung mit einem sehr hohen Energie- und Materialeinsatz verbunden, was zu einer langsamen energetischen und wirtschaftlichen Amortisationszeit führt. Dies lenkte das Interesse auf Kesterit- und Chalkogenid-basierte Dünnschichtsolarzellen, welche diese Hindernisse überwinden und zusätzliche noch weitere Vorteile bieten, wie exzellente optische Eigenschaften und mechanische Flexibilität. In den letzten Jahrzehnten konnte der Wirkungsgrad dieser Solarzellen stetig gesteigert werden. Trotzdem ist dieser noch geringer als die theoretisch vorhergesagte Obergrenze. Dies wird insbesondere auf Inhomogenitäten in der Absorberzusammensetzung, strukturelle Defekte sowie der Bildung von Sekundärphasen zurückgeführt. Das Ziel dieser Arbeit ist es daher, Einblicke in Effizienz limitierende Eigenschaften hocheffizienter Kesterit- und Chalkogenid-basierter Dünnschichtsolarzellen zu erhalten, indem die lokale Zusammensetzung mit strukturellen, mikrostrukturellen und funktionalen Eigenschaften korreliert wird.

Eine Methode, Kesterit $Cu_2ZnSnSe_4$ (CZTSe) Absorber herzustellen, ist die Abscheidung von Cu, Zn und Sn Vorläuferschichten mittels Kathodenzerstäubung, welche beim anschließenden Erhitzen in Se Atmosphäre zu CZTSe reagieren. Kürzlich wurde gezeigt, dass sich Rekordeffizienzen durch die Abscheidung einer dünnen Ge Vorläuferschicht realisieren lassen. Insbesondere das Wachstum großer Körner mit einer außergewöhnlich homogenen Elementverteilung und die Abwesenheit schädlicher Cu-, Zn- oder Sn-basierten Sekundärphasen tragen zu dieser Effizienzsteigerung bei. Es ist vorteilhaft, dass diese Homogenität auch für die präferierten Cu armen und Zn reichen Wachstumsbedingungen erreicht werden. Lediglich die Grenzflächen zum Front- und Rückkontakt zeigen Variationen in der lokalen Zusammensetzung und werden als einer der Hauptfaktoren, die die Leistung begrenzen, identifiziert. Das abgeschiedene Ge wird innerhalb des Absorbers heterogen in die CZTSe Matrix eingebaut, verändert durch die geringe Konzentration die optischen und elektrischen Eigenschaften des Absorbers jedoch nur geringfügig. Neben dem Einbau in die CZTSe Kristallstruktur bildet es nanoskalige GeO_2 Sekundärphasen, die ungleichmäßig im Absorber verteilt

sind und sich vermutlich negativ auf die Effizienz auswirken.

Um die optischen Eigenschaften besser an das Spektrum der Sonne anzupassen, kann ein Teil des Selens durch Schwefel ersetzt werden. Hocheffiziente Kesterit $Cu_2ZnSn(S,Se)_4$ (CZTSSe) Dünnschichtsolarzellen mit einer Effizienz von bis zu 12.6 % werden häufig unter Verwendung von giftigem Hydrazin hergestellt. Eine Alternative bildet ein ungiftiger Ansatz, dessen Basis ein Wasser-Ethanol-Gemisch ist, in dem Cu-Zn-Sn-Sulfidkolloide gelöst sind. Dieses wird auf den Mo Rückkontakt gesprüht und in einer Se Atmosphäre erhitzt, was zur Bildung des CZTSSe Absorbers führt. Die Untersuchung der lokalen Zusammensetzung weist auf die Bildung schädlicher ZnS(Se) Sekundärphasen hin, deren Existenz, Anzahl und Dimension mit der Reduktion des Cu und der Erhöhung des Zn Gehalts stark zunimmt. Darüber hinaus zeigt die lokale Zusammensetzung der CZTSSe Phase starke Variationen innerhalb des Absorbers, die die Effizienz maßgeblich reduziert.

Unter den Dünnschichtsolarzellen ist Chalkogenid $Cu(In,Ga)Se_2$ (CIGS) mit einem Rekordwirkungsgrad von 23.35 % eines der effizientesten Materialsysteme. Durch die Nachbehandlung mit schweren Alkalimetallen wie Rb konnten in den letzten Jahren immer wieder neue Rekordeffizienzen erzielt werden. Schwere Alkalis agglomerieren insbesondere an den Grenzflächen zum Front- und Rückkontakt sowie an zufällig angeordneten Korngrenzen. Durch den simultanen Nachweis der lokalen Zusammensetzung und Funktionalität zeigt diese Arbeit, dass Rb-angereicherte Korngrenzen im Vergleich zu ihren benachbarten Körnern einen vernachlässigbaren Einfluss auf die Sammeleffizienz aufweisen, was auf die Passivierung schädlicher Defekte hinweist.

Abstract

Photovoltaics is considered as one of the most promising technologies for the replacement of fossil fuels and the reduction of greenhouse gas emissions. To date, the majority of the solar market is still covered by Si-based solar cells, which are characterized above all by their high efficiency. However, their production involves a very high energy and material expenditure, which leads to a slow energetic and economic payback time. This directed the interest to kesterite- and chalcogenide-based thin film solar cells, which overcome these obstacles and offer additional advantages like excellent optical properties and mechanical flexibility. Over the past decades, the efficiency of these solar cells has been steadily increased. Nevertheless, the efficiency is still below the theoretically predicted upper limit. This is mainly related to inhomogeneities in the absorber composition, structural defects, and the formation of secondary phases. The aim of this thesis is therefore to gain insights into efficiency-limiting properties of highly efficient kesterite- and chalcogenide-based thin film solar cells by correlating the local composition with structural, microstructural, and functional properties.

One technology to synthesize kesterite $Cu_2ZnSnSe_4$ (CZTSe) absorbers is the deposition of Cu, Zn and Sn precursor layers by sputtering, which react to CZTSe when subsequently heated in Se atmosphere. Recently, it was demonstrated that record efficiencies can be achieved by the deposition of a thin Ge precursor layer. Especially the growth of large grains with an exceptionally homogeneous element distribution and the absence of harmful Cu-, Zn- or Sn-based secondary phases contribute to this efficiency increase. This excellent homogeneity is even achieved for the preferred Cu-poor and Zn-rich growth conditions. Solely the interfaces to the front and back contact show variations in local composition and are identified as one of the main performance-limiting factors. Within the absorber, the deposited Ge is heterogeneously incorporated into the CZTSe matrix, but due to its low concentration, the optical and electrical properties of the absorber change only to a minor extent. In addition to the incorporation into the CZTSe crystal structure, it forms nanoscale GeO_2 secondary phases that are unevenly distributed throughout the absorber and have presumably a negative impact on the conversion efficiency.

To adjust the optical properties to the solar spectrum, selenium can be partially substituted by sulfur. Highly efficient kesterite $Cu_2ZnSn(S,Se)_4$ (CZTSSe) thin film solar cells with an efficiency of up to 12.6 % are often synthesized using a toxic hydrazine-based

process. An alternative approach is based on a non-toxic water-ethanol mixture in which Cu-Zn-Sn sulfide colloids are dissolved. This mixture is sprayed onto the Mo back contact and heated in a Se atmosphere, which leads to the formation of the CZTSSe absorber. Investigations of the local composition indicate the formation of harmful ZnS(Se) secondary phases whose presence, number and dimension increases strongly with the reduction of Cu and the increase of Zn content. Furthermore, the local composition of the CZTSSe phase shows strong variations within the absorber, which significantly reduces the efficiency.

Among all thin film solar cells, chalcogenide Cu(In,Ga)Se_2 (CIGS) is one of the most efficient material systems with a record power conversion efficiency of 23.35 %. In recent years, post-deposition treatments with heavy alkali metals like Rb have repeatedly enabled new record efficiencies. Heavy alkalis agglomerate especially at the interfaces to the front and back contact as well as at random grain boundaries. In a combinatorial approach, which simultaneously monitors the local composition and device functionality, this work demonstrates that Rb-enriched grain boundaries have a negligible influence on the collection efficiency compared to their neighboring grains, indicating the passivation of detrimental defects.

Contents

1. Introduction

The globalization and growing world population has lead to a constantly increasing energy consumption, which is predicted to grow by nearly 50 % until 2050 [1]. The current energy production is accompanied by the emission of greenhouse gases, which are one of the main causes for climate change and endangers life on earth. On December 12th 2015, nearly all nations of the world agreed to join an unprecedented alliance to save the planet, the Paris Agreement [2]. It envisages limiting the rise in the average temperature of the earth by 2040 to well below 2 °C, if possible to 1.5 °C, compared to the pre-industrial average temperature.[1] This can only be achieved by a substantial reduction in the emission of greenhouse gases, especially CO_2. From 2050, the plan intends to completely avoid emissions and thus the burning of fossil fuels. Despite specified goals, the combustion of oil, natural gas, and coal increased in the last years [3]. Even in 2019, CO_2 emission increased to about 36.8 Gt/year, which is an increase about 0.6 % compared to 2018 [4]. This trend is also reflected in the achievability of the targets, as most countries are already failing to meet their climate goal accompanied with an unsatisfactory forecast [5]. These worrying signs are particularly taken up by the younger generation and led to the global social movement "Fridays for Future" [6]. This movement has increased the awareness for the critical environmental situation and strengthened the demand for renewable energies.

Along with the social and political upheaval, scientists try to develop (cost-) efficient and emission free alternatives to fossil energy sources. Several models predict that the energy supply of the future has to be covered by different technologies, like solar-, water-, wind power, etc. [7–10]. However, most studies regard solar energy as one of the most promising resources [7–9]. This becomes apparent, when considering that already 90 minutes of the sun's energy reaching earth corresponds to today's annual global energy consumption [11].

One possibility to use the energy provided by the sun is the direct conversion into electricity using solar cells. With a share of about 95 %, Si-based solar cells are currently the most common on the market [12]. However, the production of these photovoltaic modules has decisive disadvantages, particularly in terms of highly energy-consuming and cost-intensive production [13]. A promising alternative are polycrystalline thin-film solar cells, which are not only characterized by their energy-efficient production but

---

[1] The pre-industrial average temperature is the value of 1750, i.e., 13.42 °C.

also by their low material expenditure [14–16]. Moreover, they provide mechanical flexibility and low weight [17–20] enabling novel application possibilities, such as building-integrated photovoltaic on curved surfaces or roof top application where Si solar cells are to heavy [21]. Especially $Cu(In,Ga)Se_2$ (CIGS) solar cells have gained great attention due to their non-toxic constituents and one of the highest efficiencies among all thin film devices, even outperforming polycrystalline Si cells [22]. Nevertheless, the efficiency is still well below the theoretically predicted Shockley–Queisser limit of about 33 % for a single junction solar cell [23, 24]. The recent breakthrough that boosted the conversion efficiency to 23.35 % [25] was achieved by applying heavy alkali-fluoride post deposition treatments (PDT), which especially improved the open voltage (V_{OC}) deficit [26]. Further optimization of these solar cells requires a deeper understanding on the effects of heavy alkali metals on the properties of the CIGS absorbers. In particular, the behavior of alkalis at the interfaces, especially at the grain boundaries, is of exceptional interest.

An emerging problem of CIGS is the limited availability of In and Ga in the earth crust [27, 28]. Proceeding from CIGS, Cu_2ZnSnS_4 (CZTS), $Cu_2ZnSnSe_4$ (CZTSe), and $Cu_2ZnSn(S,Se)_4$ (CZTSSe), so called kesterites, were derived by isoelectronic substitution of the rare elements by earth-abundant Zn and Sn [28]. Due to the similarities to CIGS and together with its earth-abundance and non-toxic constituents, kesterites are considered as a promising candidate to revolutionize the solar cell market. However, the current record efficiency is still limited to 12.6 % [29]. To narrow the efficiency-gap to other thin film solar cell materials and Si-based solar cells, a deep understanding of the martial properties that limit the conversion efficiency is indispensable.

In order to steadily promote the expansion and market potential of these emerging thin film solar cell materials, the power conversion efficiency has to be increased. Thus, three key challenges were identified and addressed within the scope of this thesis, in order to get a more comprehensive understanding of performance limiting properties in state-of-the-art CIGS, CZTSe, and CZTSSe thin film solar cells:

i. The composition of the absorber components as well as absorber inhomogeneities on different size scales affects the efficiency of thin film solar cell significantly [30–33]. These inhomogeneities include variations in local composition, structural defects such as grain boundaries but also secondary phases [30, 34–36]. The latter is often associated with a discrepancy between intended and realized absorber composition [35, 36]. Typically, the integral composition is probed, which obviously does not represent the complete picture of such complex material systems. A deeper understanding on the origin of efficiency-limiting properties in devices, however, requires to track the spatially resolved composition and phase. Typical methods to resolve the local composition in the nano- and subnanometer range like transmission electron microscopy energy-dispersive X-ray spectroscopy or electron energy loss spectroscopy are often limited to small sections [37–39]. Furthermore, applications such as atom probe tomography are destructive [40–43], which limits the use of complementary measurement methods. Techniques that overcome these limitations allow to get a comprehensive picture of the composition and their fluctuations in the absorber.

ii. The multivalent character of Sn in kesterite solar cells, with the ability to form +II and +IV oxidation states is expected to be one of the major obstacles, limiting the V_{OC} [44–46]. To overcome this limitation, CZTSe can be alloyed with Ge, which substitutes Sn and decreases the probability for Sn^{2+} states [47, 48]. However, it was recently demonstrated that adding even small amounts of Ge during the absorber synthesis strongly enhances the conversion efficiency by improving the V_{OC} [41, 49, 50]. In particular, the localization and distribution of Ge after the absorber growth, as well as possible effects on the efficiency, are required in order to get a more detailed understanding of the improvement.

iii. The positive impact on the morphology and electrical properties of Na that is provided during the growth of CIGS absorbers has drawn attention to alkali elements [51, 52]. It was quickly discovered that Na can improve the electrical properties of such devices, even when it is incorporated after the growth by PDT [53]. Consequently, the effects of heavier alkali elements were investigated. In recent years, particularly the addition of Rb and Cs has repeatedly enabled achieving record efficiencies [25, 54, 55]. Agglomerates of the heavy alkalies are especially formed at the front and back contact interfaces as well as at selected grain boundaries [56–62]. The effect of these accumulations, primarily in terms of grain boundary passivation, is controversially discussed [58, 63–65]. Gaining insights into the role of heavy alkalis at grain boundaries is therefore required to understand the improvement by PDTs.

Following this **introduction**, this thesis begins with an overview of the intrinsic properties of CIGS and the device structure of CIGS solar cells. **Chapter 2 - Fundamentals** also introduces the current knowledge of alkali metals in CIGS and possible explanations of the improved efficiency. This is followed by an introduction into the intrinsic properties of CZT(S,Se) as an absorber material for thin film solar cells and differences of the device structure compared to the CIGS counterpart. Furthermore, the current understanding of the effects of small amounts of Ge offered during growth of CZTSe is presented. Finally, this chapter introduces X-ray matter interaction. **Chapter 3 - Experimental Methods** briefly describes the experimental methods used within this thesis, including the sample preparation as well as the different characterization techniques. **Chapter 4 - Characterization of stoichiometric, homogeneous, single-phase $Cu_2ZnSnSe_4$** highlights the urgency to calibrate the performed measurements and points out the required experimental uncertainties. The following chapters focus on the three challenges, as identified before.

Chapter 5 - Germanium incorporation in homogeneous $Cu_2ZnSnSe_4$ solar cells investigates three Ge-doped solar cells with varying nominal compositions and different level of performance, which were prepared by a sequential process. It highlights the correlation of the local composition with the off-stoichiometry types and the different electrical device parameters. Furthermore, the spatially resolved Ge distribution is shown and correlated with the microstructure, giving access to possible performance-limiting features. Finally, the local environment of Ge is probed, giving access to the short-range structural order. Parts of the results were published in references [66–68].

In **Chapter 6 - Interplay of performance-limiting nanoscale features in $Cu_2ZnSn(S,Se)_4$ solar cells** three CZTSSe absorbers with different nominal compositions and level of performance, synthesized using a non-toxic spray coating process, are discussed. The interplay between the local composition and its variations in dependence of the nominal composition is revealed and the different performances are explained. Furthermore, the microstructure is correlated with variations in composition and their effects on efficiency. Consequently, conclusions can be drawn about the factors limiting the conversion efficiency in these devices. Parts of this chapter are published in reference [67].

Chapter 7 - Local electrical properties of Rb-enriched grain boundaries in $Cu(In,Ga)Se_2$ solar cells gains detailed insights into the local elemental distribution and functionality of a highly efficient CIGS solar cell subjected to a RbF-PDT. Variations in the composition can be identified, which have a beneficial effect on the collection efficiency. Furthermore, the passivation of random grain boundaries by Rb is discussed. Parts of this chapter are published in reference [69] and in the master's thesis of Christian Plass [70].

Chapter 8 - Conclusion and outlook summarizes the main results of this thesis with respect to the three challenges and an outlook to future work is given.

2. Fundamentals

This chapter summarizes fundamental properties of chalcogenide as well kesterite thin film solar cells and provides an introduction to X-ray matter interaction.

2.1. $Cu(In,Ga)Se_2$ thin film solar cells

The ternary semiconductor compound $Cu(In,Ga)Se_2$ has unique properties that enable its use as absorber material for thin film solar cells. CIGS is a direct semiconductor, accompanied with a very high absorption coefficient of $\sim 10^5\,\mathrm{cm}^{-1}$ [71, 72]. This allows efficient absorption of the solar spectrum already for layer thicknesses of only 1-2 µm, which translates into substantial material savings. Furthermore, such low thicknesses allow to produce mechanically flexible solar cells by utilizing substrates such as polymers, metal foils or ultra thin glasses in addition to the commonly used soda-lime glass [17–19]. Another advantage is the simplified manufacturing process and especially the lower growth temperature of polycrystalline CIGS compared to single crystalline silicon, which leads to an additional cost reduction [13]. The typical polycrystallinity does not automatically lead to significant losses, since grain boundaries in CIGS do not necessarily have a negative effect on the electrical properties [73, 74]. In addition to the already mentioned advantages, CIGS possesses long-term stability [16] and a short energy payback time [14, 15].

2.1.1. Crystal structure and properties of CIGS

The quaternary system CIGS crystallizes in the chalcopyrite structure (space group $I\bar{4}2d$), which is based on a tetragonal Bravais lattice. The primitive cell in figure 2.1 shows that every cation is surrounded by four anions and vice versa while both In and Ga share one lattice site. The anions occupy the Wyckoff position 4a and 4b for Cu and group III atoms, respectively, whereas Se is located at the 8d position.

Remarkably, the crystal structure of CIGS does not change for a wide range of off-stoichiometric compositions. Such deviations from the 1:1:2 (Cu:In/Ga:Se) proportion can be expressed by the Cu/(Ga+In) (CGI) and Ga/(Ga+In) (GGI) ratio.[1] Deviations

---

[1] Here, the cations denote the atomic concentrations, usually written as [Cu]/([Ga]+[In]) and [Ga]/([Ga]+[In]), but for reasons of readability the square brackets are omitted.

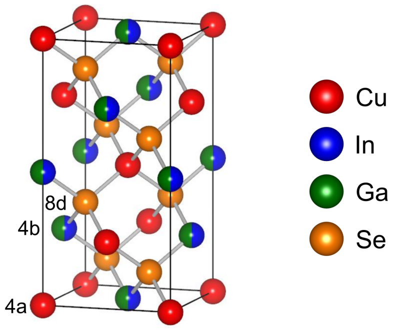

Figure 2.1.: Tetragonal unit cells of the chalcopyrite structure. Each anion is surrounded by four cations and vice versa. In and Ga share the same lattice site. Additionally, the Wyckoff positions are labeled.

from stoichiometry have a major impact on the electronic and optical properties. By changing the composition to Cu-rich conditions (CGI > 1), the charge carrier mobilities and lifetimes increase, but similar also interface and tunneling recombination, which yields to a very poor overall solar cell performance [75]. In contrast, Cu-poor conditions (CGI < 1) have reduced mobilities and lifetimes, but are currently the best choice for highly efficient thin film solar cells [25, 54, 55].

Another important property of $\mathrm{Cu(In_{1-x}Ga_x)Se_2}$ ($x \in [0, 1]$) is the tunable band gap in dependence on the GGI. Correspondingly, through a change of the gallium content x the band gap E_G can be adjusted from 1.04 eV for ternary $\mathrm{CuInSe_2}$ (CIS) to 1.68 eV for $\mathrm{CuGaSe_2}$ (CGS) [76, 77]. Thus, the band gap can be easily adjusted to the solar spectrum. The increase of the band gap is continuous, but not completely linear and can be described by:

$$E_G = (1-x)E_{G,CuInSe_2} + xE_{G,CuGaSe_2} - bx(1-x), \tag{2.1}$$

where b denotes the bowing parameter [78]. In literature, b varies between 0.11 and 0.24 [76, 79], but within this thesis 0.16 is assumed as recently reported [78].

2.1.2. Intrinsic point defects and defect complexes in CIGS

CIGS semiconductors have a complex defect structure with many possible point defects. These point defects can be ionized either by releasing an electron (donor) or by binding an electron (acceptor), which strongly affects the electronic properties [31]. The latter depend on the position within the bang gap. When the defect states are located close to the valence or conduction band, so called shallow defects, they have a small ionization energy ($\sim k_B T$) and are responsible for the doping of the material. Furthermore, their impact on the charge carrier recombination is low, since trapped electrons can be easily released. In contrast, deep defects have an ionization energy much higher than

$k_B T$ and do not contribute to the doping. Furthermore, trapped carriers cannot be released at moderate temperatures and recombine radiatively or non-radiatively via Shockley–Read–Hall (SRH) recombination [80, 81] either with an electron or hole, which is detrimental for solar cells. Thereby, the probability of recombination increases exponentially the closer the defect state is located to the center of the band gap [82].

The presence and number of defects strongly depend on their formation energy. The formation probability is influenced by the chemical potential [83] that is given by the growth conditions [84, 85] and thus by the CGI and GGI [86]. Within this thesis, only Cu-poor CIGS solar cells were investigated. Thus, this section gives a very brief introduction on defects for such conditions. According to the Kröger-Vink notation [87], defects are labeled as V_A (vacancy), A_i (interstitial), and A_B (anti-site). A and B denote random atoms in the crystal, V a vacancy and i an interstitial.

The defect with the lowest formation energy is the Cu vacancy (V_{Cu}), forming a shallow acceptor state. Due to the low ionization energy, it is associated with intrinsic p-type doping [86, 88, 89], which is observed for both CIS and CGS. In contrast, In-rich conditions yield to n-type conductivity for CIS [86, 90–92], due to the higher formation of In_{Cu} anti-site defects [93]. Thus, both compounds show intrinsic doping, which in turn makes external doping unnecessary. For the ternary CIGS compound the p-type conductivity is usually preferred, since in this case the minority charge carriers (electrons) have a higher mobility than the holes [94]. A more detailed overview about the defects in CIGS is given in references [86, 95].

Point defects can form defect complexes by Coulomb attraction between ionized donors and acceptors, when they are close enough to each other [86]. Due to the low formation energy of electrically neutral defect pairs, such as ($2V_{Cu}^{-}$ + In_{Cu}^{2+}), CIGS is considered as a self-compensated semiconductor. In consequence, slight variations of the stoichiometry barely influence the doping concentration. A detailed overview about the defect complexes is illustrated in references [86, 88, 96].

2.1.3. Device structure of CIGS solar cells

Highly efficient CIGS solar cells are typically produced in the substrate configuration. The cross-section with the typical layers is shown in figure 2.2. The most common substrate is soda-lime glass (SLG), which is both cheap and available in large quantities. It also has the advantage that sodium located in the glass can diffuse into the absorber at high temperatures during the synthesis [97–99] (see section 2.1.4).

A metallic back contact is sputtered on the substrate, which ideally forms an ohmic contact to the absorber. The transition metal Mo with a low specific resistivity of 10 to

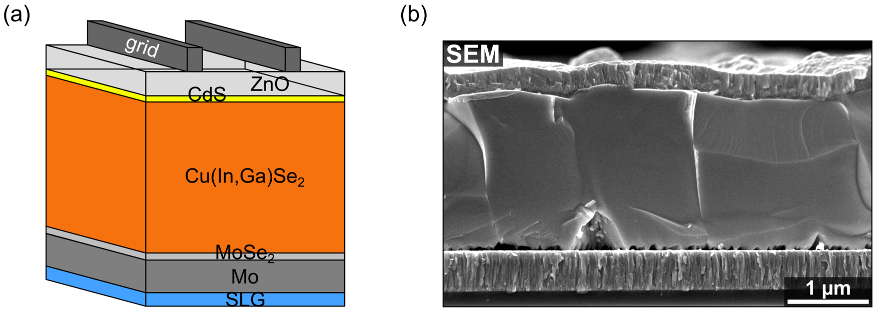

Figure 2.2.: Schematic illustration (a) and SEM image (b) of the cross-section of a CIGS solar cell. On top of the glass substrate a Mo back contact is deposited with a selenized interface to the absorber. The p-type CIGS absorber forms a hetero-junction with the n-type CdS layer and is contacted with an ZnO front contact as well as a metallic grid.

30 µΩcm [100], is well suited for this purpose. However, if Mo is in direct contact with CIGS, a Schottky barrier with a barrier height of 0.3 - 0.8 eV (for CIS) is created [101, 102]. This barrier is lowered by formation of a few 10 nm thick $MoSe_2$ layer during selenization and an ohmic contact forms [103–105].

The absorber layer follows on the back contact. Two processes have been established for absorber deposition: co-evaporation and the sequential process. Both processes are suitable for industrial applications and lead to very high efficiencies [55, 106]. Within this thesis the CIGS solar cell was produced by co-evaporation (for details see section 3.1.4). Briefly, the grown absorber itself is polycrystalline with grain sizes ranging from a few 100 nm to several µm, as a function of the Ga content [107]. The polycrystallinity naturally leads to the formation of grain boundaries. Here, it is necessary to distinguish between Σ3 twin grain boundaries and non-Σ3 grain boundaries (also called random grain boundaries). Σ3 twins are believed to be benign to the solar cell performance [33, 34, 108]. In contrast, random grain boundaries limit the conversion efficiency [33, 34, 108] due to the presence of defect states.

In Cu-poor absorbers a defect layer is formed at the surface of the absorber, which is Cu-depleted, so called ”ordered defect compound” (ODC) [109]. In this layer, the valence band shifts to a larger band gap [110, 111] and ensures that holes are transported away from the hetero-junction, which reduces the interface recombination and increases the open circuit voltage [112]. Besides the band gap widening, the conductivity is inverted and a buried p-n junction is formed [109].

Although the surface of the CIGS absorber already forms a p-n junction, a buffer layer is crucial to enhance the solar cell efficiency and to reduce interface recombination [113]. This layer should meet the following criteria:

- large band gap to minimize absorption losses [114],
- good lattice match and band alignment between absorber and front contact [114],

- creation of a sufficiently large depletion zone to reduce tunnel-assisted recombination at the interface to the absorber [115, 116],
- complete coverage of the absorber layer and high reproducibility [109, 115],
- low defect density at the buffer-absorber interface [114],
- passivation of interface states [109],
- protection of the absorber from subsequent sputtering of the front contact [116],
- and easily upscalable [114, 117].

Most solar cells are produced with a $\sim$ 50 nm thick n-type CdS buffer, since it possesses a large band gap of 2.4 eV and fulfills the previous mentioned criteria. It is usually deposited by chemical bath deposition (CBD) [54, 55, 73], as this process homogeneously deposits the buffer layer and additionally removes impurities from the absorber surface [114]. In addition, Cd diffuses into the absorber surface where it occupies the V_{Cu} and forms donors states, which additionally supports the n-type inversion of the CIGS surface [43, 118, 119]. At the same time, Cu diffuses into the buffer, which results in an increase in photoconductivity in the CdS layer [117]. Since Cd is very toxic, the search for alternatives is of great demand. Zn(O,S,OH) has recently gained great attention, since it showed the highest efficiencies for CIGS thin film photovoltaics [25] and is non-toxic. A comprehensive overview of alternative buffer as well as various deposition techniques can be found in reference [120].

The buffer layer is usually covered with n-type ZnO as a transparent conductive layer (TCO). It is optically transparent, due to the large band gap of approximately 3.20 - 3.40 eV [121]. ZnO is usually doped to increase the conductivity and to reduce ohmic losses. However, direct deposition of doped ZnO might short circuit regions which are not covered by the buffer layer [114]. Therefore, an intrinsic ZnO (i-ZnO) layer is deposited with a thickness of several 10 nm and a resistivity of $\sim 10^6\ \Omega$cm [122]. This isolates uncovered areas but does not significantly impede the vertical current transport. The carriers are further collected by Al doped ZnO (Al-ZnO), which has a specific electrical resistivity of $\sim$ 2 mΩcm [123].

Additional metallic grids are placed on the window layer to improve the current collection. They are optimized by an interplay of excellent collection and minimized shadowing of the underlying layers. To reduce the contact resistance, a system of two metallic layers is often used, such as nickel and aluminum [53]. Finally, an anti-reflection layer, such as MgF_2, can be evaporated to increase the efficiency.

2.1.4. Alkali elements in CIGS

It was discovered already in the 1990s that the electrical properties of CIGS solar cells could be significantly improved by the incorporation of alkali metals into the absorber [51, 52]. The greatest improvement in conductivity and charge carrier density was observed for Na, which directed the focus mainly on this alkali metal. In 2013 the CIGS community turned their focus on heavier alkali metals, since a solar cell with record efficiency was developed by applying a post-deposition treatment with KF after the absorber growth [53]. It soon became apparent that even higher efficiencies could be achieved using heavier alkali elements elements like Rb and Cs [25, 54, 55]. The exact origin of the improvement is not fully understood yet. Thus, in the following sections a brief literature overview summarizes the accepted models regarding alkali elements in CIGS.

Sodium

If sodium is offered during the growth of the absorber, either by diffusion from the glass substrate or by the deposition of a NaF layer on top of the Mo back contact, changes of the grain size were observed. Contradictory, there are reports on shrinking grain sizes [124, 125] and on increasing [125, 126] grain sizes. Furthermore, the grains tended to have the (112)-orientation [124, 126–128]. Besides morphological changes, it also lead to an improved conductivity [52, 129], open circuit voltage [97, 124, 126, 129–131], and fill factor [126, 130]. These electrical improvements were also observed for solar cells, where Na was supplied by a PDT [132]. This behavior was explained by the the fact that Na was mainly found at the surfaces and grain boundaries [133–135]. However, a small fraction of Na was also found in the grain interior, where it likely segregates at structural and point defects [42, 136].

Several suggestions were made to explain the improved performance. Theoretical calculations by Wei et al. [137] proposed that the formation of Na_{Cu} and Na_{In} anti-site defects are energetically favorable. While Na_{Cu} anti-sites are electrically inactive, Na_{In} forms a shallow acceptor state [138] and increases the hole density. This, might either result from the direct formation of Na_{In} [138] defects or from the substitution of In in In_{Cu} defects [52], which are always present under Cu-poor conditions. In principle, Na can also occupy the V_{Cu} vacancies but according to Wei et al. [137] it is energetically unfavorable. Furthermore, Na is predicted to passivate deep donor V_{Se} vacancies due to its ability to form atomic oxygen at the absorber surface [139], which can diffuse into the absorber [139], where it forms an O_{Se} shallow anti-site defect.

In contrast, Yuan et al. [140] proposed that the formation of Na_{In} anti-site defects are not favorable; whereas, in agreement with Wei et al., Na_{Cu} anti-site were found to be the most favorable point defect in Cu-poor CIS. This findings would automatically lead to a decreased conductivity, since the number of V_{Cu} vacancies decreases. To explain this contradiction, Yuan et al. [140] proposed a new model based on the equilibrium doping theory. Since the solubility of Na is significantly higher at elevated temperatures, it would diffuse out of the grains after cooling the sample to room temperature, due to the high diffusivity of Na [141, 142]. This effect might be enhanced by the wet chemical treatment after the absorber synthesis, which dissolves Na from the surface. Overall, this concept would explain the higher number of V_{Cu} vacancies and the improved conductivity.

Potassium

Potassium is commonly introduced by a KF-PDT, which is not affecting the absorber growth. Similar to the case of Na, most studies reported on an enhanced hole concentration by K [143–145], which has been ascribed by Yuan et al. [140] to a similar interaction of K with Cu as for Na. Furthermore, it is expected that K passivates intrinsic defects in the grain interior and at grain boundaries [65, 142, 145–148], which improves the carrier lifetime and the V_{OC} [65, 149, 150]. In contrast, Abou-Ras et al. [63] reported on an unchanged recombination velocity at grain boundaries based on electron beam induced current (EBIC) and cathodoluminescence (CL) measurements. Accordingly, the V_{OC} improvement would not be caused by defect passivation.

The surface was found to be Cu and Ga depleted after the KF-PDT [53, 151]. Indeed, it was also found that the position of the valence band maximum is lowered, while the conduction band minimum is raised [151]. In combination, this reduces the interface recombination [151–153]. Several works proposed that this observation can be explained by the formation of a KIn_xSe_y secondary phase [151, 154]. In addition to the surface secondary phase, enhanced Cd diffusion into the OCD layer was reported [53, 155, 156], which likely supports the n-type inversion. Finally, a thinner CdS layer can be grown after the KF-PDT treatment due to a modified surface topography, which reduced collection losses [53, 157].

Rubidium and Cesium

In recent years, record efficiencies were achieved by applying RbF- and CsF-PDTs [25, 54, 55]. The main breakthrough was attributed to a significantly improved V_{OC} [55, 158–161]. Schöppe et al. [56–58] used X-ray fluorescence analysis at the nano scale and found Rb and Cs segregations at Cu-poor random grain boundaries and at the interfaces to the front and back contact, while the concentration of heavy alkali elements was below the detection limit in the grain interior. Highly spatially-resolved atom probe tomography and transmission electron microscope measurements consolidate these findings for Rb [59–62]. Moreover, three dimensional time-of-flight secondary ion mass spectroscopy (TOF-SIMS) measurements also found only a very small fraction of Rb within the grains [62]. Based on density functional theory calculations [65, 162], it was proposed that light alkali elements can easily diffuse into stoichiometric and Cu-poor CIS, while heavy alkalis can only diffuse into Cu-poor CIS, which is in excellent agreement with the experimental findings. After a PDT the Na content was reduced at the grain boundaries, whereas an increased Na content in the grain interior was reported [59]. This was explained by a model in which heavy alkalis diffuse along the grain boundaries and displace the lighter Na into the grain interior [64]. At the grain boundary an energetically favorable $AInSe_2$ (A = Rb or Cs) secondary phase might form [162], which could passivate detrimental defects and lead to a hole barrier [58, 64]. In the other case point defects form, whose impact was investigated by Chugh et al. [65] and Schöppe et al. [58] using density functional theory (DFT) calculations. Compared to the alkali free reference, Na_{Cu}, Rb_{Cu}, Cs_{Cu}, and Cs_i defects showed a reduced density of states, which also indicates grain boundary passivation by alkalis. The density of states were even more reduced by the presence of heavy alkali metals likely because they compensate Se dangling bonds more effective due to the bigger size and lower electronegativity [65].

As already mentioned, alkali elements tend to segregate at the Cu depleted CdS/CIGS interface. In accordance to the KF-PDT, the formation of a $RbInSe_2$ secondary phase at the surface was confirmed by applying high resolution TEM measurements [60]. The impact of this secondary surface phases is controversially discussed in literature. $RbInSe_2$ might act as an electron barrier, which reduces the fill factor [163, 164]. In contrast, other studies proposed a reduced interface recombination velocity [60, 161], similar to the results for KF-PDTs. This apparent contradiction was explained by the fact that the beneficial effects of PDTs strongly depend on the CGI, which is not disclosed in most publications making a direct comparison of literature difficult [163]. Although the impact of the surface secondary phase is still not fully understood, the diode factor after the PDT improved. Similar to the results for KF-PDT, this was explained by a more homogeneous CdS coverage and thus, the possibility to grow thinner CdS buffer layers [157, 161, 165].

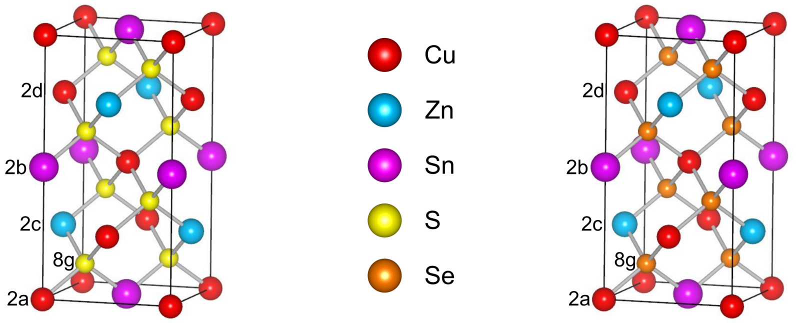

Figure 2.3.: Tetragonal unit cells of the sulfide- and selenide-based kesterite structure. Each anion is surrounded by four cations and vice versa. Additionally, the Wyckoff positions are labeled.

2.2. Kesterite thin film solar cells

According to the European Commission [166], In and Ga are classified as critical raw materials. Yet, In and Ga are key components in CIGS-based solar cells. As an alternative, the quaternary semiconductor compounds $Cu_2ZnSnSe_4$ and Cu_2ZnSnS_4 have gained great attention due to the earth-abundant constituents. These compounds have a direct band gap of 1.0 eV for CZTSe and 1.5 eV for CZTS, which can be tailored by the Se/(S+Se) ratio [167]. Due to the direct band gap and the associated very high absorption coefficient of over $10^4\,\mathrm{cm}^{-1}$ [168–170], the absorbers as well as the complete solar cells can be designed similar to the CIGS case.

2.2.1. Crystal structure of kesterite

CZTS and CZTSe crystallize in the kesterite structure (space group $I\bar{4}$), which is based on a tetragonal Bravais lattice. The cations Cu^+, Zn^{2+}, and Sn^{4+} are surrounded by four Se^{2-} or S^{2-} anions and vice versa, as shown in the primitive cell in figure 2.3. Cu is located at the origin on the Wyckoff position 2a and at the 2d position, Zn occupies the 2c position, while a Sn atom is located at the 2b position. The anions are located at the 8g position. Note that only the S-based structure is called kesterite. However, the Se-based compound crystallizes in the same structure; thus, it became established to name CZTS, CZTSe and its mixtures also ”kesterite”.

Kesterites are very challenging materials since small deviations from the 2:1:1:4 (Cu:Zn:Sn:S/Se) stoichiometry can easily result in detrimental secondary phases segregations [171, 172] (see also section 2.2.3). Similar to CIGS, deviations from stoichiometry are expressed by the cation ratios: Cu/(Zn+Sn) and Zn/Sn.[2] Despite the low phase stability of CZTSSe, the best solar cell efficiencies were achieved for Cu-poor (Cu/(Zn+Sn)

---

[2] Here, the cations denote the atomic concentrations, usually written as [Cu]/([Zn]+[Sn]) and [Zn]/[Sn], but for reasons of readability the square brackets are omitted.

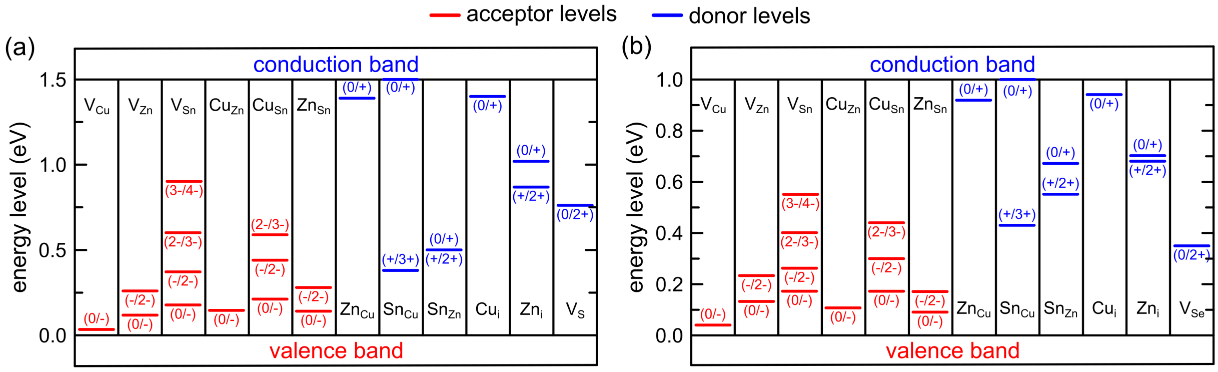

Figure 2.4.: Theoretically calculated intrinsic point defect energy levels within the band gap for CZTS (a) and CZTSe (b). The initial and final charge states are labeled in parentheses. (Drawings according to Chen et al. [32].)

< 1), Zn-rich (Zn/Sn > 1), and Sn-stoichiometric synthesis conditions [29, 50, 173–175]. In contrast Cu-rich and/or Zn-poor conditions showed poor efficiencies. The reasons will be elucidated in the following sections.

An additional advantage of kesterite is the tunable band gap. Varying the amount of S and Se increases the band gap from 1.0 eV for pure selenides to 1.5 eV for pure sulfides [167].

2.2.2. Intrinsic point defects and defect complexes in kesterite

In kesterites, a large number of point defects can occur due to the complex crystal structure. An overview of twelve possible point defects in CZTS and CZTSe, including the corresponding theoretically calculated defect energy levels by Chen et al. [32], is illustrated in figure 2.4. Anion-cation substitution as well as S_i, Se_i, and Sn_i interstitials were not considered here, as their formation is unlikely due to the valences or the atom sizes. Slightly different ionization energies were revealed in another theoretical study for some defects and especially no defect level within the band gap for a V_S vacancy in CZTS [176]. Cu_{Zn} anti-sites and V_{Cu} vacancies possess the lowest formation energies and are thus expected to be the most common ones [177, 178]. Both defects form an acceptor level and are believed to cause the observed intrinsic p-type doping of the material [32, 177–179]. Contrary, n-type doping is not observed at all, because donor defects have a higher formation energy than acceptors [180]. The remaining defects can be detrimental for the solar cell performance, as they form defect states within the band gap where charge carriers can recombine [32].

As introduced in section 2.2.1, Cu-poor conditions yield the highest solar cell efficiency, as explained by the higher formation probability of V_{Cu} vacancies and the improved p-type conductivity [32]. However, for Cu-rich conditions the Cu_{Zn} anti-sites and hole

concentration is even higher, which should result in an even better performance. To understand this contradiction, the defect complexes have to be analyzed.
As already introduced in section 2.1.2, defects can form complexes by Coulomb attraction [86]. In kesterite, such defect complexes have significantly lower formation energies than independent point defects and appear in much larger numbers. Accordingly, kesterites are also considered as self-compensated semiconductor [32, 179]. This can be advantageous in the case of deep defects since they self-compensate each other and might not impact the electronic and optical properties of kesterite. Chen et al. [32] calculated the formation energy and impact on the band gap of different defect clusters. They showed that the most abundant complexes in stochiometric kesterite is the ($\mathrm{Cu}_{\mathrm{Zn}}^{-}$ + $\mathrm{Zn}_{\mathrm{Cu}}^{+}$) complex. The impact on the band edges is very weak and can be expected to be benign. However, other defect clusters, such as ($2\mathrm{Cu}_{\mathrm{Zn}}^{-}$ + $\mathrm{Sn}_{\mathrm{Zn}}^{2+}$), ($\mathrm{Cu}_{\mathrm{Sn}}^{-}$ + $\mathrm{Sn}_{\mathrm{Cu}}^{+}$) or ($\mathrm{Zn}_{\mathrm{Sn}}^{2-}$ + $\mathrm{Sn}_{\mathrm{Zn}}^{2+}$) complexes, have a detrimental impact on the device performance since they decrease the valence and conduction band and might trap charge carriers. The formation energy for most detrimental defect complexes is very high in stoichiometric kesterite, except for the ($2\mathrm{Cu}_{\mathrm{Zn}}^{-}$ + $\mathrm{Sn}_{\mathrm{Zn}}^{2+}$) complex. Changing the conditions to Cu-poor and Zn-rich, ($\mathrm{V}_{\mathrm{Cu}}^{-}$ + $\mathrm{Zn}_{\mathrm{Cu}}^{+}$) and ($\mathrm{Zn}_{\mathrm{Sn}}^{2-}$ + $2\mathrm{Zn}_{\mathrm{Cu}}^{+}$) become the dominant complexes. Their impact on the band edges is very low as well and the device efficiency will not be influenced. In contrast, Cu-rich, Zn-poor, and/or Sn-rich conditions lead to an exponential increase of ($2\mathrm{Cu}_{\mathrm{Zn}}^{-}$ + $\mathrm{Sn}_{\mathrm{Zn}}^{2+}$) complexes. The detrimental impact of this defect cluster is much higher than the improved conductivity by $\mathrm{Cu}_{\mathrm{Zn}}$ defects and the reduced free carrier density by the Zn enrichment, which explains the preferred synthesis conditions [32]. A detailed overview about the defect complexes and their influence on the device properties is illustrated in reference [32].

2.2.3. Off-stoichiometry types and secondary phases in kesterite

The phase diagrams of the quasi-ternary $\mathrm{Cu_2S}$-ZnS-$\mathrm{SnS_2}$ and $\mathrm{Cu_2Se}$-ZnSe-$\mathrm{SnSe_2}$ system indicates that single phase kesterite can only exist in a very narrow compositional region [171, 172]. Deviations from stoichiometry, i.e., $\mathrm{Cu/(Zn+Sn)} \neq 1$ and $\mathrm{Zn/Sn} \neq 1$, result in secondary phases. Experimentally, however, it was proved that kesterite tolerate deviations from stoichiometry while maintaining the kesterite structure [182–185]. Keeping constant charge balance and valence state, so called ”off-stoichiometry types” were proposed, referred to A-L [36, 184, 186, 187]. These off-stoichiometry types are inherently connected to certain point defects (see table 2.1) and defect complexes addressed in the previous section. Thereby, the amount of defects correlates with the degree of off-stoichiometry [181]. Nevertheless, kesterite also showed limits regarding

Table 2.1.: Overview of the off-stoichiometry types in kesterite. (Table according to Schorr et al. [181].)

sample	composition	cation substitution reaction	intrinsic point defect
A	Cu-poor, Zn-rich, Sn-const.	$2Cu^{+} \rightarrow Zn^{2+}$	$V_{Cu} + Zn^{2+}_{Cu}$
B	Cu-poor, Zn-rich, Sn-poor	$2Cu^{+} + Sn^{4+} \rightarrow 3Zn^{2+}$	$2Zn^{2+}_{Cu} + Zn^{2+}_{Sn}$
C	Cu-rich, Zn-poor, Sn-rich	$3Zn^{2+} \rightarrow 2Cu^{+} + Sn^{4+}$	$2Cu^{+}_{Zn} + Sn^{4+}_{Zn}$
D	Cu-rich, Zn-poor, Sn-const.	$Zn^{2+} \rightarrow 2Cu^{+}$	$Cu^{+}_{Zn} + Cu_{i}$
E	Cu-poor, Zn-poor, Sn-rich	$2Cu^{+} + Zn^{2+} \rightarrow Sn^{4+}$	$2V_{Cu} + Zn^{2+}_{Sn}$ or $Sn^{4+}_{Cu} + V_{Cu} + V_{Zn}$
F	Cu-rich, Zn-rich, Sn-poor	$Sn^{4+} \rightarrow Zn^{2+} + 2Cu^{+}$	$2Zn^{2+}_{Sn} + 2Cu_{i}$ or $Cu^{+}_{Sn} + Cu_{i} + Zn^{2+}_{i}$
G	Cu-const., Zn-rich, Sn-poor	$Sn^{4+} \rightarrow 2Zn^{2+}$	$Zn^{2+}_{Sn} + Zn^{2+}_{i}$
H	Cu-const., Zn-poor, Sn-rich	$2Zn^{2+} \rightarrow Sn^{4+}$	$Sn^{4+}_{Zn} + V_{Zn}$
I	Cu-rich, Zn-const., Sn-poor	$Sn^{+} \rightarrow 4Cu^{+}$	$Cu^{+}_{Sn} + 3Cu^{+}_{i}$
J	Cu-poor, Zn-const., Sn-rich	$4Cu^{+} \rightarrow Sn^{4+}$	$Sn^{4+}_{Cu} + 3V_{Cu}$
K	Cu-rich, Zn/Sn = 1 = const.	$Zn^{2+} + Sn^{4+} \rightarrow 6Cu^{+}$	$Cu^{+}_{Zn} + Cu^{+}_{Sn} + 4Cu^{+}_{i}$
L	Cu-poor, Zn/Sn = 1 = const.	$6Cu^{+} \rightarrow Zn^{2+} + Sn^{4+}$	$Zn^{2+}_{Cu} + Sn^{4+}_{Cu}$

this off-stoichiometry of $0.6 \leq Cu/(Zn+Sn) \leq 1.7$ and $0.5 \leq Zn/Sn \leq 1.6$ [185]. Outside these boundaries, binary or ternary sulfur/selenide secondary phases will always occur [185]. An overview is presented in reference [181]. In general, a non-uniform phase is considered as detrimental, because it might enhance the recombination, increase the series resistance, and/or lower the band gap [188, 189].

2.2.4. Device structure of kesterite solar cells

The design of kesterite thin film solar cells is adopted from the typical layer structure of CIGS thin film solar cells. Therefore, this section will only deal with some small differences.

The CZT(S,Se) absorber layer is deposited on the back contact as well. In contrast to CIGS, where the sequential and co-evaporation process are established, especially with regard to industrial applications, there is no established process for kesterite. An overview of the technologies is given in reference [190]. Within this thesis, a sequential as well as a non-toxic wet chemical process was used to produce the absorbers (see section 3.1.2 and 3.1.3). Afterwards, the CdS buffer with a thickness of $\sim 50\,\mathrm{nm}$ is deposited by CBD. There are also approaches to use alternative buffer layers like Zn(O,S) [191], (Zn,Mg)O [192], or Al_2O_3 [193] to avoid Cd, but until now most of them yield a reduced solar cell efficiency. Subsequently, a roughly 400 µm double window layer is deposited by sputtering an i-ZnO and n-type In_2O_3-SnO_2 (ITO) layer with an optical band gap of around 3.5 - 4 eV [194, 195]. In fact, ITO is not ideal and only reasonable in laboratory scale because In was classified as critical raw materials [166].

Nevertheless, ITO showed the best conversion efficiency [29] since it has a higher mobility and a resistivity below $\sim 0.2\,\mathrm{m\Omega cm}$ [196–198].

2.2.5. Germanium in kestrite

In recent years, Germanium alloying of kesterite absorbers has received great attention in the community, even though Ge is also classified as critical raw material [166]. Germanium is a group IV element and is therefore capable to replace Sn in the lattice, which is connected to several advantages. Compared to Sn, Ge has a more stable oxidation state of +4 [47] and can avoid the presence of detrimental +2 states [44–46]. Furthermore, Ge can tune the band gap from 1.0 up to 2.25 eV in $Cu_2Zn(Sn_{1\text{-}x}Ge_x)(S_{1\text{-}y},Se_y)_4$ [199–202]. Devices prepared by an optimized Ge concentration in the order of 5 at.% revealed an improved V_{OC}, caused by reduced carrier recombination and higher minority carrier lifetimes [48, 203, 204]. This led to a record efficiency of 12.3 % [205] only slightly below 12.6 % for CZTSSe [29].
Recently, Giraldo et al. [41] showed that even small quantities of Ge (< 0.5 at.%), added as a superficial layer on top or as profound layer below the precursor during the sequential process of CZTSe, lead to a remarkable increase of the efficiency. In particular the V_{OC}, fill factor, and the minority carrier life-time significantly improved. An optimized synthesis routine yields the record conversion efficiency of 11.8 % for selenide-based kesterite [50]. The underlying mechanism of this improvement is still under debate, thus, in the following, a brief introduction of the current knowledge is presented.

Absorber synthesis without Ge

During the absorber growth, Giraldo et al. [50] observed Cu out-diffusion towards the surface, while Zn segregates at the back contact. Voids form at the back contact likely due to the high formation probability of binary volatile Sn–Se species, which also explain Sn losses after the synthesis. Furthermore, binary selenide compounds form, which react to CZTSe by following a tri-molecular reaction mechanism:

$$Cu_2Se_{(s)} + SnSe_{(s)} + ZnSe_{(s)} + \frac{1}{2}Se_{2(g)} \xrightarrow{T\sim 400\,^\circ C} Cu_2ZnSnSe_{4(s)}.$$

Here (s) and (g) denote the solid and gas phase, respectively. After the growth, the absorber showed a bi-layered structure with large, less Cu-poor grains close to the surface and smaller, less Cu-poor ones at the bottom. This can be explained by the Cu diffusion prior to the kesterite formation.

Absorber synthesis with Ge

When small amounts of Ge are added during the growth process [50], the previous observed Cu out-diffusion is prevented. Remarkably, Cu and Sn intermix from the very beginning, which also suppresses the uncontrolled Sn-loss. The latter is also directly reflected in the morphology. Ge-containing samples have significantly less voids and uniform grains extending from the back contact to the surface. However, when the Ge concentration exceeds a critical value, the efficiency drastically decreases again because “dome”-like features develop. Thus, a precise control of the Ge content is of great demand. Furthermore, the pathway for the kesterite formation changed drastically. Giraldo et al. [50] proposed the following new bi-molecular process, which does not involve a Sn-Se phase and likely explain the improved growth.
In the first step, a Cu_6Sn_5 phase forms, which decompose as follows:

$$\mathrm{Cu_6Sn_5(s)} \xrightarrow{\mathrm{T}\sim 400\,^\circ\mathrm{C}} 2\mathrm{Cu_3Sn_{(s)}} + 3\mathrm{Sn_{(l)}},$$

with (l) as liquid phase. Subsequently, a ternary and binary phase forms:

$$\mathrm{Cu_3Sn_{(s)}} + \frac{5}{2}\mathrm{Se_{2(g)}} \rightarrow \mathrm{Cu_2SnSe_{3(s)}} + \mathrm{CuSe_{2(s)}}.$$

Finally, kesterite forms by:

$$\mathrm{Cu_2SnSe_{3(s)}} + \mathrm{ZnSe_{(s)}} \rightarrow \mathrm{Cu_2ZnSnSe_{4(s)}}.$$

The reaming $CuSe_{2(s)}$ reacts with elemental $Sn_{(s)}$ as follows:

$$2\mathrm{CuSe_{2(s)}} + \mathrm{Sn_{(s)}} \rightarrow \mathrm{Cu_2SnSe_{3(s)}} + \frac{1}{2}\mathrm{Se_{2(g)}}.$$

Subsequently the ternary compound forms kesterite, as previously shown.
Two models were proposed on the role of Ge during the synthesis and how it assists the formation of the ternary phase and enlarged grains. In the first model [50], Giraldo et al. suggest that Ge enhances the solubility limit of Sn in Cu phases, which facilitates the formation of Cu-Sn-Se phases and therefore the crystallization. The second mechanism [50] implies the formation of a liquid Ge–Se phase, which acts as a flux agent for the formation of the ternary Cu–Sn–Se and quaternary Cu–Zn–Sn–Se phases. Due to the small amounts of Ge, the detection and localization is fairly difficult. Thus, it is challenging to estimation, which of the two hypotheses are correct.
Furthermore, Giraldo et al. [50] observed an strong interrelation between the doping

concentration, which drastically decreases when the Ge quantity exceeds a certain amount. TOF-SIMS profiles indicated a reduced sodium content within the absorber. Na diffuses from the soda-lime glass into the absorber during the growth and is expected to act similar like in CIGS [206]. Energy-dispersive X-ray spectroscopy measurements showed for high Ge quantities that Na is extracted to the surface of the absorber, where it forms $\mathrm{Na_xO_y}$ precipitates. This behavior can likely be explained by the presence of $\mathrm{GeO_x}$ nanoclusters, which form because of the short air exposure during the synthesis. It is well known that oxygen attracts Na [207] explaining the diffusion to the surface. However, it is unclear why these $\mathrm{Na_xO_y}$ clusters only form when the Ge concentration exceeds a certain value.

2.3. X-ray matter interaction

The interaction of X-rays and matter includes four different effects. Elastic (Rayleigh) and inelastic (Compton) scattering describe the scattering of a photon at electrons [208]. Additionally, if the X-ray energy exceeds the binding energy of the electrons, an electron can be ionized (photo-ionization). Finally, pair production describes the formation of an electron positron pair (particle-antiparticle process) from a photon, whose energy is two times bigger than two times the rest energy of an electron (511 keV). However, the latter effect is not relevant in respect to this thesis, as the maximum X-ray energy was 29.6 keV.

2.3.1. X-ray fluorescence spectroscopy (XRF)

If an X-ray whose energy is at least equal to the electron's binding energy of an atom hits the respective material, the photon is absorbed and the electron is lifted into the continuum (figure 2.5a). The ionized atom pursues for an energetically more favorable state, which leads to a transition of an electron from a higher shell occupying the resulting vacancy. A X-ray is emitted, with an energy equal to the energy difference between the states involved. Therefore, the emitted energy of the X-ray radiation is characteristic for each element. An analysis of the characteristic radiation of a sample therefore allows conclusions about its composition. This principle is used for X-ray fluorescence spectroscopy (XRF).

Exciting a homogeneous, flat sample with a monochromatic X-ray beam with an energy E_0 at an angle of incidence θ_{in} to the sample surface and an initial intensity I_0, the intensity of the created fluorescence radiation $I_i(E_i)$ emitted at the angle θ_{out} to the

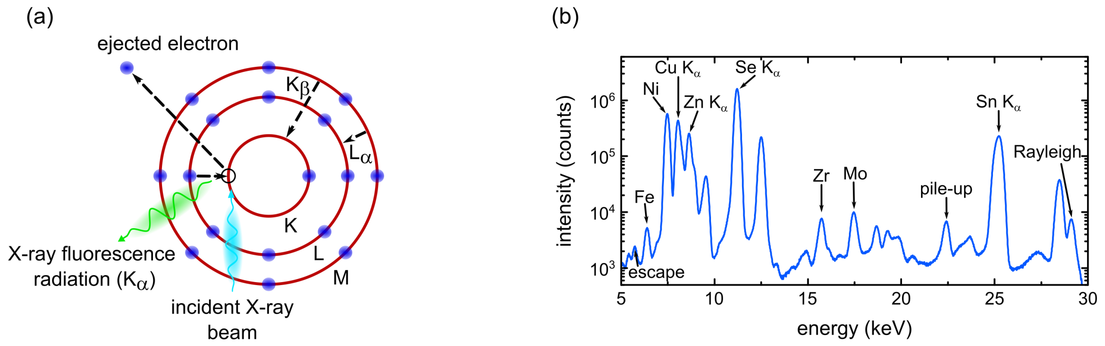

Figure 2.5.: (a) Principle of XRF. The hard X-ray beam excites an electron from the K-shell and lifts it to continuum. An electron from the outer shell occupies the resulting vacancy by emitting X-ray fluorescence radiation, in this case K_α radiation. (b) XRF spectrum taken on a CZTSe lamella with an incident X-ray beam energy of 29.6 keV.

sample surface is given according to van Grieken at al. [209] by:

$$I_i(E_i) = I_0 \frac{G}{sin(\theta_{in})} \varepsilon(E_i) a_i(E_0) \cdot \frac{1 - exp\left[\rho d \left(\frac{\mu(E_0)}{sin(\theta_{in})} + \frac{\mu(E_i)}{sin(\theta_{out})}\right)\right]}{\frac{\mu(E_0)}{sin(\theta_{in})} + \frac{\mu(E_i)}{sin(\theta_{out})}}. \tag{2.2}$$

Here, ε denotes the detector efficiency and G the detector geometry. Both the intensity of the incident beam and the characteristic radiation is attenuated in the sample, which is considered in the second part of equation 2.2. The sample thickness is described by d, while ρ is the sample density, and $\eta(E_0)$ and $\eta(E_i)$ are the mass attenuation coefficients including absorption and scattering within the sample. All fundamental parameters related to the emission of the characteristic X-rays of the i-th element are included in the factor $a_i(E_0)$ [209]:

$$a_i(E_0) = w_i \tau_i(E_0) \omega_i p_i \left(1 - \frac{1}{j_i}\right). \tag{2.3}$$

Hereby, the mass fraction of the i-th element is given by w_i and the total mass photoelectric absorption coefficient of the i-th element at energy E_0 by $\tau_i(E_0)$. Furthermore, p_i gives the relative fraction of the total emitted photon intensity of the considered transition. The ratio between the absorption coefficient with the absorption edge and the absorption coefficient without the absorption edge at energy E_0 is described by j_i. Moreover, ω_i describes the fluorescence yield, which equals the ratio between the number of emitted characteristic X-rays and the number of created vacancies. Thus, ω_i takes the competing Auger effect into account, which describes a non-radiative process where the created fluorescence photon excites an electron of an outer shell that leaves the atom. According to reference [210], the fluorescence yield ω_i can be approximated by $\omega = Z^4/(K + Z^4)$ with atomic number Z and a constant K. Thus, the ratio between radiative and non-radiative emission increases for higher atomic numbers [210].

A typical XRF spectrum, taken on a CZTSe lamella, is shown in figure 2.5b. It consists of the characteristic fluorescence lines on top of a continuous background. In addition, at the highest-energy of the spectrum ($\approx 29.6\,\mathrm{keV}$) the elastically scattered primary beam (Rayleigh peak) can be identified. Furthermore, two effects contribute to the spectrum. Pile-up peaks arise when the detector detects two or more photons simultaneously and interprets them as a single one with the summed energy of the photons involved. Escape peaks, however, are generated when the K-shell of the detector material is excited. The created K-line photon leaves the detector while the created photon releases the energy in the detector. Thus, the detected energy is reduced by the binding energy of the detector material K-shell. In this thesis, silicon-based detectors were used. As a result, escape lines, which are shifted by the Si K-line ($1.74\,\mathrm{keV}$) towards smaller energies of the corresponding main line appear in the spectrum.

The XRF spectrum in figure 2.5b can be evaluated by fitting the individual peaks using Gaussian functions. The mass fraction w of an individual element is then determined by [211]:

$$A = I_0 w \frac{\Omega}{4\pi} \sum_j R'_j, \tag{2.4}$$

where A denotes the peak area, Ω the solid angle of the detector, I_0 the intensity of the incident beam, and R'_J the relative intensity.

More details about XRF and the data evaluation can be found in reference [209–211]. The fluorescence energies of the individual elements used in this thesis are summarized in the X-ray data booklet [212].

2.3.2. X-ray absorption near-edge structure spectroscopy (XANES)

If a X-ray with intensity I_0 and energy E encounters a material with thickness d, only an extend of the X-rays is transmitted. The Lambert–Beer law proposes that the transmitted intensity $I(d)$ is [213]:

$$I(d) = I_0 \cdot exp\left[-\mu(E)d\right], \tag{2.5}$$

where $\mu(E)$ is the energy dependent X-ray absorption coefficient. For most energies the absorption coefficient is a smooth function, which decreases with increasing photon energy and can be approximated by [213]:

$$\mu(E) = \frac{\rho Z^4}{AE^3}. \tag{2.6}$$

Here, ρ denotes the sample density, Z the atomic number, and A the atomic mass. However, if the X-ray energy equals or exceeds the electron's binding energy, $\mu(E)$ sharply increases. X-ray absorption near-edge structure spectroscopy (XANES) probes the energy dependence of $\mu(E)$ below, at, and above the electron binding energy for a specific shell of an atom [208, 213, 214]. Since each element has a distinct absorption edge energy, this technique is sensitive to atomic species [208, 213, 214]. Furthermore, $\mu(E)$ depends on the oxidation state. In a neutral atom, the positive charges of the core are screened by the negatively charged electrons. However, the shielding effect for atoms of higher oxidation state (i.e., with a reduced number of electrons) changes, causing slightly lowered energy states of the remaining electrons and an increase of the absorption edge energy [208]. In consequence, XANES is also sensitive to the short-range structural order, in which the examined atom is located [208]. Detailed information about this technique is given in reference [208, 213, 214].

2.3.3. X-ray beam induced current (XBIC)

In X-ray beam induced current (XBIC) measurements, a hard X-ray excites core-level electrons. Through the Auger or XRF process, electrons from shallower levels immediately fill the created core-hole [215]. The created highly energetic photo- and Auger electrons lose energy through inelastic scattering (thermalization), thus creating secondary electrons in their traces [215, 216]. In semiconductors, the hot electrons and holes thermalize to the conduction and valence band, respectively [215, 217]. When these processes appear in a p-n junction, the electron-hole pairs are separated and produce a current [215, 218], which can be measured. This signal is influenced by the device properties, such as defect states leading to an enhanced recombination and a reduced current signal [215, 218–220].

2.3.4. X-ray collection efficiency (XCE)

The created XBIC current signal is also influenced by thickness variations and compositional dependent electron-hole pair generation efficiencies. An approach to correct for these effects is the calculation of the collection efficiency (CE), as described by

Stuckelberger et al. [217]:

$$CE = \frac{N^{coll}_{e^-/h^+}}{N^{gen}_{e^-/h^+}}. \tag{2.7}$$

Here, $N^{coll}_{e^-/h^+}$ is the number of collected electron-hole pairs, whereas $N^{gen}_{e^-/h^+}$ is the number of generated pairs.

In this thesis, the p-n junction is represented by a solar cell. An approach to describe the charge carrier collection efficiency for solar cells is the measurement of the external (EQE) and internal quantum efficiency (IQE) known as:

$$EQE = \frac{N^{coll}_{e^-/h^+}}{N^{in}_{ph}} \quad \text{and} \quad IQE = \frac{N^{coll}_{e^-/h^+}}{N^{abs}_{ph}}, \tag{2.8}$$

where N^{in}_{ph} is the number of incident photons and N^{abs}_{ph} the number of absorbed photons. For low energetic photons, as used for photovoltaics applications, it can be assumed that only one electron-hole pair is produced per incident photon ($N^{coll}_{e^-/h^+} \approx N^{abs}_{ph}$). Furthermore, the transmission for solar cells is negligible and the absorption A ($A = 1 - R$) is only influenced by the reflectivity R. Taking both effects into account, the CE can be approximated by:

$$CE \approx \frac{N^{coll}_{e^-/h^+}}{N^{abs}_{ph}} = IQE = \frac{EQE}{1-R}. \tag{2.9}$$

For X-ray-based investigation, the previously described assumptions are not valid, since an absorbed photon creates several electrons and a significant fraction of the incident photons is transmitted. In order to include this issue, the CE can be corrected by a factor C and now expresses the "XCE", which is determined as:

$$XCE = \frac{N^{coll}_{e^-/h^+}}{N^{gen}_{e^-/h^+}} = \frac{N^{coll}_{e^-/h^+}}{C \cdot N^{in}_{ph}}. \tag{2.10}$$

In this case, $N^{coll}_{e^-/h^+}$ describes the XBIC signal and N^{in}_{ph} the measured photon flux of the synchrotron X-ray beam. C denotes the ratio of generated electron-hole pairs per incident X-ray photon:

$$C \approx \frac{E_{abs} E_g}{E_{ion} E_{ph}}. \tag{2.11}$$

Here, E_{abs} denotes the deposited energy in the absorber layer per incident photon with the known energy E_{ph}, E_g the band gap of the absorber, and E_{ion} the ionization energy. The band gap of every position can simply be calculated by equation 2.1 using the local composition evaluated from nano-XRF. Furthermore, E_{ion} can be determined using the empirical formula from reference [221]:

$$E_{ion} = \frac{14}{5}E_g + 0.5eV. \tag{2.12}$$

To determine E_{abs} is more complex, since in a multilayered device, such as CIGS solar cells, the incident flux I_0 reaching the absorber is inhomogeneously attenuated by the front contact layers. Furthermore, compositional dependent absorption probabilities and thickness variations influence E_{abs} as well. Thus, West et al. [222] introduced a simple correction that takes the attenuation into account. This equation is given by:

$$\frac{I}{I_0} = \frac{1}{T}\sum_{N=1}^{T} exp\left[\sum_{i=1}^{N} \frac{-\mu_{in}(t_i)}{cos(\theta_{in})}\Delta t_i + \frac{-\mu_{out}(t_i)}{cos(\theta_{out})}\Delta t_i\right], \tag{2.13}$$

where I is the transmitted flux, T is the number of layers, Δt_i is the thickness of each layer, and $\mu_{in}(t_i)$ and $\mu_{out}(t_i)$ are the attenuation coefficients of the incident beam and the created fluorescence radiation at a depth t_i. The incident beam angle and detection angle relative to the surface normal are given by θ_{in} and θ_{out}, respectively. By calculating the fraction which reaches the absorber I_r and is transmitted through I_t, E_{abs} can be calculated by:

$$E_{abs} = \frac{(I_r - I_t)E_{ph}}{I_0}. \tag{2.14}$$

For more details see references [217, 222].

3. Experimental methods

The methods used within this thesis are briefly summarized in this chapter. If not stated in more detail, the measurements were performed in the Institute of Solid State Physics at the Friedrich Schiller University Jena.

3.1. Sample preparation

3.1.1. Synthesis of stoichiometric, homogeneous CZTSe and CZGeSe powders

Stoichiometric, homogeneous CZTSe and $Cu_2ZnGeSe_4$ (CZGeSe) powders were synthesized by Dr. Galina Gurieva in the group of Prof. Susan Schorr at the Helmholtz-Zentrum Berlin für Materialien und Energie (HZB). In a solid state reaction based process, pure elements were placed in pyrolytic graphite boats and annealed in a multistage process under vacuum conditions. The composition of the produced powders were determined at HZB by wavelength-dispersive X-ray spectroscopy using a JEOL-JXA 8200 electron probe microanalyzer. A PANalytical X'Pert PRO MRD diffractometer at HZW was to used in order to determine the phase by X-ray powder diffraction. More details of the preparation process and compositional investigations are described in reference [184].

3.1.2. Synthesis of Ge-doped CZTSe solar cells by a sequential process

Ge-doped CZTSe kesterite solar cells were fabricated and characterized by Dr. Sergio Giraldo in the group of Dr. Edgardo Saucedo at the Catalonia Institute for Energy Research (IREC). In a sequential process, Cu/Sn/Cu/Zn metallic stacks were sputtered onto Mo-coated soda-lime glass. This process included thermal evaporation of a 5 nm thin Ge interface layer between Mo and the precursor stack and 10 nm on top of the precursor. Subsequently, the precursor is annealed in a two step routine under an Se + Sn (100 mg Se + 5 mg Sn) atmosphere in a tubular furnace. In the first annealing step, the stacks were heated to 400 °C for 30 min at 1.5 mbar Ar pressure and in a second step at 550 °C for 15 min at 1 bar Ar pressure. The heating ramps were set to

20 °C/min. After letting the samples cool down, the surface of the CZTSe:Ge absorbers were chemical cleaned using $(NH_4)_2S$. Finally, the window layer was deposited using chemical bath deposition for the CdS layer ($\sim$ 50 nm), followed by sputtering of $\sim$ 50 nm i-ZnO and $\sim$ 200 nm ITO. Illuminated J–V curves were measured at IREC at 25 °C using a calibrated Sun 3000 class AAA solar simulator (Abet Technologies). The nominal composition was also measured at IREC with a calibrated Fischerscope XVD X-ray fluorescence spectrometer. More details of the synthesis can be found in references [41, 49, 50].

3.1.3. Synthesis of CZTSSe solar cells by spray coating

Kesterite CZTSSe absorbers were produced and characterized by Dr. Gerardo Larramona from IMRA Europe. The absorbers were synthesized using an additive-free water-ethanol (90 %vol - 10 %vol) based ink of Cu-Zn-Sn sulfide colloids with a primary particle size of $\sim$ 10 nm. This ink was spray-deposited onto Mo-coated soda-lime glass. Subsequently, the samples were annealed in a N_2 atmosphere, followed by a second annealing step under Se-Ar atmosphere. Final reference solar cells were produced by the deposition of a CdS layer with a thickness of $\sim$ 50 nm via chemical bath deposition, followed by sputtering of a $\sim$ 60 nm i-ZnO layer and $\sim$ 400 nm ITO layer. The nominal composition was estimated based on the ratio of the metal chloride salts in the mother solution. Illuminated J–V curves were measured at 25 °C using a AAA-class solar simulator (Oriel Sol3A Class) at IMRA. More details on the synthesis can be found in reference [223].

3.1.4. Synthesis of CIGS Rb post-deposition treated solar cells by co-evaporation

Thin film CIGS solar cells were produced by Dr. Philip Jackson from the Zentrum für Sonnenenergie-und Wasserstoff-Forschung Baden-Württemberg (ZSW). In a co-evaporation-based multistage process Cu, In, Ga, and Se were deposited on top of Mo coated soda-lime glass. The composition of the absorber was controlled by means of the evaporation rate and the substrate temperature. Afterwards, the CIGS absorber was subjected to a RbF post-deposition treatment. The solar cell was completed by the deposition of a 30-50 nm thick CdS layer via chemical bath deposition, followed by sputtering of a 50-100 nm thick i-ZnO layer and an Al-ZnO layer with a thickness of 150-200 nm. Subsequently, a Ni/Al/Ni grid was evaporated for efficient carrier collection. Finally, a 110 nm thick MgF_2 layer was deposited to achieve the highest

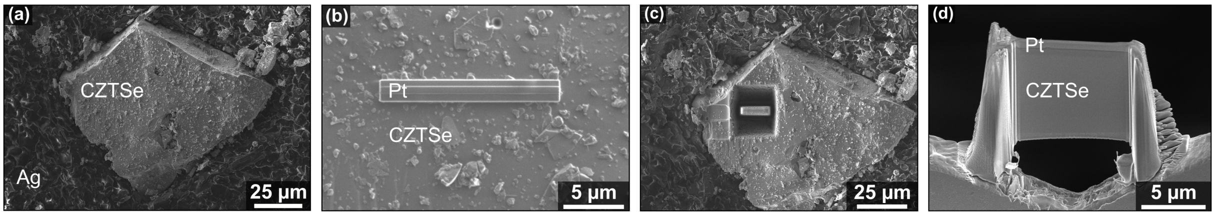

Figure 3.1.: Scanning electron micrographs of the lamella preparation from a stoichiometric CZTSe powder grain. (a) Single powder grain sprinkled onto silver paste. (b) Deposited electron and ion beam Pt layer on top of the grain. (c) Separation of the lamella. (d) Final lamella mounted onto a nickel grid and thinned down to 310 nm.

efficiency. More details of the preparation process are described in reference [54].

3.1.5. Lamella preparation

Cross-sectional lamellae were prepared using a FEI DualBeam Helios NanoLab 600i focused ion beam (FIB) system. Figure 3.1 shows the different steps during the lamella preparation, in this case, from a single grain powder sample (see section 3.1.1), which was sprinkled onto silver paste (figure 3.1a). In the first step a protective layer of Pt was deposited to the desired area from which the lamella will be taken (figure 3.1b). This layer protects the underlying material during preparation and reduces the curtaining effect[1] [224]. A focused Ga ion beam was then used to remove the surrounding material by sputtering (figure 3.1c). Subsequently, the lamella was lifted out and mounted onto a nickel TEM grid (figure 3.1d) using a micro manipulator. Finally, the lamella was thinned down and cleaned with XeF_2 to remove agglomerations. As shown in figure 3.1d, the final lamella structure comprises of an evenly thinned area and two thicker areas at the edges (ridges), which serve for stabilization. Detailed information about the lamella preparation can be found in references [225, 226].

3.2. Synchrotron-based techniques

3.2.1. Nanoscale X-ray fluorescence spectroscopy (nano-XRF)

The general measurement principle of nanoscale X-ray fluorescence spectroscopy (nano-XRF) on a lamella used in this thesis is shown in figure 3.2a. The lamella was gradually moved through the focused synchrotron nanobeam using a piezo stage and a complete X-ray fluorescence spectrum was detected at each step. The individual spectra of each

---

[1] An uneven sample surface changes the sputter yield, which leads to striation on the surface of the prepared cross-section, so called ”curtaining effect”.

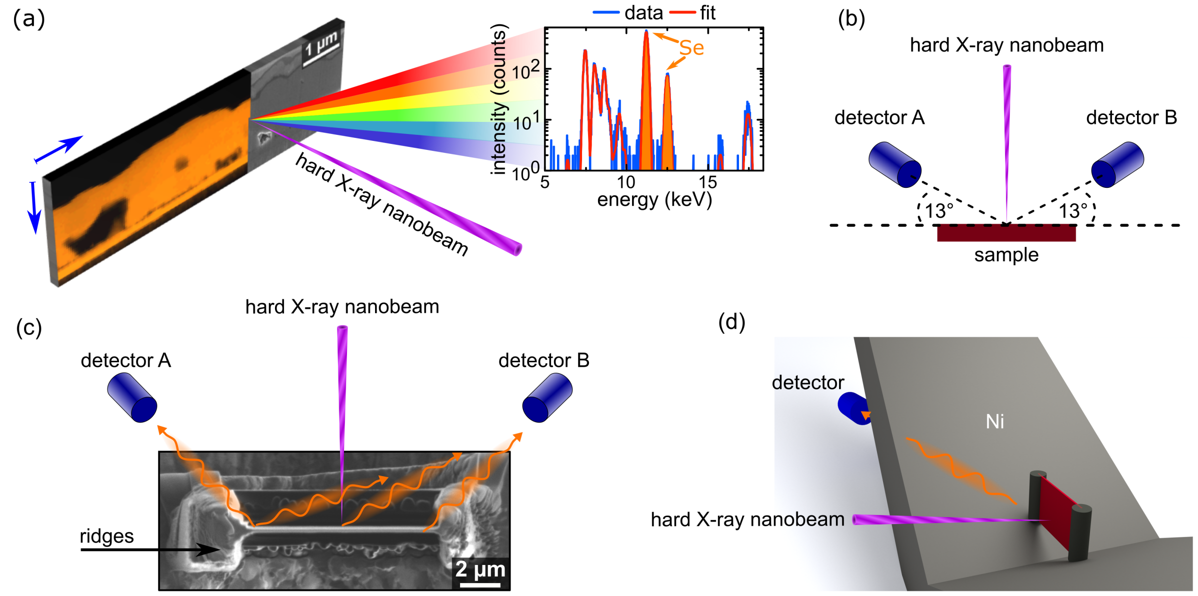

Figure 3.2.: (a) Measurement principle of nano-XRF on a lamella. The lamella is raster scanned via the highly focused hard X-ray synchrotron nanobeam in vertical and horizontal directions. At each position a XRF spectrum is taken, which can then be converted to intensity or concentration maps, as shown here for Se. (b) Schematic drawing of the experimental geometry at the nanoanalysis beamline ID16B of the ESRF. (c,d) Schematic illustration of a lamella during the measurement. The lamella ridges attenuate the created fluorescence radiation close to the ridges, whereas the radiation is not affected if the nano-beam hits a position closer to the center of the lamella. Additionally, the Ni grid homogeneously attenuates the fluorescence radiation.

pixel were evaluated using PyMCA [211] to determine the local elemental intensities and local concentrations. The advantage of this program is that instead of modeling peaks of different elements independently, PyMCA models the peaks of all included elements simultaneously. Thus, the evaluation of elements is possible even when the peaks of different elements overlap. Furthermore, other effects such as self attenuation by the sample, pile-up, and escape peaks are also included. The measurements were performed at the nanoanalysis beamline ID16B of the European Synchrotron Radiation Facility (ESRF) in Grenoble, France [227]. The energy of the synchrotron nanobeam was set to 29.6 keV in "pink-beam" mode ($\Delta E/E = 10^{-2}$) with an average photon flux of $2.5 \cdot 10^{10}$ photons/s , a focal spot size of $54 \times 52\,\mathrm{nm}^2$, a counting time of 800 ms/pixel, and a step size of $50\,\mathrm{nm}^2$.

The experimental setup at ID16B is schematically depicted in figure 3.2b. The X-ray nanobeam hits the sample perpendicular to the surface and two 3-element silicon drift detectors detect the created fluorescence radiation under an angle of 13 °. This shallow detection angle caused two unintended effects influencing the measured fluorescence radiation, when lamellae are investigated with the structure described in section 3.1.5. Fluorescence radiation gets inhomogeneously attenuated close to the ridges, whereas it is not affected when the nanobeam hits a position closer to the center of the lamella (figure 3.2c). Therefore, only the area which was not influenced by the ridges was evaluated. The second effect, which influenced the fluorescence radiation, is illustrated in figure 3.2d, showing attenuation by the Ni grid. As this attenuation was homogeneous throughout the lamella and the grid dimension was the same for all investigated lamellae, the created fluorescence was always influenced in the same way. Thus, relative changes between different areas are reliable. Both effects finally caused that only one of the six detectors could be used for the data evaluation.

3.2.2. Nanoscale X-ray absorption near-edge structure spectroscopy (nano-XANES)

X-ray absorption near-edge structure spectroscopy measurements at the nanoscale (nano-XANES) were performed in fluorescence mode at the nanoanalysis beamline ID16B of the European Synchrotron Radiation Facility (ESRF) in Grenoble, France [227]. The experimental setup was similar to the one shown in figure 3.2, with the major difference that a new 7-element silicon drift detector located at an angle of 35 ° recorded the emitted fluorescence. This comparable wide angle enabled to overcome the attenuation problems of both the Ni grid and the lamella ridges, except for acquisitions close to the lamella ridges. Thus, these regions were excluded during the XANES measurements. The energy of the synchrotron nanobeam was set to 11.103 keV (Ge K-edge) in “monochromatic beam” mode ($\Delta E/E = 10^{-4}$) with an average photon flux of $1.4 \cdot 10^7$ photons/s and a focal spot size of $150 \times 135\,\mathrm{nm}^2$. The energy was scanned from 53 eV below to 197 eV above the Ge edge with a step size of 1 eV. For each energy the counting time was set to 100 ms. Twenty scans were collected and summed up to improve statistics. The final XANES spectrum was obtained by averaging five of such spectra to improve the signal-to-noise ratio. Due to the low flux and high counting time, only selected spots were investigated with this technique. Finally, the data were standardized and partially smoothed after the normalization. Finally, the XANES spectra were evaluated using the software Athena [228]. Detailed information about the data evaluation can be found in reference [208, 214].

3.2.3. Nanoscale X-ray beam induced current (nano-XBIC)

Thin film CIGS solar cells were investigated by XBIC measurements on the nanoscale (nano-XBIC) while simultaneously detecting the nano-XRF signal. The experimental setup in the so called ’top-view’ geometry is illustrated in figure 3.3. The contacted device was raster scanned through the focused synchrotron nanobeam using a piezo

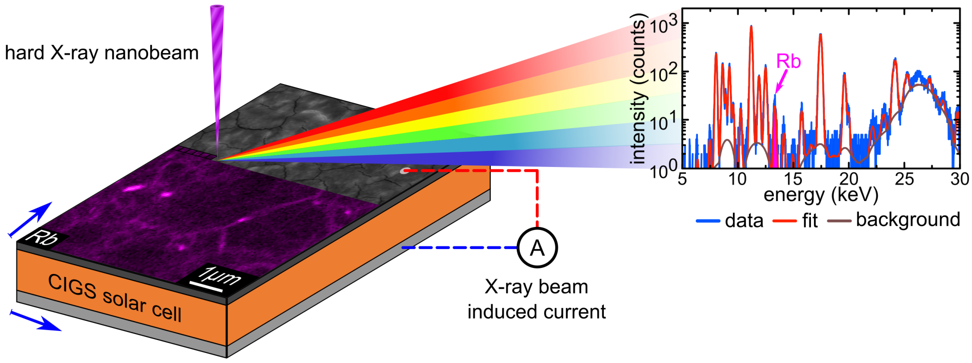

Figure 3.3.: Measurement principle of combined nano-XRF and nano-XBIC on a complete solar cell in top-view geometry. The device was raster scanned through the highly focused hard X-ray synchrotron nanobeam in vertical and horizontal directions. At each position a XRF spectrum was detected, which was then converted to intensity or concentration maps, as shown here for Rb. Simultaneous, the generated current was measured, which yields into a current map.

stage. A XRF spectrum and current signal was detected for every position.

The measurements were performed at the nanoanalysis beamline ID16B of the European Synchrotron Radiation Facility (ESRF) in Grenoble, France [227]. The energy of the synchrotron nanobeam was set to 29.6 keV in "pink-beam" mode ($\Delta E/E = 10^{-2}$) with an average photon flux of $4.0 \cdot 10^{10}$ photons/s, a focal spot size of $60 \times 56\,\text{nm}^2$, a counting time of 800 ms/pixel, and a step size of 50 nm. The created fluorescence radiation was detected by a 7-element silicon drift detector. The concentrations of all elements of interest were individually estimated by fitting the XRF signal using the software PyMCA [211]. The XBIC signal was collected using an EG&G 7280 DSP lock-in amplifier.

3.3. Electron microscope-based techniques

3.3.1. Scanning electron microscopy (SEM) and scanning transmission electron microscopy (STEM)

The morphology of complete solar cells and cross sectional lamellae was examined using a high resolution scanning electron microscope (SEM) (FEI DualBeam Helios NanoLab 600i FIB system). The microscope is equipped with a field emission electron gun emitting electrons with a maximum energy of 30 kV and a maximum current of 22 nA. The immersion mode provides a lateral resolution down to approximately 1 nm. Cross sectional lamellae were further investigated by scanning transmission electron microscopy (STEM) in the same electron microscope. The contrast of these images relies on different diffraction contrasts of the individual grains. In this way, the grain structure of the sample can be obtained. STEM detectors consist of several segments, thus allowing different operating modes: dark field (DF), bright field (BF), and high angle annular dark field (HAADF). Detailed information about both electron microscopy techniques are presented in reference [229, 230] .

3.3.2. Transmission electron microscopy (TEM)

For a detailed investigation of nanoscale features, cross sectional lamellae were investigated using a JEOL Jem-3010 transmission electron microscope (TEM) at the Otto Schott Institute of Materials Research (FSU Jena). A stationary parallel electron beam with an energy of 300 keV is transmitted through the sample. Electrons, which are unaffected by the transmission, are focused on the detector, while those who undergo scattering at the lattice atoms are defocused forming the image (bright field (BF) imaging). The scattering cross section strongly depends on the atomic number determining the contrast of this technique. Detailed information about this technique is given in reference [230].

3.3.3. Electron backscatter diffraction (EBSD)

The orientation of different grains can be accessed by electron backscatter diffraction (EBSD), thus allowing to determine the misorientation of adjacent grains, which enables to classify grain boundaries. In this thesis, kesterite CZTSe lamellae were investigated by EBSD. CZTSe has a tetragonal phase with lattice parameters of a = 5.698 Å and c = 11.352 Å [184]. Thus, CZTSe only shows a minimal tetragonal distortion with a c/2a relation of only 0.996. This complicates the EBSD analysis as shown by Martin et al. [231] in the case of tetragonal ZrO_2. When the tetragonal distortion becomes too small, the applied software cannot distinguish between cubic and tetragonal phase, thus failing to index the EBSD patterns when applying the kesterite-type CZTSe material file that is based on ICSD-file no. 200419. However, a cubic approximation, in this case by applying a material file of cubic Si, showed good indexing results. As a consequence, the twinning relations had to be defined as 60° rotations around the $\langle 111 \rangle$ direction and as 70.53° rotations around the $\langle 110 \rangle$ direction in an approximated cubic structure [232] instead of 60° rotations around the $\langle 221 \rangle$ direction and as 70.53° rotations around the $\langle 110 \rangle$ direction in the tetragonal lattice [231].

The scans were performed using a Jeol JSM 7600F SEM equipped with a Nordlis Max EBSD camera at the centre for Functional and Surface Functionalized Glass, Alexander

Dubček University of Trenčín, Slovakia. The scans were performed using electrons of 20 kV, a current of up to 2.2 nA, and a step sizes of 50 nm. The scans were captured using the Oxford Instruments software AZtec® and evaluated using the Channel 5 software package. A detailed introduction of this technique can be found in reference [233].

3.3.4. Energy-dispersive X-ray spectroscopy (EDS)

The qualitative and quantitative elemental composition of a sample can be obtained by energy-dispersive X-ray spectroscopy (EDS) measurements. It works in a similar way as XRF (introduced in section 2.3.1) with the major difference that an electron beam is used to excite the core electrons, instead of a X-ray beam. The scattered electrons create bremstrahlung, thus, EDS is not as sensitive as XRF.

EDS measurements were carried out at the FEI DualBeam Helios NanoLab 600i FIB system equipped with a large area Oxford Instruments X-Max^N silicon drift detector. The data were evaluated with AZtec®, a commercial software provided by Oxford Instruments. The software uses the XPP (extended Pouchou Pichoir) model [234], which is based on the $\phi(\rho z)$ function to correct for matrix effects. Hereby, $\phi(\rho z)$ describes the relative intensity of the X-ray generation rate in dependence of the sample thickness z and sample density ρ. EDS measurements were conducted with an electron energy of 30 keV, a current of 0.69 nA, and a measurement time of 15 min/μm^2. More details about EDX can be found in reference [235].

4. Characterization of stoichiometric, homogeneous, single-phase $Cu_2ZnSnSe_4$

This chapter discusses the experimental limits of EDS and XRF using lamellae that were taken out of a stoichiometric, single-phase CZTSe powder grain. It highlights the interplay of statistics, spatial resolution, absolute concentrations, and their experimental uncertainties. Moreover, the strong need to calibrate EDS measurements conducted on kesterite lamellae is demonstrated. The CZTSe powder was synthesized by Dr. Galina Gurieva and provided by Prof. Susan Schorr (Helmholtz-Zentrum Berlin für Materialien und Energie, HZB). The lamella was prepared by Dr. Sven Schönherr and the EDS measurements were conducted in cooperation with Dr. Philipp Schöppe. Nano-XRF measurements were performed in collaboration with Dr. Sven Schönherr, as well as Konrad Ritter, Prof. Claudia S. Schnohr (Universität Leipzig), Dr. Andreas Johannes, Dr. Damien Salomon (European Synchrotron Radiation Facility, ESRF), and Dr. Gema Martínez-Criado (Instituto de Ciencia de Materiales de Madrid, CSIC). Parts of this chapter are published in reference [67].

4.1. Motivation

The basis of this thesis is the measurement and evaluation of electron- and X-ray-based fluorescence radiation spectra. To gain quantitative elemental information through fitting of such spectra, the respective software (AZtec® for EDS and PyMCA [211] for XRF) needs to model the background, and the characteristic X-ray peaks. Thereby, it has to include the excitation probabilities for all elements for a given primary beam energy, and needs to know the transition rates of the X-ray lines. In addition, pile-up and escape peaks can also occur, and have to be taken into account. Thus, modeling fluorescence spectra and determining absolute concentrations are still challenging. Therefore, it is of great interest to learn about the limitations and experimental uncertainties of the system using a well known reference material.

The EDS measurements focus on the investigation of the spatially resolved composition on lamellae that were prepared out of thin film kesterite solar cells or absorbers with

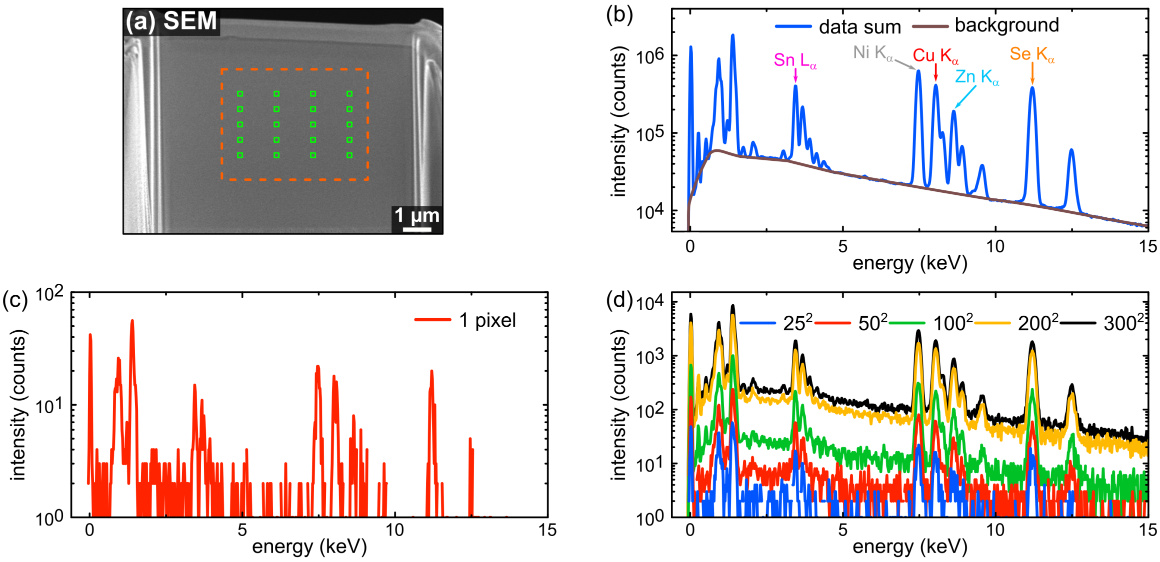

Figure 4.1.: (a) SEM image of the of the stoichiometric, single-phase CZTSe reference lamella. The orange rectangle in (a) mark the area where EDS measurements were conducted and the evenly distributed green rectangles exemplarily mark regions where spectra were extracted, in this case with a size of $200 \times 200\,\mathrm{nm}^2$. The average thickness of this lamella was approximately 310 nm. (b) EDS sum spectrum, which shows the integrated intensity in the orange marked rectangle, together with a possible background. For a single pixel the spectrum is illustrated in (c), while (d) shows the integrated spectra for different areas with sizes ranging from $25 \times 25\,\mathrm{nm}^2$ - $300 \times 300\,\mathrm{nm}^2$.

thicknesses between 160 - 340 nm, as well as the examination of lateral variations. An ideal reference consists of the same elements with a similar stoichiometry and the same crystal structure. A stoichiometric, single-phase $Cu_2ZnSnSe_4$ powder has all the desired properties and can be synthesized by solid sate reaction (see section 3.1.1). As the grain size of this powder was roughly 100 µm (compare figure 3.1) a cross-sectional lamella could be prepared in the same fashion as described in section 3.1.5. Thus, the reference has a similar excitation volume and related spatial resolution like the lamellae prepared out of CZTSe solar cells and CZTSSe absorbers, which are investigated in chapter 5 and 6.

4.2. Calibration of energy-dispersive X-ray spectroscopy

Figure 4.1a shows the SEM image of the stoichiometric, single-phase CZTSe reference lamella. EDS measurements with an electron energy of 30 keV were performed in the orange marked rectangle. The corresponding sum spectrum in figure 4.1b reveals the characteristic X-ray peaks of Cu, Zn, Sn and Se, on top of the continuous background (for the elemental intensity maps see figure A.1 in the appendix). Note, the software package AZtec® does not allow to extract the real shape of the fitted background, thus a possible shape based on the noise level has been defined. Next to Cu a strong

Table 4.1.: Nominal composition of the CZTSe reference and uncalibrated atomic concentrations determined from the EDS measurements, which were taken on the CZTSe reference. They were derived by fitting the sum spectrum and the spectra of 20 individual spots which were evenly distributed throughout the lamella for each spot size, respectively. The values represent the mean value and standard deviation of the 20 selected areas. The blue highlighted values are used to calculate the calibration factors.

area (nm^2)	Cu (at.%)	Zn (at.%)	Sn (at.%)	Se (at.%)
nominal	25.0	12.5	12.5	50.0
sum	26.5	13.0	14.2	46.2
1 pixel	25.8 ± 4.7	12.2 ± 2.2	13.3 ± 2.3	48.6 ± 3.5
25 x 25	25.7 ± 3.3	13.4 ± 2.6	14.4 ± 2.9	46.6 ± 5.0
50 x 50	26.6 ± 2.0	12.8 ± 0.9	13.9 ± 1.3	46.7 ± 2.3
100 x 100	26.5 ± 0.6	12.8 ± 0.5	14.2 ± 0.5	46.5 ± 1.0
200 x 200	26.7 ± 0.4	13.0 ± 0.3	14.2 ± 0.2	46.1 ± 0.4
300 x 300	26.5 ± 0.3	13.0 ± 0.3	14.1 ± 0.2	46.3 ± 0.3
calibration factor	0.937	0.964	0.880	1.083

Ni peak is visible, which stems from secondary excitation of the Ni grid on which the lamella was mounted. For qualitative and especially for quantitative analyzes of EDS spectra, the primary electron beam energy should be at least two times higher (ideal value is ~ 2.7) than the electron binding energy (so-called overvoltage ratio) in order to efficiently generate fluorescence radiation [235]. Tin with an electron binding energy of 29.20 keV for the K shell can not be excited by the restricted electron beam energy of 30 keV. Fortunately, the L-lines at roughly 3.44 keV do not overlap with other fluorescence lines and can be used for quantification, although their signal-to-noise ratio is worse compared to the K-lines. For Cu, Zn and Se the K-edges are well below 15 keV and thus, suited to quantify these elements.

The composition of the sample can be extracted by fitting the EDS sum spectrum. The results reveal a relative big overestimation of the cation elements accompanied with a reduced anion concentration (see table 4.1) demonstrating the urgency to calibrate the measurements. However, fitting the sum spectrum is not intended, because the aim of this thesis is to study the elemental concentrations spatially resolved. Ideally a single pixel can be used for quantification, but figure 4.1c clearly demonstrates that the statistics of a single pixel and its signal-to-noise ratio is not sufficient, although it is possible to force the software to perform a fit. The signal-to-noise ratio improves by increasing the size of the integrated area, as shown in figure 4.1d, and an improved fit is possible. By extracting and evaluating the spectra with the same size at 20 different lateral positions, it was possible to define the experimental accuracy by the variations between these different regions on the lamella. The calibration factors were calculated by their mean values assuming spatial homogeneity. Table 4.1 list the mean values and standard deviations for different sizes areas. Similar to the previous discussed results for the sum spectrum, the software AZtec® overestimates the cation concentrations and underestimates the Se concentration. For a single pixel and for an area of 25 × 25 nm^2 the mean values show a difference to the sum fit, because the statistics are too low to get reliable results. Already at a size of 50 × 50 nm^2 the concentrations show no significant difference to the sum. Further, the standard deviations, reflecting the experimental uncertainty improve drastically, which is in fact expected due to the improved signal-to-noise ratio. Of course the aim is the best spatial resolution, but it is reasonable to exclude one 1 pixel and 25 × 25 nm^2 because the spectra are noisy. Moreover, the extracted concentration does not fit to the sum spectrum and the standard deviation is very high. Comparing the remaining values, the standard deviation improves until a size of 200 × 200 nm^2 is reached. Only a slight improvement for Cu and Se is noticeable by further increasing the integration area. Thus, a size of 200 × 200 nm^2 is an ideal compromise of sufficient statistics and a still good spatial resolution. In principle, the uncertainty could also reflect real compositional variations. Therefore, several spots with a size of 200 × 200 nm^2 were examined 20 times in a row on the same lamella and under the same experimental conditions. The mean values and standard deviations were similar for Cu, Zn, and Sn and only the deviation of Se was slightly increased by 0.1 at.%. Nevertheless, the good agreement between the standard deviations of the locally different areas and the consecutive measured areas proves the homogeneity of this sample and that variations in table 4.1 correspond to the experimental uncertainty. In general, it is also possible to improve the spatial distribution with an uncertainty similar to 200 × 200 nm^2 by extending the measurement time. To reduce the area to 100 × 100 nm^2, the accumulation time has to be increased by a factor of 4, which means an increase to 60 $\mathrm{min}/\mu\mathrm{m}^2$. With sizes over 20 $\mu\mathrm{m}^2$ for unknown samples a measurement time of 20 hours or more is not feasible and other effects like sample degradation or drift might play a role.

Finally, the calibration factors are calculated by dividing the nominal composition by the mean value acquired from the 200 × 200 nm^2 sized evaluation. In this thesis every EDS measurement conducted on kesterite lamellae was further calibrated with the values listed in table 4.1.

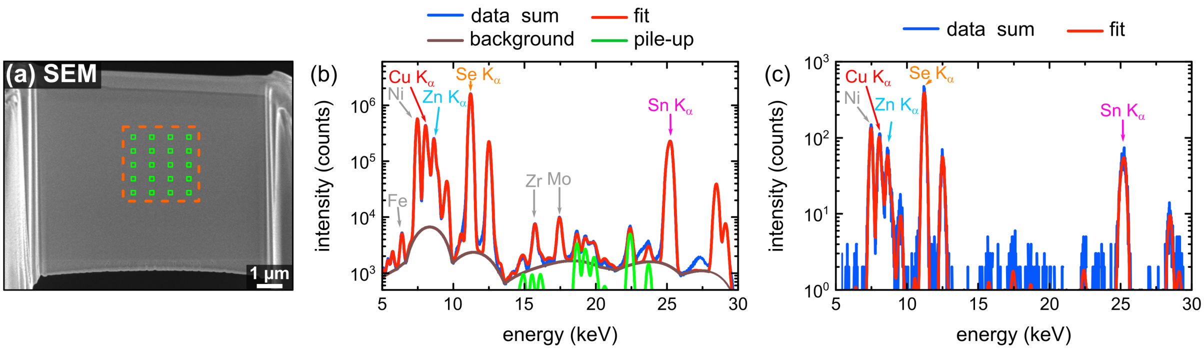

Figure 4.2.: (a) SEM image of the of the stoichiometric, single-phase CZTSe reference lamella. The orange rectangle marks the area where XRF measurements were conducted, and the evenly distributed green rectangles exemplarily mark regions where spectra were extracted, in this case with a size of $200 \times 200\,\mathrm{nm}^2$. The average thickness of this lamella was approximately 160 nm. (b) Integrated nano-XRF spectrum of the entire investigated area, including the fit, background and pile-up. (c) Spectrum for a single pixel (size: $50 \times 50\,\mathrm{nm}^2$) with the corresponding fit.

4.3. Experimental uncertainty of nanoscale X-ray fluorescence spectroscopy

The SEM image in figure 4.2a illustrates the stoichiometric, single-phase CZTSe reference lamella on which XRF measurements were taken at the ESRF with an X-ray energy of 29.6 keV and a focal spot size of $52 \times 54\,\mathrm{nm}^2$ (for details see section 3.2.1). The corresponding XRF sum spectrum in figure 4.2b shows the integrated intensity in the orange marked region together with the respective fit using the software package PyMCA [211]. Similar to the EDS spectrum in figure 4.1b the characteristic peaks of Cu, Zn, Sn, and Se can be identified on top of a continuous background, in this case modelled using the software PyMCA [211]. The fitted intensity maps are illustrated in figure A.2 (appendix). A major difference to the electron beam is the possibility to excite the K shell of Sn, whose fluorescence peak is clearly visible at roughly 25.3 keV. Moreover, the Ni peak is again present but also peaks in the energy region below Ni and between Se and Sn. Some of these peaks originate from pile-up, others from secondary excitation or scattered X-rays exiting the experimental setup, such as the sample holder, piezo stage, etc. The single pixel spectrum in figure 4.2c is dominated by the matrix elements of the lamella and the Ni peak from the grid. Remarkably, the excellent signal-to-noise ratio allows to fit the spectrum of every individual pixel. An almost perfectly homogeneous distribution for the reference elements can be identified in the fitted intensity maps in figure A.2 (appendix). As already discussed in section 3.2.1 during the XRF acquisition, the Ni grid slightly attenuates the fluorescence radiation, thus the estimation of absolute concentrations is not possible. Since this attenuation was homogeneous throughout the lamella relative changes between different areas

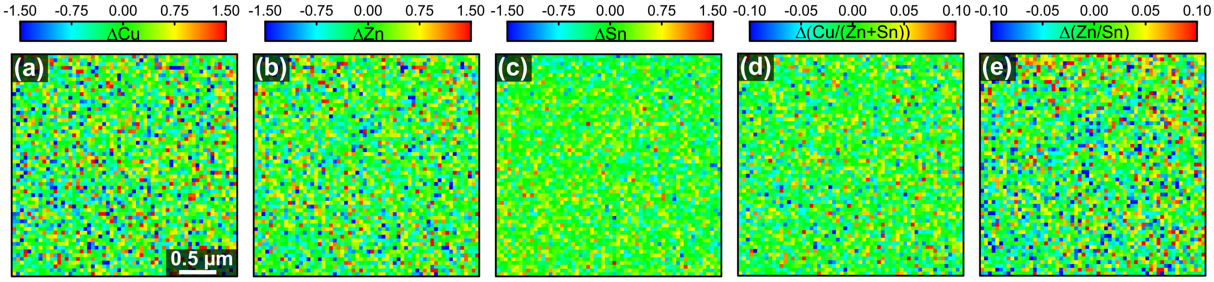

Figure 4.3.: Deviation of the cation atomic concentrations for Cu, Zn, and Sn (a-c), and for the cation ratios (d, e) from the respective mean value for the stoichiometric, homogeneous, single-phase CZTSe reference lamella. These maps were calculated by subtracting the mean value of a particular map from the actual value of every individual pixel.

Table 4.2.: Standard deviations of the cation atomic concentrations and cation ratios, determined from the nano-XRF measurements, for a single pixel and with a size of 200 × 200 nm^2 (16 pixel) based on 20 selected areas. The values of the EDS measurements are adopted from table 4.1.

area	σ(Cu (c-at.%))	σ(Zn (c-at.%))	σ(Sn (c-at.%))	σ(Cu/(Zn+Sn))	σ(Zn/Sn)
1 pixel	0.7	0.7	0.4	0.04	0.05
16 pixel	0.2	0.2	0.1	0.01	0.02
EDS	0.6	0.6	0.4	0.03	0.03

are still reliable. Thus, figure 4.3 shows the maps of the relative differences for the cation atomic concentration, namely ΔCu, ΔZn, and ΔSn, and for the cation ratios, namely Δ(Cu/(Zn+Sn), and Δ(Zn/Sn). They are calculated by determining the mean value of a particular map similar to the EDS measurements, i.e., from 20 spots with an area of 200 × 200 nm^2.This mean value was then subtracted from the local value for every pixel. The variations within these maps represent the noise level and can be used to define the experimental uncertainty (standard deviation). Table 4.2 summarizes the estimated experimental uncertainty for both the cation atomic concentrations and the cation ratios based on the 20 spot evaluation for a single pixel and for a size of 200 × 200 nm^2 (16 pixel). The sensitivity increased roughly by a factor of 2 for the same resolution compared to EDS, which is of course expected due to higher counting statistics.

4.4. Summary

A stoichiometric, homogeneous, single-phase CZTSe lamella was investigated by electron- and X-ray-based spectroscopy techniques. The experiential determined composition by EDS is off-stoichiometric, demonstrating the urgency to calibrate all EDS measurements conducted on CZT(S,Se) lamellae in the following chapters of this thesis.

Since the composition and experiential uncertainty strongly depend on the statistics, ideal parameters were found for an integration area of $200 \times 200\,\mathrm{nm}^2$. They represent the best compromise between an excellent signal-to-noise ratio, a good fit of the peaks, and the best spatial resolution. In contrast, the XRF spectrum of a single pixel with a size of $50 \times 50\,\mathrm{nm}^2$ has a sufficient signal-to-noise ratio. Thus, it was possible to evaluate the elemental distribution with a 16 times better spatial resolution compared to EDS.

5. Germanium incorporation in homogeneous $Cu_2ZnSnSe_4$ solar cells

This chapter highlights morphological, compositional, structural, and microstructural properties of Ge-doped CZTSe kesterite solar cells, which are correlated to electrical parameters. These solar cells were fabricated and electrically characterized by Dr. Sergio Giraldo from the group of Dr. Edgardo Saucedo (Catalonia Institute for Energy Research, IREC). The cross-sectional lamellae were prepared by Dr. Sven Schönherr. SEM and STEM images were taken in cooperation with Dr. Sven Schönherr and Oliver Rüger. TEM investigations were conducted in cooperation with Dr. Philipp Schöppe. Nano-XRF and nano-XANES measurements were performed in collaboration with Dr. Sven Schönherr, Christian T. Plass, as well as Konrad Ritter, Prof. Claudia S. Schnohr (Universität Leipzig), Dr. Andreas Johannes, Dr. Damien Salomon (European Synchrotron Radiation Facility, ESRF), and Dr. Gema Martínez-Criado (Instituto de Ciencia de Materiales de Madrid, CSIC). The CZTSe and CZGeSe reference samples were synthesized by Dr. Galina Gurieva and provided by Prof. Susan Schorr (Helmholtz-Zentrum Berlin für Materialien und Energie, HZB). The EBSD experiments were carried out by Dr. Wolfgang Wisniewski (Alexander Dubček University of Trenčín). Parts of this chapter are published in references [66–68].

5.1. Motivation

The main limitation of thin film kesterite solar cells is still the low V_{OC}, which is drastically reducing the efficiency. Recently, record conversion efficiencies of 11.8 % [50] for pure selenide-based kesterite cells were achieved by introducing a superficial Ge layer during the synthesis boosting the V_{OC} from 400 mV for a Ge free reference to 469 mV for the record device. So far it is only known that Ge improves the grain morphology and helps to modify the reaction pathways of CZTSe from a tri-molecular process towards a mainly bi-molecular process, by suppressing the formation of a involuntary Sn–Se phase during the synthesis [50]. Moreover, other aspects like the superior control of Na in the absorber and at the interfaces, or the improved charge transport properties might also be accounted to the Ge introduction [203, 236, 237].

To gain a more comprehensive understanding of the origin of the improvement,

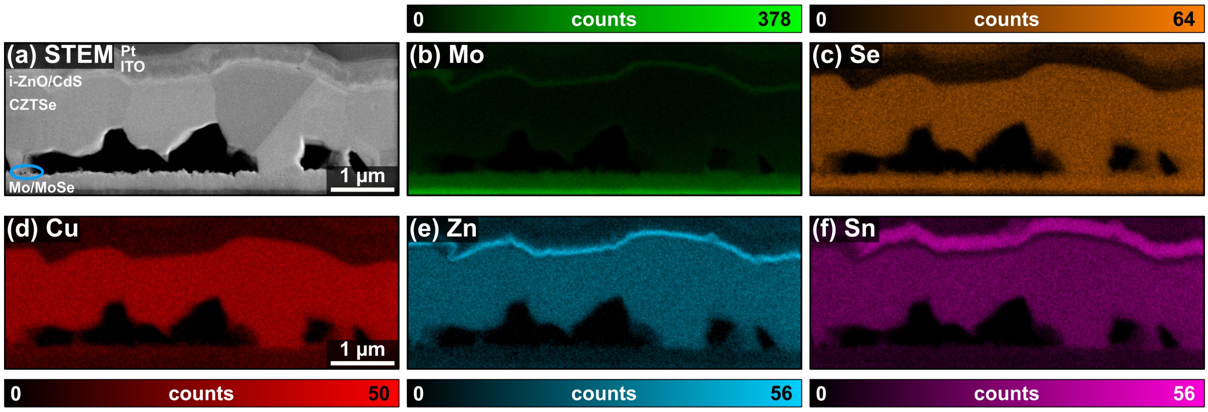

Figure 5.1.: STEM-pHAADF image (a) and EDS intensity maps of the back contact (b) and the four absorber elements (c-f) of a Ge-doped CZTSe solar cell with the nominal composition S1. The intensity maps were obtained by integrating the counts for each pixel in an energy interval (see appendix table A.1) for the individual elements. The small Mo signal within the absorber originates from secondary excitation of the Mo back contact, while the Mo signal in the CdS layer stems from the strong superposition of the Mo L_α-lines and the S K_α-line. The alleged Se signal in the Pt layer stems from a combination of both effects, i.e., secondary excitation and the superposition of the Pt L_β-line and Se K_α-line. The average thickness of this lamella was approximately 210 nm.

Ge-doped CZTSe solar cells were fabricated with different nominal compositions in order to determine the morphological, compositional, structural, and microstructural properties of the devices. For details about the solar cell synthesis see section 3.1.2.

5.2. Morphology

The STEM image in figure 5.1a depicts the cross-sectional lamella prepared out of a complete CZTSe:Ge solar cell with nominal Cu/(Sn+Zn) and Zn/Sn ratios of 0.83 and 1.13 (S1), respectively. The Mo back contact is visible at the bottom of the micrograph on top of the CZTSe:Ge absorber was grown on. A more detailed examination of the micrograph reveals a thin $MoSe_2$ interface layer formed during the selenization process with a thickness of roughly 200 nm, which has a mainly beneficial effect on the charge collection and will likely not contribute to V_{OC} losses [238]. The dark regions at the CZTSe/MoSe interface indicate the formation of several voids with varying sizes ranging from a few hundred nm up to more than 1 µm. The exact origin is not yet known and several reasons should be considered: fast Cu out-diffusion [239], the formation and evaporation of SnSe [240, 241], the dezincification of the precursor layer stack caused by emerging ZnSe [240], or the reaction of CZTSe with Mo [242]. Detrimental effects to the conversion efficiency are very likely, because roughly 19 % of the absorber is missing for light conversion. Moreover, the reduced direct electrical contact between absorber and $MoSe_2$ layer likely contributes to an increased series resistance (R_{series}). Thus, both effects will likely reduce short circuit-current density (J_{SC}) and the fill factor (FF) [243]. The lamella also showed small nanometric voids at the back contact (see blue circle), which are not expected to have critical effects, as the minority and majority charge carrier diffusion length surpasses 500 nm, which is much higher than the void size [244]. The polycrystalline absorber is characterized by large grains with sizes lager than 1 µm in diameter in perfect agreement with the assumption of an improved grain growth due to the presence of Ge during the growth [41, 49, 50, 236, 245]. The absorber is covered with the CdS buffer layer onto which the front contact, consisting of an i-ZnO and ITO layer, was sputtered. Finally, the protective Pt layers, i.e., electron beam and Ga-ion beam deposited Pt are visible, which were was deposited during the lamella preparation (see also section 3.1.5).

Similar morphologies and no significant differences were also found for the lamellae prepared out of solar cells with different nominal compositions S2 and S3 (see figure 5.5a and 5.6a).

5.3. Detecting the spatially resolved composition and off-stoichiometry types

Compositional variations of the absorber and possible formations of secondary phases can significantly influence the device performance [32, 36, 246–252]. Therefore, EDS measurements were carried out on the same lamella shown in figure 5.1a to gain insight into the chemical identity of the absorber. Details about the measurements can be found in section 3.3.4 and 4.2.

The EDS spectrum in figure 5.2a illustrates the integrated fluorescence intensity detected on the lamella and the possible background. The absorber elements Cu, Zn, Sn, and Se are clearly identifiable together with the front and back contact elements. The Ni signal originates from the grid, similar as the Ni signal observed for the CZTSe reference. One of the key challenges is the identification of Ge. Therefore, the inset shows a magnification of the spectrum from 9 - 10.5 keV covering the Ge K_α fluorescence line at 9.886 keV. Since the signal is almost in perfect agreement with the background, Ge is either absent or below the detection limit. Nevertheless, EDS provides the possibility to investigate the remaining elements including their spatial distributions and compositions.

The corresponding EDS maps in figure 5.1b-f illustrate the intensity maps of the Mo (L_α-line) back contact and the four absorber elements of interest. Apparently, these maps reflect similar layers like the STEM image except for Pt, Cd, and S whose intensity

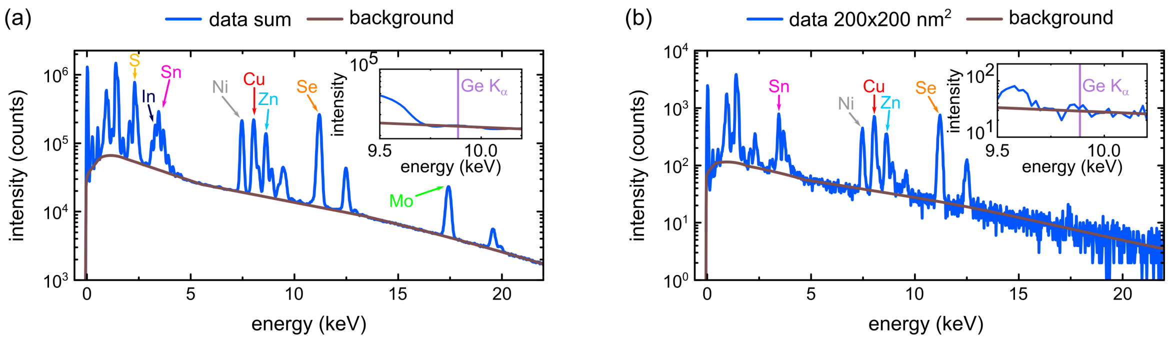

Figure 5.2.: EDS spectra taken on a lamella prepared out of a Ge-doped CZTSe solar cell, integrated over the entire area of the lamella (a) and in an area of 200 × 200 nm^2 (b), with their possible backgrounds. The elements of interest are marked by arrows. The insets show a magnification of the respective spectra in the energy region from 9 - 10.5 keV, covering the Ge K_α fluorescence line at 9.886 keV.

maps are not shown here. The Mo map reveals a strong signal at the bottom of the image followed by a layer that correlates with the Se map proving the formation of the $MoSe_2$ interface layer. A relatively low and apparent Mo signal in figure 5.1e is also present in the absorber and a more pronounced one in the CdS layer. This is a result of secondary excitation and the superposition of two fluorescence emission lines. The latter is clearly present for the Mo L_α-lines at 2.29 keV and S K-lines at roughly 2.30 keV (figure 5.3a), whereas the alleged Mo signal in the absorber layer is the result of secondary excitation. The combination of both effects also explains the strong Se signal in the Pt layer (figure 5.1c), because the Pt L_β-line at 11.07 keV overlaps with the Se_α-line at 11.22 keV (figure 5.3b) and the distinct Se peak indicates secondary excitation by high energy photons, which likely originate from L_γ transitions. The very small signals of Cu, Zn, and Sn in the Pt and front contact layers can be also explained by secondary excitation.

The absorber layer can be localized by comparing the STEM image and the intensity maps. Remarkably, a homogeneous distribution of the matrix elements is present. It has been reported that secondary phases were observed in Cu-poor and Zn-rich kesterite-based absorbers especially at the surface [253–256] and back contact [253, 256–261], but no depletions or hotspots indicate the formation of other phases apart from the kesterite. These findings are in excellent agreement with recent Raman spectroscopy [41, 262], TOF-SIMS [41], and glow discharge optical emission spectroscopy measurements [263]. Thersleff et al. [245] employed electron energy loss spectroscopy measurements to similar fabricated Ge-doped CZTSe layers and found a two layer system in the absorber, one less Cu-poor (top layer) with respect to the other (bottom layer). In their case, however, the absorber was grown under slightly different conditions, i.e., with 10 nm Ge on top of the precursor and no Ge on the Mo layer, whereas

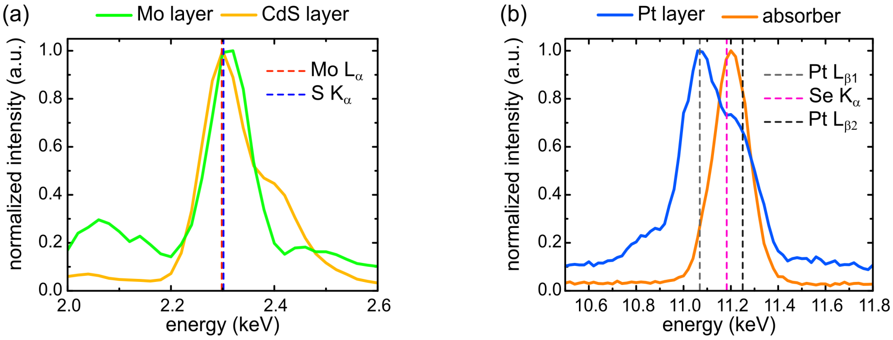

Figure 5.3.: Comparison of the normalized EDS spectra taken on the lamella as shown in figure 5.1a at different lateral positions. (a) Spectra taken from the Mo and CdS layer revealing the strong superposition of the Mo L_α-lines and S K_α-lines. (b) EDS spectra taken on the Pt layer and on the CZTSe:Ge absorber, demonstrate a partly superposition of the Pt L_β-lines and the Se K_α-lines. Moreover, a clear Se peak is also visible in the Pt spectra, which indicates secondary excitation.

in the present case a 5 nm layer was deposited on the Mo layer in addition to the 10 nm on top of the precursor. Thus, the formation of a bi-layer system is likely prevented using ideal quantities of Ge [50] promoting the homogeneous elemental distribution in such absorbers. The strong dependence on the ideal Ge amount is corroborated by Giraldo et al. [49], who found ZnSe and Cu related secondary phases when the Ge thickness surpasses 25 nm. As already mentioned earlier, the presence of ZnSe secondary phases was extensively investigated when the initial Zn/Sn ratio exceeds a value of 1.09 ± 0.04 for pure selenides [35]. Thus, the absence of ZnSe secondary phases in the present case can likely be explained by the presence of Ge [50]. On the other hand, the limited conversion efficiency and especially the low V_{OC} can not be explained by the formation of different phases.

To analyze the composition in even more detail, 20 spots with a size of $200 \times 200\,\text{nm}^2$ were defined on the absorber and the concentrations were determined by fitting the respective spectra with the software AZtec®. Subsequently, the atomic concentrations were calibrated with the calibration factors listed in table 4.1. Figure 5.4 plots the Zn/Sn as a function of the Cu/(Zn+Sn) ratio for the randomly chosen 20 calibrated spots (orange circles). Their mean value with its standard deviation is given by the red circle and the nominal growth composition by a black star. The dark gray area corresponds to one standard deviation and the light gray area to two standard deviations obtained from the measurement of the stoichiometric CZTSe reference in section 4.2. As a visual guide, figure 5.4a illustrates the data taken on the stoichiometric CZTSe reference. The mean value reflects the stoichiometry of CZTSe in accordance to the calibration, i.e., Cu/(Zn+Sn) = 1.00 and Zn/Sn = 1.00 and the data points of the 20 individual spots are randomly distributed around it. Implying a homogeneous reference sample and a Gaussian distribution of the data, the standard deviation reflects the experimental

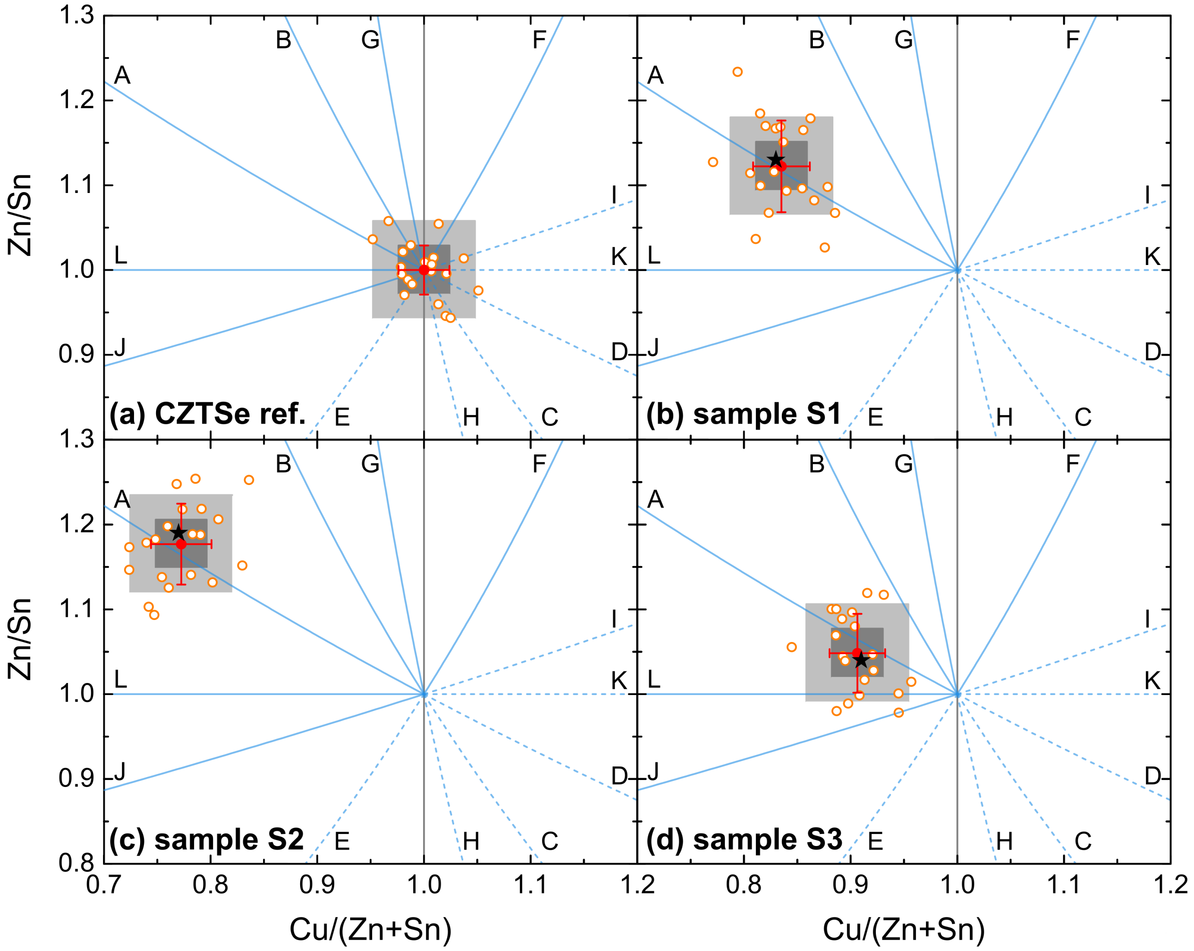

Figure 5.4.: Calibrated cation ratio plots of the CZTSe reference (a) and the three investigated solar cells (S1-S3) with different nominal composition (c-d). The orange circles illustrate the composition of the 20 individual spots, while the red circle marks their average, with the corresponding standard deviation as error bars. The black star illustrates the nominal composition. The dark and light gray areas represent one and two times the standard deviation, evaluated from the reference, and plotted with respect to the average composition for the different absorbers. The solid and dashed blue lines show all off-stoichiometry types (A-L) of kesterite. (The off-stoichiometry types are adapted from [36, 184, 186, 187].

accuracy containing 68 % (dark gray area) and 95 % (light gray area) of the data points for one and two times the deviation, respectively. Real fluctuations of the local absorber composition are present when the variation of the 20 individual data points of an unknown sample clearly exceeds these experimental uncertainties.

Figure 5.4b shows the calibrated cation ratios for sample S1. Remarkably, the nominal and probed concentrations are in very good agreement (the star matches the dark gray area). Just et al. proposed that the CZTSe composition always coincides with the point of stoichiometry and that it is not possible to grow Zn-rich CZTSe because excess Zn will segregate in secondary phases [35]. Here, the beneficial effect of Ge likely helps to grow off-stoichiometric kesterite by suppressing the formation of other phases apart from the kesterite. In their case, however, the solar cells were prepared by non-vacuum

Table 5.1.: Calibrated compositions of the cation atomic concentrations and cation ratios of the CZTSe reference and the three investigated solar cells with composition S1-S3 determined by EDS. The values display the mean value and standard deviation of 20 selected areas that were evenly distributed on the absorber. The nominal composition was determined by global XRF measurements. For details see section 3.1.2.

sample	Cu (at.%)	Zn (at.%)	Sn (at.%)	Cu/(Zn+Sn)	Zn/Sn
CZTSe	25.0 ± 0 .4	12.5 ± 0.3	12.5 ± 0.2	1.00 ± 0.03	1.00 ± 0.03
S1	21.9 ± 0.5	13.9 ± 0.5	12.4 ± 0.3	0.84 ± 0.03	1.12 ± 0.05
nominal	22.6	14.3	13.0	0.83	1.13
S2	21.2 ± 0.7	14.8 ± 0.4	12.6 ± 0.4	0.77 ± 0.03	1.18 ± 0.05
nominal	21.5	15.5	12.9	0.77	1.19
S3	23.4 ± 0.4	13.2 ± 0.4	12.6 ± 0.4	0.91 ± 0.03	1.05 ± 0.05
nominal	24.3	13.1	12.7	0.94	1.04

solution processing, thus effects from the different synthesis route can not be ruled out [35]. The error bars in figure 5.4 indicate the variation of the 20 different spots and symbolize the (in)homogeneity of the sample. Indeed for S1, the error bar of the Cu/(Zn+Sn) ratio (see table 5.1) is almost similar to the reference (light gray area), whereas the observed data fluctuations for the Zn/Sn ratio is almost twice as high as the reference. This clearly demonstrates the presence of real spatial fluctuations of the local absorber composition, which mostly concerns the Zn and Sn distributions. These variations are inherently connected to different off-stoichiometry types named A-L [36, 184, 186, 187], which were proposed based on cation substitution reactions, while assuming charge balance and unchanging valence states [186]. These types are drawn as solid and dotted blue lines in figure 5.4. In agreement with the initial conditions, the integral absorber composition matches the A-type featuring favorable Cu vacancies V_{Cu} and Zn_{Cu} anti-site defects [186]. They form a shallow donor (Zn_{Cu}) and acceptor levels (V_{Cu}) leading to the beneficial p-type conductivity [32]. In terms of the 20 individual spots and considering the experimental accuracy, most of the spots correspond to the A-type as well. Nevertheless, some spots also indicate a mixture of A-type defects with either B- or L-type. They form Zn_{Cu}, Zn_{Sn}, and Sn_{Cu} anti-sites [186, 187] that are connected to deep donor and acceptor states [32], where electrons might recombine reducing the conversion efficiency.

The same EDS evaluation was also performed for two different solar cells, prepared under the same growth conditions, one (S2) with an even Cu-poorer and Zn-richer nominal composition (Cu/(Sn+Zn) = 0.77 and Zn/Sn = 1.19) and one (S3) with a composition close to the stoichiometry (Cu/(Sn+Zn) = 0.94 and Zn/Sn = 1.04). The respective STEM images and EDS intensity maps are depicted in figure 5.5a-f and

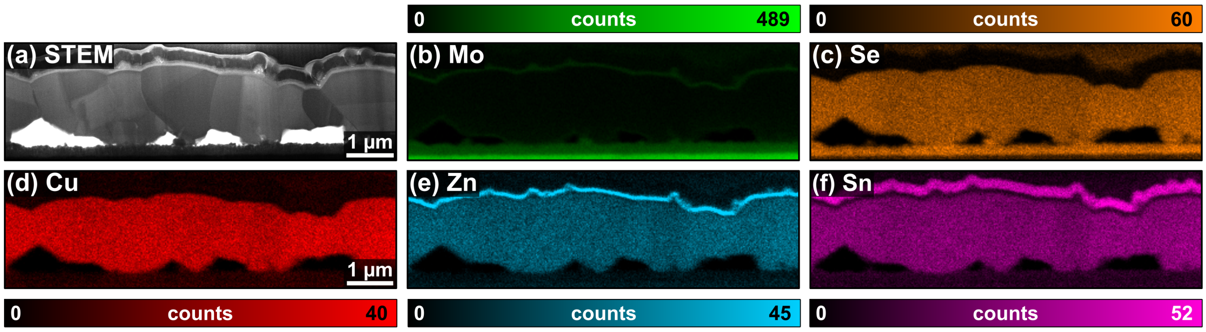

Figure 5.5.: STEM-BF image (a) and EDS intensity maps of the back contact (b) and the four absorber elements (c-f) of a Ge-doped CZTSe solar cell with the nominal composition S2. The average thickness of this lamella was approximately 170 nm.

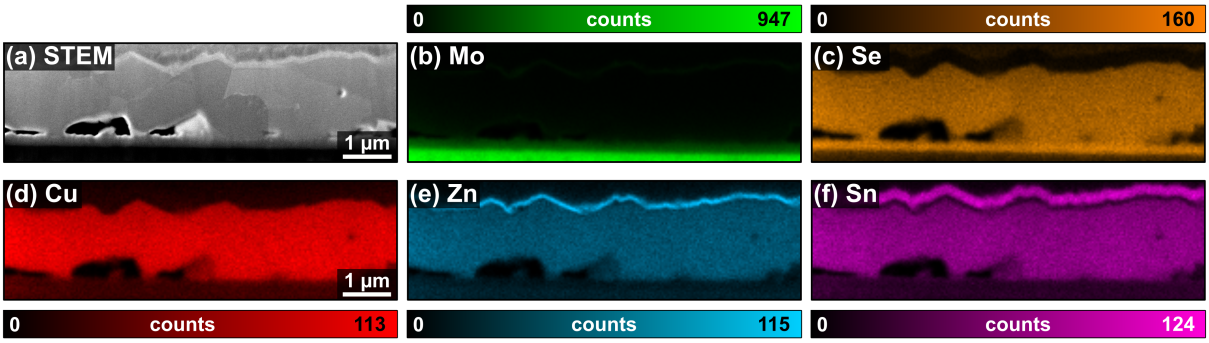

Figure 5.6.: STEM-pHAADF image (a) and EDS intensity maps of the back contact (b) and the four absorber elements (c-f) of a Ge-doped CZTSe solar cell with the nominal composition S3. The average thickness of this lamella was approximately 250 nm.

5.6a-f. They are influenced by the same superposition of the fluorescence lines and secondary excitation, which has been already discussed for sample S1. Interestingly, the absorbers of both samples reveal a comparable homogeneity like S1 and the absence of secondary phases. Even more interesting is the classification of the off-stoichiometry types. In accordance to sample S1 the nominal and integral composition of S2 and S3 (figure 5.4c and d) almost match perfectly including the assignment of the integral composition to the beneficial A-type. Nevertheless, an increased standard deviation for the Zn/Sn ratio points to the formation of different domains for both samples. Most of the individual spots are assigned to the A-type for S2, but a small fraction is likely a mixture of the A-type in combination with harmful B or L off-stoichiometry types. Sample S3 mainly possesses the A-type for the individual spots. In addition to the already observed B- or L-type defects, some domains might also be a mixture or only J-type. The latter implies Sn_{Cu} and V_{Cu} point defects [187] forming a likely detrimental deep donor and a shallow acceptor state [32], respectively. Furthermore, the Zn-poor condition of the J-type likely facilitates the formation of harmful ($2Cu_{Zn}^{-} + Sn_{Zn}^{2+}$) defect complexes [32], thus reducing the effective band bag [30].

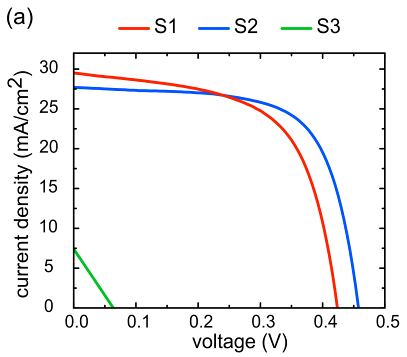

(b)

sample	S1	S2	S3
η (%)	7.6	8.5	0.1
J_{SC} (mA/cm^2)	29.5	27.6	7.4
V_{OC} (mV)	423	457	64
FF (%)	60.7	67.4	25.1
R_{shunt} (Ωcm^2)	127	405	8
R_{series} (mΩcm^2)	479	332	47964

Figure 5.7.: Illuminated JV curves of the samples with nominal composition S1-S3 (a) and selected electrical device parameter (b).

Summarizing, the nominal and integral compositions coincide, which proves the possibility to grow Cu-poor and Zn-rich kesterite absorbers over a wide compositional range facilitating the Ge containing sequential process. The absorbers are almost as homogeneous as the CZTSe reference for the Cu/(Zn+Sn) ratio and real spatial fluctuations in the local kesterite composition mainly concerns the Zn/Sn ratio whose standard deviation increases by almost a factor of 2.

5.4. Correlation of the absorber properties with the conversion efficiency

It has been observed that the absorbers are free of Cu, Zn, and Sn related secondary phases and possesses the intended nominal composition for most regions. Now it is of great interest to explore the electrical parameters of the devices. Figure 5.7 shows the illuminated JV curves and selected electrical device parameters for the three different absorber compositions. The illustrated performance parameters are affected by several characteristics, such as interface recombination [251], band alignment between the different layers [264–266], non-passivated grain boundaries [267], etc. and care has to be taken when comparing single parameter with selected intrinsic properties. The highest conversion efficiency (μ) of 8.5 % is achieved for the Cu-poorest and Zn-richest composition S2. A slightly decreased efficiency of 7.6 % was observed for S1, while the one close to stoichiometry yields the lowest conversion efficiency of almost 0 %. The three different absorbers show a similar morphology and are free of secondary phases. They feature a similar homogeneity, and the absorbers are dominated by the off-stoichiometry type A. Of course, the local off-stoichiometry types cause variations of the intrinsic defects and their concentrations [36, 184, 186, 187], which might lead to varying electrical and optical properties. Thus, the suppression of off-stoichiometry types other than A by improving the Zn/Sn homogeneity might improve the device performance. Comparing the conversion efficiency with respect to each other, the higher efficiency of S2 compared to S1 can presumably be explained by the higher doping level, which decreased series resistance of S2. However, a different contact area to the back contact could explain the improvement as well. The big difference to S3 can not be explained by strong lateral compositional variations or the formation of a different phase. However, the reduced doping level and possibly the formation of detrimental ($2Cu_{Zn}^{-}$ + Sn_{Zn}^{2+}) complexes reduce the efficiency of the device. Thus, these strong efficiency variations explicitly shows the strong need of Cu-poor and Zn-rich conditions.

In fact, the absorbers are already exceptional homogeneous and are characterized above all by the beneficial off-stoichiometry A type. An even more homogeneous distribution might improve the efficiency, but will presumably not explain the difference to the Shockley–Queisser limit and to state of the art Si- and CIGS-based solar cells. This indicates other origins of the low V_{OC} and the related conversion efficiency and that the absorber itself is not the main limitation in these solar cells.

5.5. X-ray fluorescence analysis of Ge-doped CZTSe solar cells

In section 5.3 it was shown that Ge-doped solar cell absorbers are free of Cu-, Zn-, and Sn-based secondary phases. The main elements reveal a fairly homogeneous distribution, and possess the intended integral composition, while locally slight differences occur. However, the question remains whether Ge is really absent or the amount of Ge is not detectable in EDS. Variations at grain boundaries, which were also found for kesterite-based solar cells [40, 245, 268, 269] are also not resolved by EDS. Synchrotron-based nano-XRF was employed to lamellae prepared out of the same solar cells, but on slightly different positions, in order to increase the sensitivity and detection limits. It has already been demonstrated in literature that this technique is a powerful tool to reveal lateral variations even on nanometer scales [36] or fluctuations at grain boundaries [56–58]. For details on the measurements see section 3.2.1.

Figure 5.8a shows the integrated nano-XRF spectrum measured of the lamella shown in figure 5.9a and the fit by the software PyMCA including background and pile-up. Similar fluorescence peaks of the absorber elements are discernible on the background in agreement with the EDS spectrum in figure 5.2a. Characteristic X-ray peaks of the front- and back-contact elements, the Ni grid, and the Pt layer are also visible. The

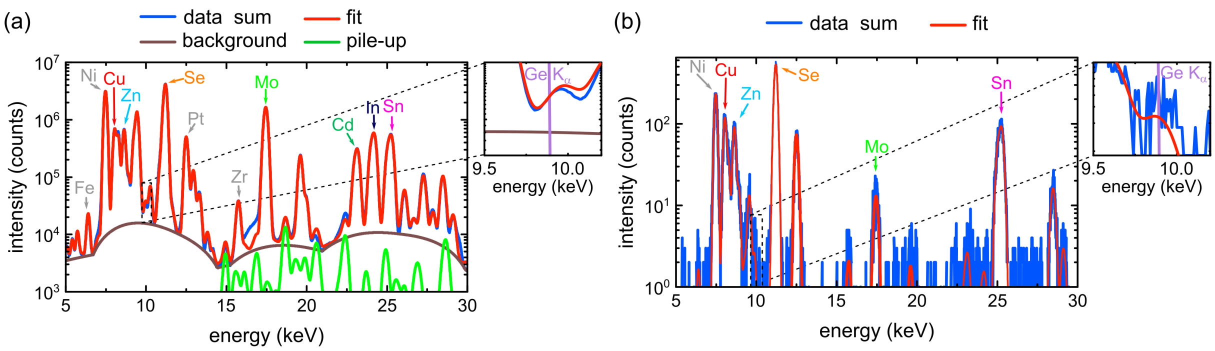

Figure 5.8.: Nano-XRF spectra taken on a lamella prepared from a Ge-doped CZTSe solar cell. The sum spectrum is shown in (a), while (b) shows the spectrum of a single pixel, with a size of $50 \times 50\,\mathrm{nm}^2$ that was taken on the absorber. The fit, background and pile-up was calculated using the PyMCA code [211]. Magnifications shows the respective spectrum in an energy rage of 9.5 - 10.2 keV covering the K-edge of Ge.

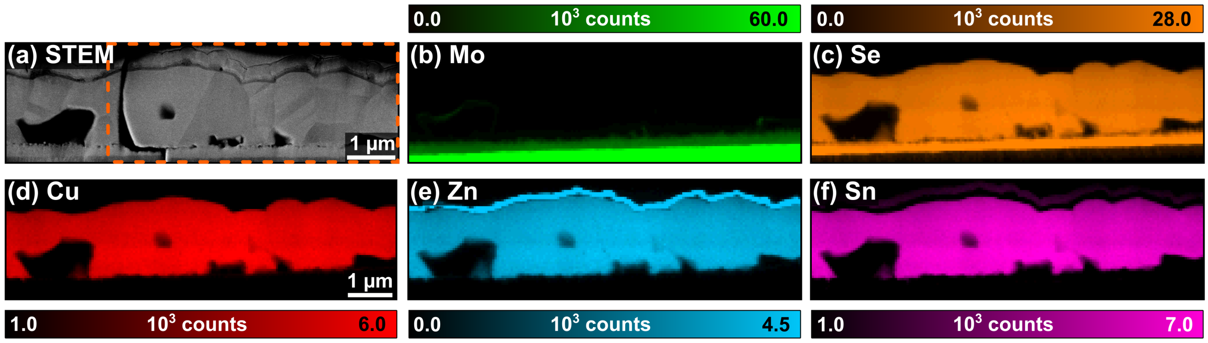

Figure 5.9.: STEM-pHAADF image and fitted XRF intensity maps of the Mo back contact (b) and the four absorber elements (c-f) of sample S1. The intensity maps show the integrated counts of each element for each pixel, obtained by fitting the corresponding spectrum with the software PyMCA [211]. The slightly increased Mo signal at the surface of the voids is an artifact from the lamella preparation. The orange rectangle marks the region, which is suited to calculate the relative maps in figure 5.10. The average thickness of this lamella was approximately 160 nm.

Fe and Zr peaks were already discussed for the CZTSe reference (see section 4.3) and likely originate from the experimental setup. The most interesting new peak is clearly visible in the magnification of the figure 5.8a, whose energy coincides with the Ge K_α-line at 9.886 keV. Therefore, in addition to the homogeneity of the absorber the following sections also examine the presence of Ge.

5.5.1. Evaluation of nanoscale compositional fluctuations

In a pixel-by-pixel based analysis, it is possible to extract elemental intensity maps by fitting each single spectrum (see figure 5.8b) individually using the PyMCA code [211]. Figure 5.9 depicts the integrated counts for each pixel of the Mo back contact (b) and the absorber elements (c-f). It is evident that the absorber consists of the same layered geometry and feature the same characteristics, which have already been discussed in

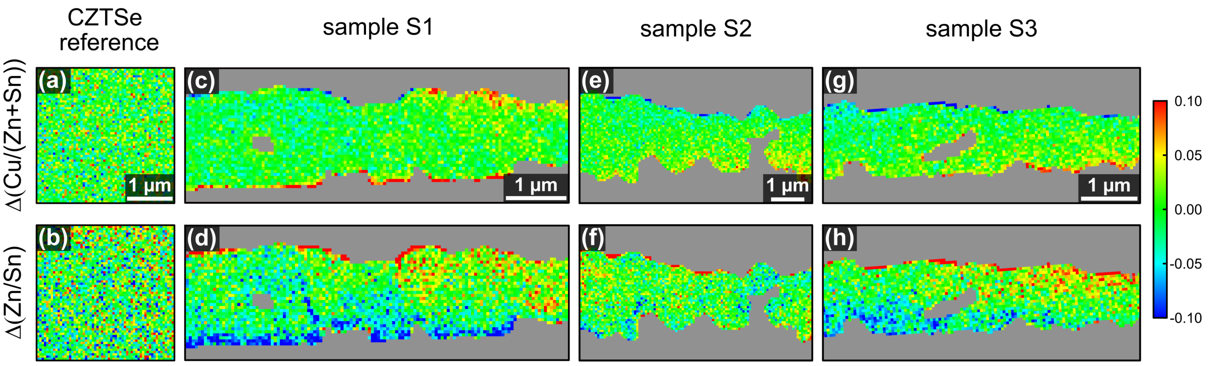

Figure 5.10.: Deviation of the cation ratio from the respective mean value for the Cu/(Zn+Sn) and Zn/Sn ratio. These maps were calculated by subtracting the mean value of a particular map from the actual value of every individual pixel for the CZTSe reference (a,b) and the three different compositions S1-S3 (c-h). The gray areas mark the regions where no CZTSe:Ge absorber was present, such as the Mo back contact, the MoSe layer, voids, Pt and air.

section 5.2. In accordance to the EDS maps in figure 5.1, the XRF maps present the same homogeneous distribution and apparently no intensity variation indicating the formation of secondary phase segregation.

The next step would be the conversion of the intensity to atomic concentrations. However, the lamella ridges and the Ni grid onto which the lamella was mounted, attenuated the created fluorescence radiation during the measurement, which makes a quantification impossible (for details see section 3.2.1). Maps of the relative differences of the cation ratios, named Δ(Cu/(Zn+Sn)) and Δ(Zn/Sn), were calculated similar to the maps in section 4.3. Figure 5.10c and d show the relative maps calculated in the orange marked region in figure 5.9a. Sample areas without absorber are colored by a light gray.

The Δ(Cu/(Zn+Sn)) map in figure 5.10c appears to be as homogeneous as the CZTSe reference (see figure 5.10a and b) in the bulk absorber and apart from the upper right area where the Cu content increases, the deviation does not overcome the experimental uncertainty of 0.04 for a single pixel (see table 4.2). On the other hand, at the interface to the front contact specific regions show a reduced or increased Cu content, while at the back interface the Cu content is increased. The variations in the Δ(Zn/Sn) map validate spatial fluctuations of the local absorber composition deduced from figure 5.4b and the formation of different off-stoichiometry types. Particularly in the vicinity of the interface to the CdS buffer layer, the absorber is even richer in Zn compared to the bulk, while at the back contact the inverted case prevails. An even more detailed comparison with EDS is possible by comparing the standard deviations based on the 20 individual spots with a size of $200 \times 200\,\mathrm{nm}^2$. Table 5.2 lists the corresponding deviations corroborating that fluctuations mostly concerns the Zn and Sn distributions.

Table 5.2.: Standard deviations of the cation ratios determined from the nano-XRF measurements, for the CZTSe reference lamella and the three different samples S1-S3. Similar to the EDS evaluations, 20 randomly chosen areas were defined to determine these deviations.

sample	Δ(Cu/(Zn+Sn))	Δ(Zn/Sn)
CZTSe	0.01	0.02
S1	0.01	0.04
S2	0.01	0.03
S3	0.01	0.04

The deviation of the Cu/(Zn+Sn) ratio matches the experimental uncertainty, which demonstrates that the elemental distribution is even more homogeneous than expected from EDS. This also includes the homogeneity at grain boundaries, whose positions become visible comparing the relative maps with the STEM-pHAADF image in figure 5.9a.

Similar nano-XRF studies were also performed for the lamellae of samples S2 and S3. Again the intensity maps reveal an exceptional good homogeneity (see figure A.3 and A.4 in the appendix), which is also reflected in the deviation maps in figure 5.10e-h. The Cu/(Zn+Sn) ratio reveals the same standard deviation like the reference (see table 5.2) in accordance to the previous results. Real spatial fluctuations are only present for the Zn and Sn distribution. Furthermore, the interfaces of both samples show in selected areas a slight decrease of the Cu content towards the front contact as well as an increase at the back contact. The Δ(Zn/Sn) maps reveal a similar distribution like S1 for both, the absorber and interfaces, but it is worth noting that a reduced Zn content for S2 was only observed in the bottom left corner (see figure 5.10f). These results are in excellent agreement with latest Raman measurements on similar cells with composition S2 showing a reduced amount of Cu vacancies V_{Cu} defects at the back interface region with respect to the front interface [68]. In addition, surface related Raman and Auger electron spectroscopy measurements indicate variations of the cation ratios between the different grains related to variations in the V_{Cu} and Zn_{Sn} defect density, which is in fact in perfect agreement with the observed compositional variations at the surface [68]. As already mentioned, variations within the absorber might cause different performances of individual areas and band fluctuation, but interface variations can also strongly influence carrier recombination. Recent HRTEM revealed line and point defects at the surface of the absorber and a transitional region at the CdS/CZTSe interface of about 6 nm. This region has a worse crystallinity than the reaming absorber and contains a high density of line and point defects [68]. These results fit very well to the here observed variations at the front interface. Admittance spectroscopy measurements

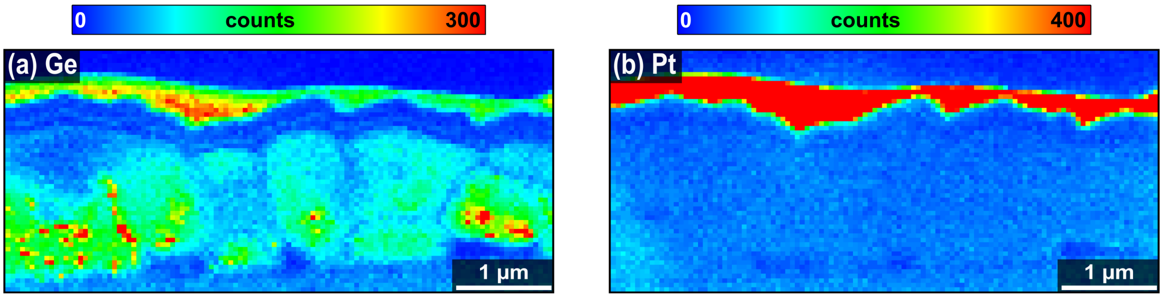

Figure 5.11.: Comparison of the Ge (a) and Platinum (b) ROI intensity maps of a CZTSe:Ge lamella with composition S1 measured with nano-XRF. The pixels show the integrated intensity in an energy interval between 9.81 to 10.07 keV for Ge and 12.85 to 13.18 keV where the isolated Pt $L_{\gamma 1}$-line is located.

also indicate a higher density of trapping centers at the front interface [68]. The here observed variations at the front contact corroborate that the main problem is likely not the absorber, but the interface region between the CdS and CZTSe layer. Removing the transition layer or a surface passivation might reduce the recombination as already proposed by several groups [270–274]. Moreover, no variations at grain boundaries are discernible.

Finally, the same examinations were also carried out on 3 more lamellae: one for each stoichiometry. They also showed a very homogeneous absorber with variations mainly concerning the Zn/Sn distribution. Furthermore, similar elemental variations were found at the interfaces and no compositional fluctuations at grain boundaries were observed at all.

5.5.2. Detection of Germanium

In figure 5.8a a small peak at roughly 10 keV indicates the presence of Ge (K_α: 9.886 keV).[1] The fluorescence radiation of the Pt L_η-line ($\sim$ 9.975 keV) has a similar energy, which at first glance does not seem to be a problem since Pt is not present in the absorber. But by considering scattering of the incident beam and secondary excitation, the origin of the signal might also be explained by Pt. To determine the origin of the signal figure 5.11a shows the ROI map in the energy range from 9.81 to 10.06 keV covering the Ge K_α-line at 9.886 keV. A distinct signal is present in the absorber layer but also in the Pt layer. To verify that the signal in the absorber stems from Ge, figure 5.11b illustrates the ROI map in the energy range from 12.85 to 13.18 keV. In this interval the Pt $L_{\gamma 1}$-line is isolated. If the signal originates from Pt, the lateral distributions have to coincide. The map reveals a strong signal in the actual Pt layer

---

[1] The Ge K_β-lines at 10.982 keV cannot be used for the evaluation, because their intensity is too low and it heavily overlaps with the orders of magnitude higher Se K-line intensity.

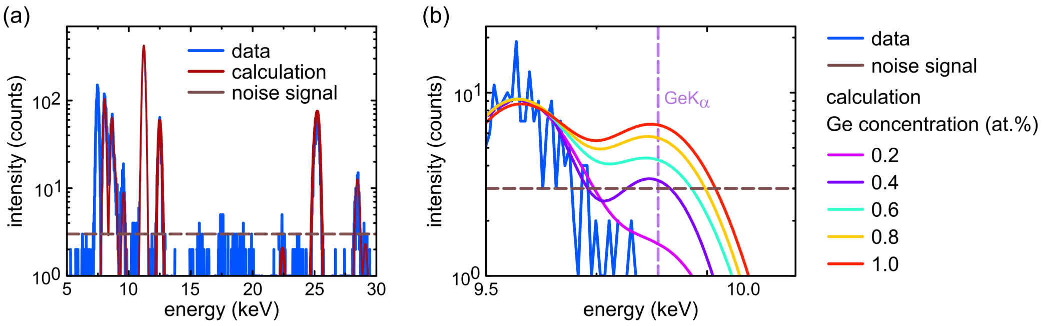

Figure 5.12.: Estimation of the minimum detection limit of Ge for 1 pixel. The calculated CZTSe spectrum was adjusted to coincide with the measured CZTSe reference (a). Calculated spectra with a Ge concentration between 0.2 at.% and 1.0 at.% in comparison to the measured spectrum, in an energy range between 9.5 - 10.2 keV covering the K-edge of Ge.

and noise in the remaining area. Compared to 5.11a a similar signal is also present in the Pt layer but a clear difference within the absorber layer is apparent, demonstrating that the signal and variations indeed stem from Ge and are reliable. The intensity within the protective Pt layer thus originates from the superposition of Ge and Pt lines in combination with secondary excitation by high energetic Pt fluorescence radiation.

5.5.3. Detection limit of Germanium

The presence of Ge in the absorber has been confirmed, thus it is of particular interest to identify the minimum detection limit (MDL), which represents also the experimental uncertainty. A comparable lamella that contains Ge which is crystallized into the structure of kesterite may serve as an ideal reference, because the background of an X-ray spectrum depends on the properties of the sample, such as composition, density, and thickness. Considering the Ge concentration is well known, the detection limit can be determined by the measurements signal-to-noise ratio [275]. The homogeneous CZGeSe sample that was used as a reference for the nano-XANES measurements in section 5.6, would serve as such an ideal reference for the nano-XRF measurements. Unfortunately, this sample was not accessible during the beam time where the Ge-doped CZTSe solar cells were investigated. Thus, the MDL is estimated by an iterative process by comparing the measured XRF spectrum of the CZTSe reference with calculated spectra whose Ge content varies.

Figure 5.12a shows the measured CZTSe spectrum for 1 pixel and the corresponding calculated spectrum, which was obtained using the software PyMCA [211]. The first step to calculate this spectrum implied the specification of all know parameters such as the detection angle, distance to the detector, active area of the detector, and exposure time. Subsequently, the photon flux of the primary beam was adjusted in such a way that the measured spectrum and the calculation are in good agreement, as shown in figure 5.12a. To estimate the MDL, different concentrations of Ge were added to the matrix (figure 5.12b). The calculated spectrum was further compared to the average noise signal, which was determined in the energy region from roughly 15 - 20 keV, to estimate at which concentration the Ge K_α-line becomes significant. Although a noise signal of less than or equal to 2 counts can be identified in the region of the Ge K_α-line in figure 5.12b, the estimation should be rather conservative. Thus, an average noise signal of 3 counts was used, instead of 2 counts. Figure 5.12b shows the result of this calculation with Ge concentrations between 0.2 - 1.0 at.%. For 0.2 at.% the calculated Ge peak is not significant, since it is below the noise signal. The calculated spectrum becomes more distinct and exceeds the noise signal with increasing Ge content. At a Ge concentration of 0.6 at.% the peak is higher than the noise signal. However, the peak maximum exceeds the noise by only 1 count. Considering a conservative estimation, the choice of MDL is therefore 0.8 at.%, although 0.6 at.% could also have been used. Since the MDL for a single pixel exceeds the integral amount of 0.5 at.% that was introduced during the synthesis process, the area/statistic was increased. The MDL was estimated based on the previously described process for 4 pixel to 0.2 at.% and for 9 pixel to 0.08 at.%.

5.5.4. Germanium distribution in correlation with microstructural elements

The STEM-pHAADF image in figure 5.13a depicts the same cross-sectional lamella as shown in figure 5.9 of sample S1 and the corresponding fitted Ge intensity map in figure 5.13b. The data demonstrates that Ge remains in the absorber after the synthesis and is incorporated in the grains. Other groups extensively studied the presence and distribution of Ge by utilizing EELS [245] and SIMS [41] measurements. In contrast to the present results, they only detected nanoscale inclusions at selected grain boundaries [245] and indicated that Ge remains in the top-half part of the absorber, but is missing in the bottom half [41]. However, the results in figure 5.13b unambiguously demonstrate that Ge is laterally inhomogeneous distributed throughout the absorber layer. The latter reveals areas with a relative uniform distribution, but also areas where Ge appears to be depleted or completely absent and characteristic hotspots. In contrast to the SIMS results [41], a generally higher Ge concentration in the lower half of the absorber (towards the back contact) seems to be present, while in the upper half and only a few regions also possess a relative high intensity. The results seem not contra-

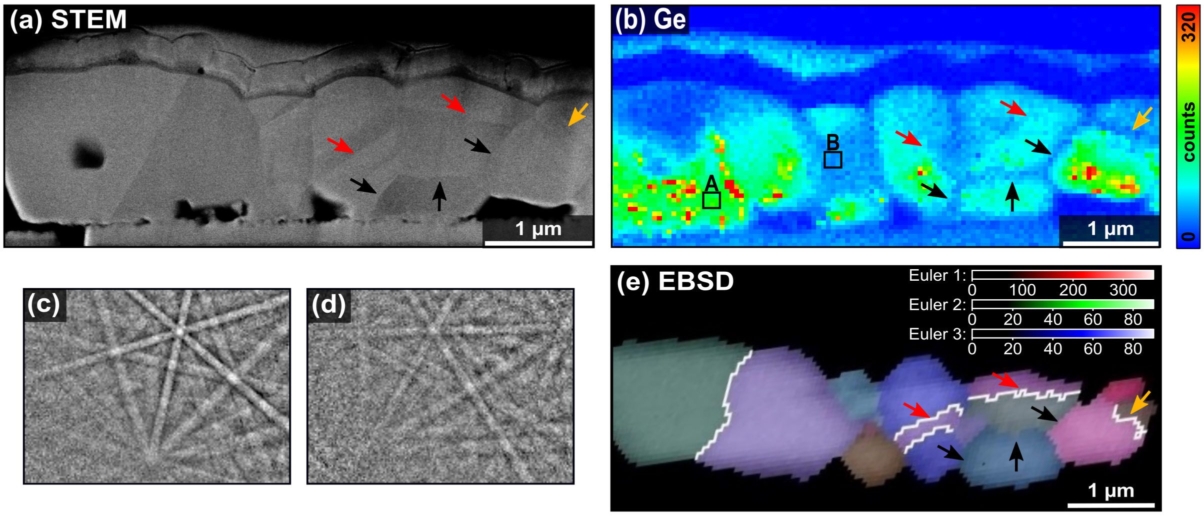

Figure 5.13.: Microstructural characterization and Ge distribution of the cross-sectional lamella taken out of sample S1 with an averaged thickness of 160 nm. (a) STEM-pHAADF image revealing the grain boundaries of the lamella. (b) Ge intensity map measured via nano-XRF. The fitted Ge counts, which were evaluated with the software PyMCA [211], are depicted for each pixel. Within the energy region of Ge, the Pt L_η-line partly overlaps with the Ge K-lines, which leads to a signal in the protective Pt layer. The black squares (A,B) mark exemplarily areas where the Ge concentration was quantified. The red arrows indicate grain boundaries with a comparatively homogeneous Ge intensity, while the black arrows point to grain boundaries with a depleted signal. (c) Kikuchi pattern taken on a selected CZTSe:Ge grain, demonstrating the excellent pattern quality if only one grain with a certain orientation contribute to the EBSD pattern and a worse quality (d) if two grains with different orientation contribute to a single EBSD-pattern. (e) All-Euler map superimposed with the band contrast map obtained from an EBSD scan. The highly symmetrical $\Sigma3$ twin boundaries are highlighted by white lines.

dictory, considering the missing lateral resolution of SIMS. In order to understand the reason for the heterogeneous Ge distribution, the map in figure 5.13b was compared to the STEM image in figure 5.13a. It becomes evident that the distribution of Ge correlates with the presence of different grains and their boundaries. A mainly even Ge distribution can be identified for single grains and significant variations seem to be present only between different grains. Grain boundaries reveal a significant Ge depletion although only certain grain boundaries are affected. To investigate this correlation in detail, the grain orientation was determined by EBSD. This enables the determination of the misorientation of adjacently grains and the classification of the grain boundary. An excellent Kikuchi pattern quality was obtained for most spots on the lamella (figure 5.13c). Still care has to be taken when two grains contributed to the same pattern (figure 5.13d), because then the indexing algorithm considers the Kikuchi bands from a single lattice and indexing might be wrong or completely fails. Figure 5.13e depicts the all-Euler map superimposed with the band contrast (BC) map of the performed EBSD scan. Brighter areas represent a good quality of Kikuchi patterns and darker shades illustrates a lower pattern quality. The color code indicate the Euler angles (ϕ_1, Φ, ϕ_2), which present the rotation of the corresponding location with respect to the fixed sample coordinate system. They were used to calculate the crystallographic direction of the grains [276, 277] (see inverse pole figure+BC (IPF+BC) map in figure A.5 in the appendix). In the next step, the misorientation of adjacent grains was determined providing the possibility to classify the grain boundary. In the present case, the twinning relations had to be defined as 60° rotations around the $\langle 111 \rangle$ direction and as 70.53° rotation around the $\langle 110 \rangle$ direction in an approximated cubic structure [232] instead of 60° rotations around the $\langle 221 \rangle$ direction and as 70.53° rotation around the $\langle 110 \rangle$ direction in the tetragonal lattice [231, 278]. For details concerning the measurement see section 3.3.3. The highly symmetrical $\Sigma 3$ grain boundaries with a 60°-$\langle 111 \rangle_c$ misorientation are highlighted by white lines in figure 5.13d. Apparently, the investigated area did not contain grain boundaries with a misorientation of 70.53°-$\langle 110 \rangle_c$. EBSD is fairly surface sensitive with information depths less than 100 nm [279], compared small to STEM and XRF where the entire 160 nm thick lamella was examined. Thus, not every grain boundary might be visible and indexed in the EBSD map. Nevertheless, the correlation between grain boundaries and the presence of Ge reveal a depletion for the random grain boundaries (see black arrows in figure 5.13b) while the $\Sigma 3$ twins remain unchanged (see red arrows). One exception seems to be present in the upper right corner of the map (see orange arrow). Here, a $\Sigma 3$ twin boundary exhibits a depleted signal. This can be likely explained by superposition of two grains with different orientation. The probed grain forms a $\Sigma 3$ twin with the adjacent grain and the grain below likely a random grain boundary, which creates the impression that the $\Sigma 3$ twin grain boundary is Ge depleted.

The applied techniques do not allow to investigate the cause for the depletion. However, a Ge depleted growth front during the synthesis might be a possible explanation for depleted grain boundaries. The latter can be formed by two scenarios: by a stacking fault (likely forms $\Sigma 3$ twin grain boundary) and if two growth fronts encounters with different orientations (likely forming random grain boundaries). The grain growth continues in the same way as before after a stacking fault, thus Ge is built-in similarly. However, if two growth fronts with different orientation encounter, the growth suddenly stops and a depleted grain boundary is formed. This might be explained by a Ge depleted growth front and a time delayed incorporation.

In order to quantify Ge, XRF spectra were extracted in different areas on the absorber, summed up over 9 pixels for the CZTSe:Ge absorber and over 4 pixels for the hotspots and fitted using the software PyMCA [211]. The evaluated concentrations drastically depend on the position and reached maximum concentrations of up to 0.5 at.% ± 0.08 (see area A in 5.13b) and minimum concentrations of about 0.1 at.% ± 0.08 (see area

B in 5.13b), which is in excellent agreement with the integral amount of 0.5 at.% that was introduced during the synthesis process. Note, the Ge fluorescence signal also suffers from the previous mentioned attenuation by the Ni grid. Thus, the absolute values present a rough estimate rather than an exact quantification. The supposedly missing Ge agglomerates in hotspots, whereby the concentration rises up to 1.8 at.% ± 0.2 depending on the position and size of the hotspots.

Germanium is usually used to alloy CZTSe solar cells [48] partially exchanging Sn in the lattice. This incorporation widens the band gap almost gradually from 1.0 eV to 1.35 eV for 0 at.% and 12.5 at.%, respectively [280]. In the investigated absorber of sample S1, the maximum concentration of 0.5 at.% causes a rather small enlargement of the band gap of 15 meV. This nearly unaffected band gap is in excellent agreement with Giraldo et al., who found similar results by PL and EQE measurements [41, 49]. Thus, the enhanced conversion efficiency cannot be explained by an overall enlarged band gap.

In addition to the overall band gap, the local band alignment can influence the electronic properties. Ge was found to remain rather in the lower half of the absorber. The incorporation of Ge increases the conduction band minimum, while the valence band is nearly unaffected [199]. This band bending results in a small force that drags the electrons towards the front contact, which probably enhance the efficiency slightly. Although the overall effect of Ge is beneficial, the depletion at grain boundaries leads to a small force for the electrons towards the random grain boundaries, since the conduction band minimum is slightly decreased [199]. Random grain boundaries are known to feature detrimental defect states due to dangling and wrong bonds. A force for electrons towards these recombination centers will likely slightly lessens the overall beneficial effect of Ge in the device.

Similar evaluations of the Ge distribution were also performed on the lamellae presented in section 5.5.1 from sample S2. Figure 5.14a depicts the STEM-DF image and the respective Ge intensity map is shown in figure 5.14b. In accordance with the previous discussed results, the same inhomogeneous Ge distribution can be identified. Pronounced intensity variations of individual grains were observed, while the Ge content remains even within single grains. Moreover, selected grain boundaries exhibit a Ge depletion and also similar Ge hotspots can be identified. Overall, six lamellae (two for each composition and solar cell) showed identical characteristic proving that the observed Ge distribution can be assumed for all Ge-doped CZTSe absorbers within the here investigated compositional range.

The hotspots might either be Ge-enriched $Cu_2Zn(Sn,Ge)Se_4$ or a secondary phase. To

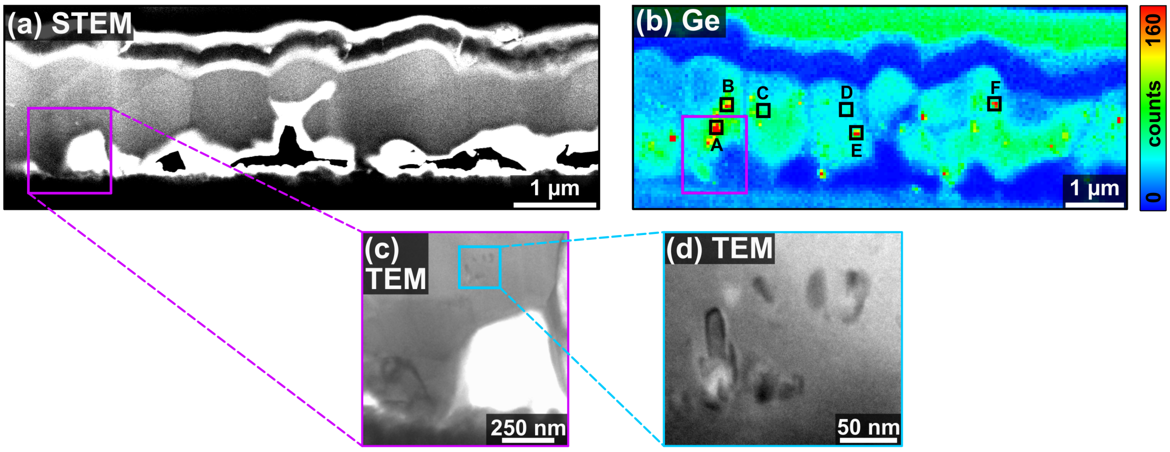

Figure 5.14.: Microstructural characterization and Ge distribution of the cross-sectional lamella taken out of a complete solar cell with composition S2 and an averaged thickness of 260 nm. (a) STEM-DF image revealing the grain boundaries of the lamella. (b) Ge intensity map measured by nano-XRF. The black squares (A-F) roughly mark the areas where nano-XANES measurements were conducted and the purple rectangle where TEM measurements were performed. (c) TEM-BF image taken in an area which includes region A and the Ge hotspot. For the TEM measurements the lamella was thinned down to approximately 80 nm. (d) TEM-image with an increased magnification of a specific region in (c) revealing the formation of small nanoscale inclusions.

extract more information, one lamella was thinned down to approximated 80 nm to perform TEM measurements. For details regarding the TEM measurements see section 3.3.2. Figure 5.14c and d show the TEM micrographs including area A (marked in figure 5.14b) with two different magnifications. Clearly, small nanoscale inclusions become apparent, with sizes fluctuating between 10 and 50 nm. The presence of nanoscale inclusions with slightly smaller diameters (1 - 10 nm) was also observed in literature [41, 49]. However, they were hardly found within the grains but multiple were located at grain boundaries [41]. Contrary, the inclusions are only located in the grains in the present case. Priorly, the average concentration of the hotspots was estimated to increase up to 1.8 at.% in an area of $100 \times 100\,\text{nm}^2$. According to the TEM image in figure 5.14d the size of the observed inclusions is in the range of only 10 - 50 nm. This indicates that they are not expected to be present over the whole thickness of the lamella and it becomes evident that the actual Ge concentration is higher in the inclusions than the integral value. By a simple estimation of a spherical object for the inclusions with a radius of 25 nm ($V(r = 25\,\text{nm}) = \sim 65\,000\,\text{nm}^3$) and a rectangular shape for the probed volume (focal spot size = $54 \times 52\,\text{nm}^2$, lamella thickness 260 nm, $V = \sim 730\,000\,\text{nm}^3$), a Ge concentration of 20 at.% or even higher can be estimated. This indicates the formation of a secondary phase rather than Ge-enriched $Cu_2Zn(Sn,Ge)Se_4$. Besides the formation of Ge-enriched nanoscale inclusions, it has been also reported that similar sized Sn-enriched nanoscale inclusions are present in Ge-doped CZTSe

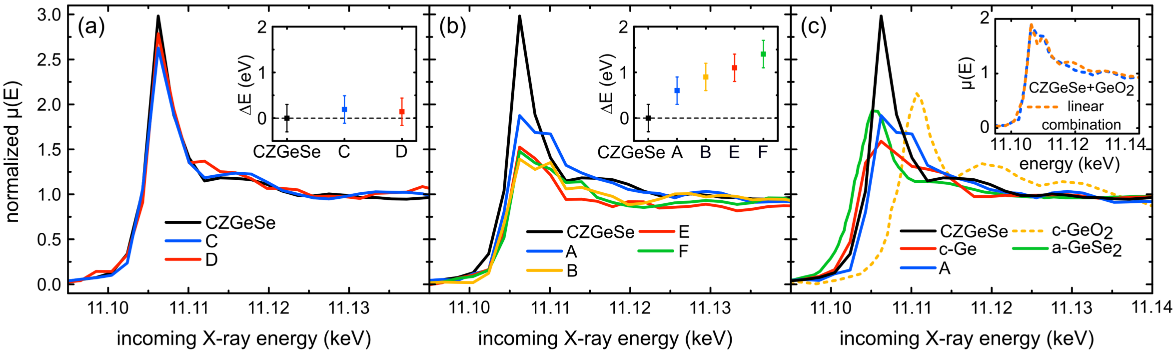

Figure 5.15.: Normalized nano-XANES spectra at the Ge K-edge taken on the CZTSe:Ge absorber of the same cross-sectional lamella as shown in figure 5.14a. (a) Normalized absorption coefficient as a function of incoming X-ray energy for area C and D (see 5.14b) compared to the CZGeSe reference. (b) Normalized nano-XANES spectra of the four different regions A,B,E,F (see 5.14b), which all include hotspots, compared to the CZGeSe reference. The insets of (a) and (b) shows the absorption edge energy shift (ΔE) evaluated at μ(E) = 0.5, relative to the CZGeSe reference edge. (c) Normalized nano-XANES spectrum of area A compared to a crystalline Ge reference lamella, crystalline GeO_2 taken from Ward et al. [281], and amorphous $GeSe_2$ taken from Zhou et al. [282]. The inset plots the spectra for region A and for a linear combination of 60 % CZGeSe and 40 % GeO_2.

solar cells produced from the same group and under similar synthesis conditions [41, 245]. As already discussed in section 5.3 and 5.5.1 neither the Sn intensity maps in figure A.3f nor the intensity maps of the other samples in figure 5.9 and A.4 (see appendix) indicate the presence of Sn related secondary phases.

5.6. Short-range structural order of Germanium in the CZTSe:Ge absorber

Detailed information about the chemical identity of the solar cells were achieved by applying EDS and nano-XRF, but information about the chemical bonding are still missing. Indeed, it is of great interest to know whether Ge is build into the kesterite matrix to confirm the previous assumed band bending but also to identify possible detrimental secondary phases. Spatially resolved XANES measurements at the Ge K-edge energy are sensitive to the local environment and give access to the local structure. For details about the experimental see section 3.2.2.

The nano-XANES measurements were performed on the same lamella of sample S2, which is shown in figure 5.14a. The black squares in 5.14b (A-F) roughly mark regions containing Ge-enriched nanoscale inclusions (A, B, E, F) and CZTSe:Ge grains (C, D) where the nano-XANES measurements were taken. Figure 5.15a shows the normalized absorption coefficient μ(E) as a function of incoming X-ray energy for region C and D compared to a CZGeSe reference. This reference spectrum was also taken on a CZGeSe lamella prepared from a single phase, homogeneous powder grain similar to the CZTSe reference lamella (for synthesis details see section 3.1.1). The excellent agreement of the spectral shape of the reference and the CZTSe:Ge absorber clearly indicates that Ge occupies tetravalent Ge^{4+} sites in CZTSe and is build into the kesterite matrix. Furthermore, the absorption edge position gives more insights into the local coordination. The inset in figure 5.15a shows the energy deviation (ΔE) of the edge energy of region C and D with respect to the CZGeSe reference evaluated at $\mu(E) = 0.5$. Both areas on the absorber show an excellent agreement with the reference considering the analysis uncertainty of 0.3 eV. The fact that the shape and edge position is nearly identical proves that Ge is incorporated on substitutional Sn lattice sites in the CZTSe matrix. This confirms the previous described band bending towards the front contract and to the random grain boundaries. Moreover, this substitutional behavior is associated with the suppression of detrimental +II oxidation states for Sn and therefore with the reduction of deep recombination centers for electrons within the band gap [45, 47]. This is expected to be the reason for the improved V_{OC} in $Cu_2Zn(Sn,Ge)Se_4$ alloys. For the here investigated solar cells, the Ge concentrations reach maximum values of only 0.5 at.% according to section 5.5.4. As a consequence only a small number of atoms are exchanged, which likely contribute to the improved V_{OC} only to a small extent, in agreement with the proposed improvement by a higher crystalline quality [41, 49, 50, 236, 245]. The XANES spectra A, B, E, and F in figure 5.15b contain the Ge hotspots. Compared to the CZGeSe reference and the CZTSe:Ge grains absorber the appearance of the spectra changed, and the edge energy shifts towards higher energies. Thus, a contribution apart from the kesterite matrix becomes evident. Further, the inset in figure 5.15b reveals an edge energy shift with respect to the CZGeSe reference of up to 1.4 eV, which can not be explained by the analysis uncertainty ($\sim$ 0.3 eV). Even by taking the 1.0 eV energy resolution of the Si (111) double crystal monochromator into account, two out of four spectra own a larger shift, which can only be explained by the presence of an additional contribution from a secondary phase. Figure 5.15c compares spectrum A with suited references in order to determine the additional phase, such as the CZGeSe lamella, a single crystalline Ge (c-Ge) lamella, crystalline GeO_2 (c-GeO_2) taken from Ward et al. [281] and amorphous $GeSe_2$ (a-$GeSe_2$) taken from Zhou et al. [282]. For this purpose the energy axes of the XANES spectra, taken from literature, were carefully calibrated as described by Johannes at al. [283]. XANES is sensitive to the short-range order and can distinguish between amorphous and different crystalline phases. This is also possible even if the spectra are almost similar, as shown for GeO_2 by Majérus et al [284] and elemental Ge by Backman et al. [285]. However, nano-XANES

is still very challenging and can not resolve these small differences. Therefore, the differentiation between amorphous and crystalline phase will be omitted.
A direct comparison of the exemplarily depicted region A and the references show no clear agreement. In particular, the c-Ge and $GeSe_2$ absorption edges shift -0.4 eV and -1.7 eV towards lower energies with respect to the CZGeSe, respectively, and can be excluded from the analysis. Note that the edge energy of $Ge_xSe_{(1-x)}$ depends on the composition and stays well below amorphous Ge for $Ge_xSe_{(1-x)}$ $(0.2 \leq x \leq 0.4)$ according to Zhou et al. [282]. As the maximum edge energy can only reach elemental Ge, it can also be excluded.
As already mentioned, the remaining GeO_2 reference is not in agreement with region A but shifts the edge energy towards higher values. According to the TEM images, the nanoscale inclusions feature sizes between 10 - 50 nm and are likely not present over the entire thickness of the lamella. Taking also the comparable large focal spot size of $150 \times 135\,nm^2$ of the synchrotron beam into account (see section 3.2.2), it becomes evident that region A is likely a superposition of the kesterite CZTSe:Ge matrix and GeO_2. The inset in figure 5.15c shows a linear combination of the XANES spectra with 60 % CZGeSe and 40 % GeO_2 in comparison to the spectrum of region A. The almost perfect agreement manifests that the inclusions are composed of GeO_2. A similar agreement was also found for the remaining three regions (B, E and F) but with different compound fractions.
Determining the impact of GeO_2 to the electrical properties and to the final device performance from these data is not simple as several parameters have to be taken into account. The wide bang gap of 5.7 eV [286–288] and the insulating nature does not allow GeO_2 to contribute effectively to the light conversion, and it might be beneficial to avoid or minimize their presence. In the same way their size, local distribution, and the relatively low particle concentration indicate a minor impact to the reduced light conversion and to the general optical properties. Considering the very low electron affinity of only 2.24 eV [289] compared to 4.46 eV for CZTSe [290], they create a barrier for electrons, but due to their small size of only 10 - 50 nm compared to the carrier diffusion length > 500 nm [244] and their spatial distribution within the absorber, the electrons can easily circumvent them. Although their contribution as potential recombination centers cannot be ruled out, it might be beneficial to reduce or avoid their presence.
Finally, the same measurements were also conducted on two lamellae with composition S1 (see figure 5.13) and S3 (not shown here). Figure 5.16a illustrates the normalized nano-XANES spectra for both samples, taken on the CZTSe:Ge grains, while the inset

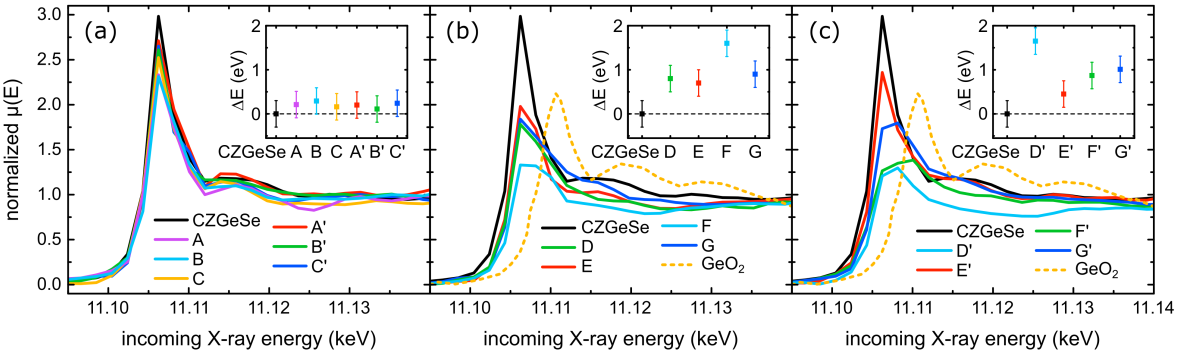

Figure 5.16.: Normalized nano-XANES spectra at the Ge K-edge taken on the CZTSe:Ge absorber of the same cross-sectional lamella as shown in figure 5.13a (S1) and one with composition S3. (a) Normalized absorption coefficient as a function of incoming X-ray energy for the areas of the CZTSe:Ge grains for S1 (A, B, C) and for S3 (A′, B′, C′) compared to the CZGeSe reference. (b,c) Normalized nano-XANES spectra of the regions which include the hotspots for S1 (D, E, F, G) and S3 (D′, E′, F′, G′) in comparison to the CZGeSe reference and to GeO_2 from Ward et al. [281]. The insets of (b) and (c) show the absorption edge energy shift (ΔE) evaluated at μ(E) = 0.5, relative to the CZGeSe reference edge.

reveals the edge energy deviation with respect to the CZGeSe reference. Both the spectral shape and the edge energy confirm the incorporation of Ge into the CZTSe matrix and therefore the exchange of Sn in the lattice. On the other hand, the spectra including the inclusion in figure 5.16b and c corroborate the different shape, the shift towards higher energies and the formation of small GeO_2 secondary phases. Thus, the findings on the short-range structural order in these solar cells are independent of the here investigated stoichiometry range and can be assumed as general characteristic in Ge-doped CZTSe solar cell absorbers prepared by the sequential process.

5.7. Summary

High resolution morphological, compositional, structural, and microstructural properties of Ge-doped CZTSe solar cells have been accessed by conducting a combinatorial approach of electron- and advanced synchrotron-based methods at the nanoscale. Three different solar cells with varying nominal compositions and different level of performance were prepared by IREC using a sequential process, which includes the deposition of an ultra thin Ge layer on top of Mo and the precursor stack. In total 9 cross-sectional lamellae, 3 for each composition, were prepared at different positions out of complete devices using a FIB system.

STEM images revealed the morphology and the layered geometry of the solar cells. The polycrystalline absorbers consists of large grains, but also exhibits detrimental voids at the back contact, which were observed for all cross-sections. The chemical composition was identified by EDS. The outstanding homogeneous distribution of the main absorber elements (Cu, Zn, Sn and Se) is independent of the stoichiometry and particularly remarkable since no Cu, Zn and Sn related secondary phases were observed at all. Compositional analysis of the average absorber composition coincided with the intended Cu-poor and Zn-rich nominal composition. Slight lateral variations between different regions on the absorber, which exceeded the experimental uncertainty, were found for the Zn/Sn ratio, while the Cu/(Zn+Sn) distribution was in agreement with the reference. The off-stoichiometry types associated with the composition can therefore mainly be assigned to the A-type, which is responsible for the intrinsic p-type doping. However, the slight Zn/Sn disorder also leads to a mixture of the A-type with either B or L off-stoichiometry types for specific domains and for S3 some might consist also of a mixture or only J-type. These local variations imply the formation of different harmful intrinsic point defects and should be avoided. Complementary nano-XRF measurements reveal an even more homogeneous Cu/(Zn+Sn) distribution than expected from EDS, and corroborate the fluctuation of Zn and Sn. With respect to the different nominal compositions, the varying conversion efficiencies cannot be explained by strong compositional fluctuations or by secondary phase segregations and are probably related to the different intrinsic doping levels and the formation of detrimental defect complexes for S3. Moreover, the nano-XRF measurements allow to observe subtle compositional changes in selected regions of the front- and back contact interfaces. In particular, a slightly reduced Cu and increased Zn content at the CdS/CZTSe interface and vice versa at the back contact can also strongly influence carrier recombination. The combination of the outstanding homogeneity of the absorber and the variations at the interfaces indicate that the main limitations are likely the interfaces and not the bulk absorber.

By exploiting the high sensitivity of the hard X-ray nanobeam Ge was found to remain in the absorber after the solar cell synthesis. The heterogeneous Ge incorporation was found to be independent on the stoichiometry and was compared to the results of different electron microscopy techniques, whereby the correlation with the presence of different grains, selected grain boundaries, and nanoscale inclusions was revealed. The Ge concentration varied between different grains from 0.1 to 0.5 at.%. Only a negligible impact on the improved V_{OC} is expected by this substitution, because the band gap is not significantly widened by such small quantities of Ge and the number of exchanged atoms is quite small. Increased Ge concentrations were found for the inclusions and a minimum concentration of at least 20 at.% was estimated. Two types of grain boundaries were observed via EBSD in the absorber, the highly symmetrical $\Sigma3$

twins and random ones. Whereas the former are inconspicuous, random boundaries are Ge depleted. The absent leads to an attractive force for electrons and probably to an increased carrier recombination. The short-range structural order of Ge was obtained from nano-XANES measurements. Within the absorber Ge is located on substitutional lattice sites and incorporated into the kesterite matrix. On the other hand, the nanoscale inclusions most likely consist of GeO_2, which presumably limit the efficiency because of the higher band gap and the interface area, where electrons might recombine.

6. Interplay of performance-limiting nanoscale features in $Cu_2ZnSn(S,Se)_4$ solar cells

This chapter reports on the formation of secondary phases, local compositional variations and microstructural properties of CZTSSe kesterite absorbers, which were produced with different nominal Cu-poor and Zn-rich compositions. The absorbers and complete solar cells were fabricated and electrically characterized by Dr. Gerardo Larramona (IMRA Europe). The electrical data were evaluated in collaboration with Dr. Udo Reislöhner. The cross-sectional lamellae were prepared by Dr. Sven Schönherr. SEM and STEM images were taken in cooperation with Dr. Sven Schönherr and Oliver Rüger. Nano-XRF measurements were performed in collaboration with Dr. Sven Schönherr, as well as Konrad Ritter, Prof. Claudia S. Schnohr (Universität Leipzig), Dr. Andreas Johannes, Dr. Damien Salomon (European Synchrotron Radiation Facility, ESRF), and Dr. Gema Martínez-Criado (Instituto de Ciencia de Materiales de Madrid, CSIC). The CZTSe reference sample was synthesized by Dr. Galina Gurieva and provided by Prof. Susan Schorr (Helmholtz-Zentrum Berlin für Materialien und Energie, HZB). Parts of this chapter are published in reference [67].

6.1. Motivation

The incorporation of sulfur during the growth of thin film kesterite solar cells gives control over the direct, tunable band gap in terms of tailoring the absorption properties of the absorber layer [167]. This approach led to record conversion efficiency of 12.6 % [29] for CZTSSe solar cells using a toxic hydrazine-based processing approach. The main limitation in such devices is still the high V_{OC} deficit compared to the optical band gap. Cu-poor and Zn-rich synthesis conditions [29, 175] are generally preferred for high efficiency cells to control the intrinsic p-type doping by Cu vacancies [32, 177–179]. However, such conditions also facilitate the formation of binary secondary phases [35, 180, 181, 291] harming the device performance [188, 189]. Moreover, the presence of phases apart from kesterite usually introduces a discrepancy between the intended and realized CZTSSe composition [36, 181], which significantly influences

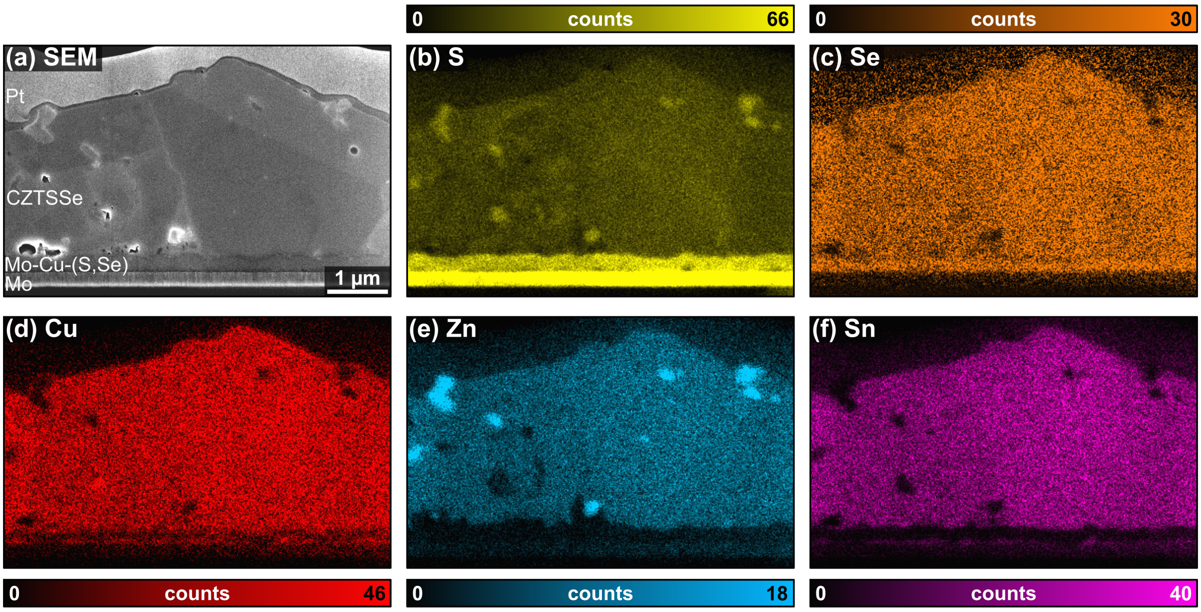

Figure 6.1.: SEM image (a) and EDS intensity maps for the five absorber elements (b-f) of the CZTSSe absorber with the nominal composition C1. The intensity maps were obtained by integrating the counts for each pixel in an energy interval (table A.1, appendix) for the individual elements. The alleged S signal in the Mo layer actually originates from Mo L_α lines, which strongly overlap with the S K_α lines. The average thickness of this lamella was approximately 170 nm.

the electronic properties by the formation of different defects and defect clusters [32]. To overcome these limitations, it is of great importance to gain a more comprehensive understanding about the local kesterite composition, but also about the nature, quantity, size, and spatial distribution of the secondary phases. To that end, highly efficient CZTSSe absorbers with different nominal compositions were produced by a non-toxic spray coating process in order to study morphological, spatially resolved compositional and microstructural characteristics of the absorbers. For details about the solar cell synthesis see section 3.1.3.

6.2. Detecting secondary phases, the spatially resolved composition and various off-stoichiometry types

The SEM image in figure 6.1a shows the cross-sectional lamella prepared out of the CZTSSe absorber C1, with nominal Cu/(Zn+Sn), Zn/Sn, and Se/(S+Se) ratios of 0.83, 1.10, and 0.65, respectively. In the micrograph, the layered geometry of the sample can be clearly identified, while on top of the absorber the protective Pt layer is located. Small voids within the absorber and close to the back contact are formed during the growth (for details see section 5.2), which are not expected to be detrimental as their size is below roughly 200 nm [244]. Within the absorber several interesting contrast variations can be recognized. EDS measurements were performed in order to evaluate the origin of these variations. Details about the measurements can be found in section 3.3.4 and 4.2.

Figure 6.1b-f show the EDS intensity maps of the matrix elements, which display similar layers like the SEM image. A pronounced signal at the bottom of the S map in figure 6.1 seems to correlate with the Mo layer in the SEM image. However, this alleged signal originates from the strong overlap of the Mo L_α-lines and S K-lines (see figure 5.3). An irregular, roughly 250 nm thick Mo-Cu-(S,Se) interface layer was formed between Mo and CZTSSe. The diffusion of Cu into the Mo(S,Se) layer during the lamella preparation has been reported in previous studies [292, 293]. However, here, the estimated Cu concentration of 14 at.% rather indicates the formation of a Mo-Cu-(S,Se) compound during the absorber synthesis. In addition, the lamellae prepared out of CZTSe:Ge solar cells in section 5.3 were prepared by the same the same FIB-based process and revealed no Cu in the $MoSe_2$ layer.

The absorber layer can be localized by comparing the SEM image and the intensity maps. The most striking characteristics are small spots with sizes between 200 - 650 nm in size with a different composition than CZTSSe. Comparing the different maps, it becomes evident that the spots are Zn- and S-rich. Furthermore, the remaining absorber elements are absent or strongly reduced clearly indicating the formation of secondary phase segregations. Two possible phases might be formed: ZnS(Se) or Zn(Cu,Sn)S(Se). Note, EDS only provides information about the local composition and not a structural analysis. However, X-ray diffraction data taken on similar produced CZTSSe solar cells only detected ZnS(Se) secondary phases [294]. The formation of ZnS(Se) was also observed by XANES measurements on CZTS thin films prepared by co-evaporation [35]. ZnS(Se) was also found by TEM-EDS investigations on CZTSSe thin films prepared by a non-toxic solvent-based process [295]. Thus, the formation of ZnS(Se) can be expected. In the present case the signal of Cu and Zn in the regions where secondary phases occur is not contradictory. Small amounts of kesterite behind or in front of the secondary phase can contribute to the signal when averaging over the whole lamella thickness along the beam direction. The number and size of the secondary phases tend to be larger close to or at the absorber surface in the examined area. Nevertheless, several segregations can also be identified within the absorber and near the back contact. ZnS and ZnSe secondary phases are believed to be the least detrimental due to their semiconducting nature combined with wide band gaps of 3.91 eV [296, 297] and 2.69 eV [298], respectively. The large band offset between CZTSSe and ZnS(Se) indicates that these secondary phases act as a resistive barrier for

Table 6.1.: Atomic concentrations and cation ratios of the CZTSe reference and the three investigated absorbers with composition C1-C3 determined by EDS. The values display the mean value and standard deviation of 20 selected areas that were evenly distributed on the absorber and did not contain secondary phases. For sample C1-C3 only the cation concentrations and cation ratios were calibrated using the CZTSe reference sample, while the anions were not calibrated. The nominal composition was estimated from the initial colloid content.

sample	Cu (at.%)	Zn (at.%)	Sn (at.%)	S (at.%)	Se (at.%)	Cu/(Zn+Sn)	Zn/Sn
CZTSe	25.0 ± 0 .4	12.5 ± 0.3	12.5 ± 0.2		50.0 ± 0.4	1.00 ± 0.03	1.00 ± 0.03
C1	22.5 ± 0.7	12.5 ± 0.5	11.9 ± 0.7	21.5 ± 2.2	28.0 ± 1.7	0.92 ± 0.04	1.05 ± 0.08
nominal	22.7	14.3	13.0	17.5	32.5	0.83	1.10
C2	21.8 ± 0.8	13.3 ± 0.8	12.5 ± 0.5	20.5 ± 2.0	28.4 ± 1.4	0.85 ± 0.05	1.07 ± 0.08
nominal	21.8	15.7	12.5	17.5	32.5	0.77	1.25
C3	24.4 ± 0.7	12.3 ± 0.4	12.3 ± 0.5	20.4 ± 2.7	27.3 ± 2.5	1.00 ± 0.04	1.03 ± 0.07
nominal	24.3	13.1	12.7	17.5	32.5	0.94	1.04

electrons [299, 300]. Since the minority charge carrier diffusion length surpasses 500 nm [244] and therefore the width of the secondary phases, a critical effect to the electrical transport properties is not expected. Nevertheless, a detrimental impact cannot be ruled out, since Just et al. reported on a reduced current density, fill factor and open circuit voltage and therefore adverse effects on the electronic properties caused by ZnS inclusions [296].

In figure 6.1d-f, the cation distributions in the absorber seem to be fairly homogeneous apart from the secondary phases. In contrast, lateral variations of the anion distribution can be observed in excellent agreement with previous studies [301, 302]. 20 areas with a dimension of $200 \times 200\,\mathrm{nm}^2$ were defined on the absorber, which contain no secondary phase segregations, in order to investigate this lateral heterogeneous distribution in even more detail. The concentrations were determined by fitting the respective spectra with the software package AZtec®. Only the atomic concentrations of the cations were calibrated with the factors listed in table 4.1 as the reference did not contain S. Table 6.1 lists the mean values and standard deviations of the 20 spots for the CZTSe reference and all absorbers investigated. The observed fluctuations for C1 clearly exceed those of the CZTSe reference, which indicates real variations of the local CZTSSe composition. Especially, the anion distribution reveals distinct fluctuations in excellent agreement to the observed variations in the intensity maps in figure 6.1b and c and to the previous reports [301, 302]. Varying amounts of S and Se tune the band gap from 1.0 eV for pure selenides to 1.5 eV for pure sulfides [167]. Thus, a graded S,Se profile over the depth of the absorber can be used to reduce the conduction band minimum towards the front contact. Such a band bending results in a beneficial attractive force for the electrons towards the front contact. In the present case, the observed anion fluctuations show a random distribution, which probably reduces the effective band gap and therefore the V_{OC}. Thus, the synthesis parameters should be adjusted to avoid the inhomogeneity or to apply a depth gradient.

Figure 6.2 plots Zn/Sn as a function of the Cu/(Zn+Sn) ratio for the randomly chosen 20 calibrated spots (orange circles), for a more precise investigation of the heterogeneous cation distribution. Their mean value is given by the red circle with its standard deviation and the nominal growth composition by a black star. The dark gray area corresponds to one standard deviation and the light gray area to two standard deviations obtained from the measurement of the stoichiometric CZTSe reference in section 4.2. As a visual guide, figure 6.2a illustrates the data taken on the stoichiometric CZTSe reference. As introduced in section 5.3 real fluctuations of the local absorber composition are present when the variation of the 20 individual data points exceeds the experimental uncertainty of the CZTSe reference.

Figure 6.2b depicts the calibrated cation ratio plot for sample C1. The average sample composition reveals Cu-poor and Zn-rich conditions, although the absorber is less Cu-poor and less Zn-rich compared to the nominal composition. Even considering the experimental uncertainty - one or two standard deviations - a significant discrepancy between nominal and probed quantity can be detected. Just et al. [35] reported for sulfide- and selenide-based kesterite absorbers on a constrained Zn/Sn ratio of 1 for Cu-poor and Zn-rich conditions and that excess Zn will always segregate in secondary phases. However, these absorbers were prepared by non-vacuum solution processing for the selenides and co-evaporation for the sulfides [35]. In fact, ZnS(Se) secondary phases were also found in these cells, explaining the difference between nominal and measured composition. However, the absorber still remains Cu-poor and Zn-rich, which proves the possibility to grow off-stoichiometric CZTSSe by this spray coating technique. It suggests that the achievable range of off-stoichiometry is different for diverse synthesis routes. Indeed, the possibility to grow off-stoichiometric CZTS and CZTSe was already demonstrated, but only for powder samples prepared by time and energy consuming solid state reaction [181, 184, 187].

The fluctuations of the 20 spots clearly surpasses that of the stoichiometric reference sample in figure 6.2a. For the Cu/(Zn+Sn) ratio the standard deviation is significantly increased, whereas for the Zn/Sn ratio the deviation is more than twice as high as the reference (see also table 6.1). This unambiguously proves the presence of real spatial fluctuations of the local absorber composition. As already introduced in section 5.3, varying compositions are inherently connected to different off-stoichiometry types

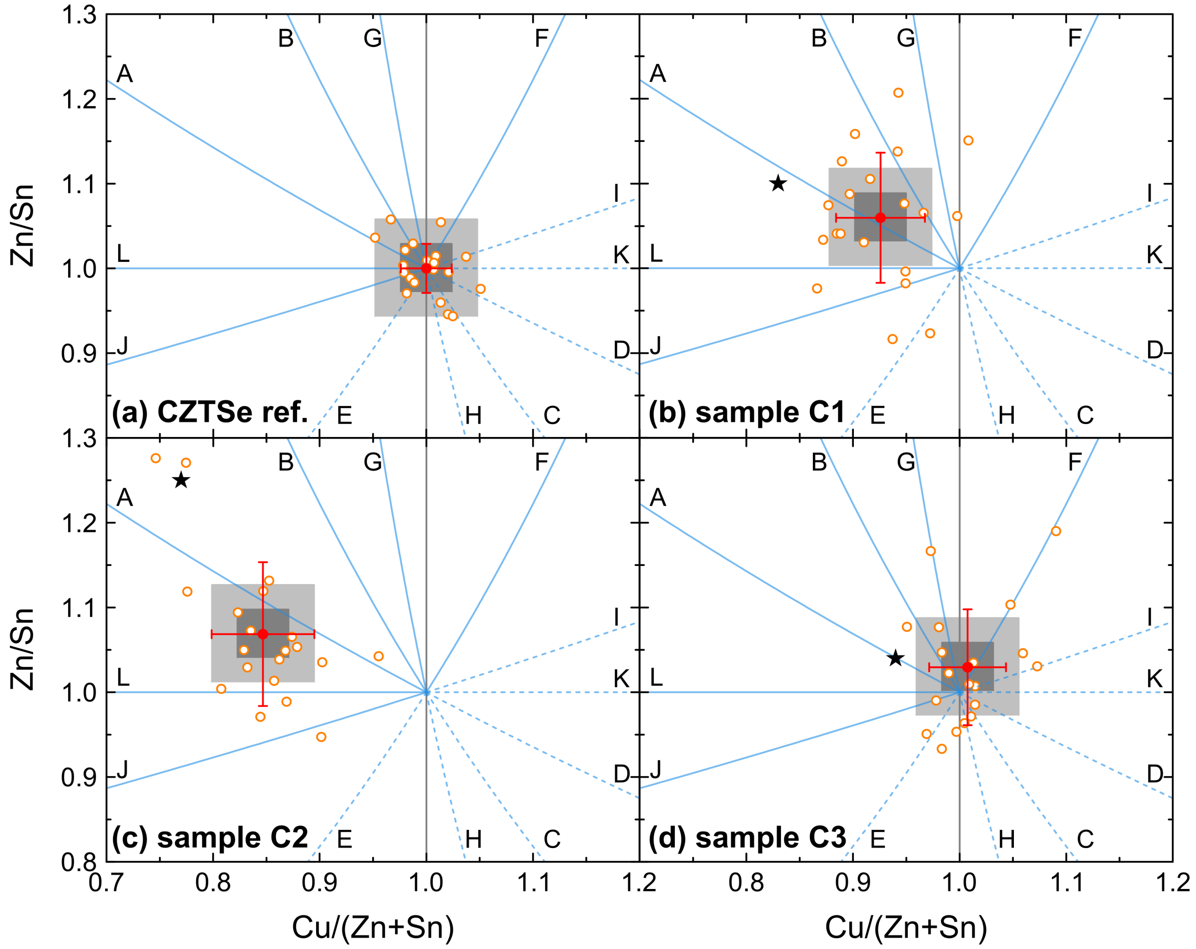

Figure 6.2.: Calibrated cation ratio plots of the CZTSe reference (a) and the three investigated solar cells (C1-C3) with different nominal composition (c-d). The orange circles illustrate the composition of the 20 individual spots, while the red circle marks their average with the corresponding standard deviation as error bars. The black star illustrates the nominal composition. The dark and light gray areas represent one and two times the standard deviation, evaluated from the reference and plotted with respect to the average composition for the different absorbers. The solid and dashed blue lines show all off-stoichiometry types (A-L) of kesterite. (The off-stoichiometry types are adapted from [36, 184, 186, 187].)

named A-L [36, 184, 186, 187]. To classify the absorber, these types are highlighted by solid and dotted blue lines in figure 6.2. The measured absorber composition of sample C1 coincides with the A off-stoichiometry type as intended by the nominal composition. The related point defects are Cu vacancies V_{Cu} and Zn_{Cu} anti-sites [186], which form a shallow acceptor and donor level, and are responsible for p-type doping [32]. In case of the 20 individual spots, considering the experimental accuracy, a broad range of off-stoichiometry types are discernible including A, B, E, F, G, J, and L types. Only the A-type feature the favorable defects and lead to the beneficial p-type conductivity. The remaining off-stoichiometry types feature Zn_{Sn}, Cu_{Sn}, Zn_{Cu}, and Sn_{Cu} anti-sites, V_{Cu} and V_{Zn} vacancies, and Zn_i and Cu_i interstitials [36, 184, 187]. Several of these defects form deep donor and acceptor states [32] that could act as electron recombination

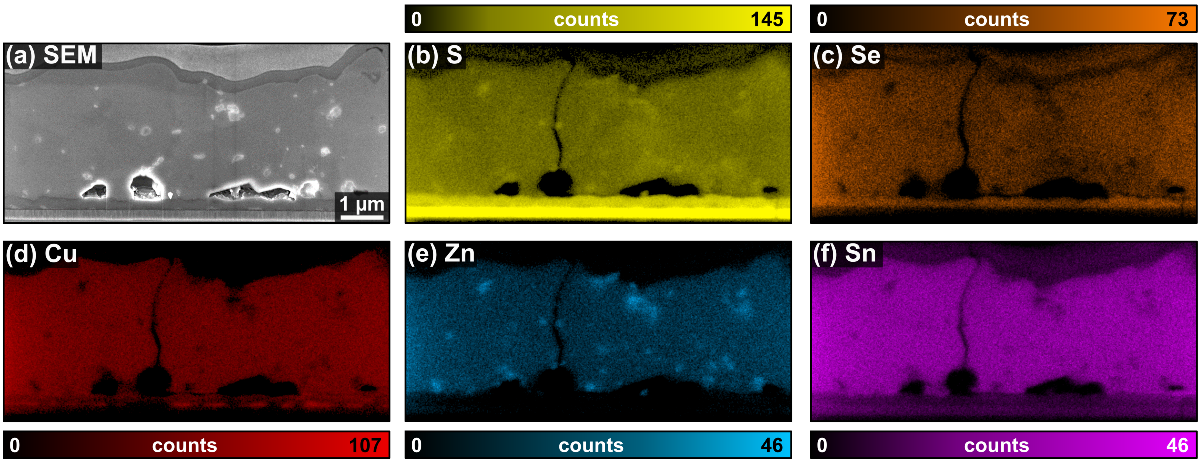

Figure 6.3.: SEM image (a) and EDS intensity maps for the five absorber elements (b-f) of the CZTSSe absorber with the nominal composition C2. The lamella broke after the nano-XRF measurements, causing a vertical artifact only in the EDS maps. The average thickness of this lamella was approximately 340 nm.

centers and reduce the conversion efficiency. Moreover, some spots are Zn-poor and one also Cu-rich, which likely increase the number of detrimental ($2\mathrm{Cu}_{\mathrm{Zn}}^{-}$ + $\mathrm{Sn}_{\mathrm{Zn}}^{2+}$) defect complexes [32].

Two more solar cells were grown under the same synthesis condition: one (C2) with an even Cu-poorer, Zn-richer composition and another (C3) close to the CZTSSe stoichiometry (table 6.1). The nominal Se/(S+Se) ratio of 0.65 remained the same for all three samples. Subsequently, lamellae were prepared and examined with the same measurement and analysis technique to gain detailed insights in the elemental distribution.

The calibrated cation ratio plot of absorber C2 is depicted in figure 6.2c. The average composition reveals a less Cu-poor and less Zn-rich absorber compared to the nominal composition, but remains Cu-poor and Zn-rich (compare table 6.1). The difference between nominal and measured quantity is very similar to C1, in relation to the Cu/(Zn+Sn) ratio, but clearly exceeds it for the Zn/Sn ratio. This can be explained by the formation of even more and larger ZnS(Se) secondary phases with sizes of more than 1 µm (see figure 6.3). The off-stoichiometry type derived from the averaged composition does not agree with the intended mixture of A- and B-type and indicates a mixture of A and L. Locally, most of the 20 spots can be classified as A- and L-type or as a mixture of both. Thus, beneficial Cu vacancies V_{Cu} of the A-type vacancies compete against harmful $\mathrm{Sn}_{\mathrm{Cu}}$ anti-sites of the L-type [187], which form detrimental donor states in the band gap [32]. Finally, one spot is almost in agreement with the J-type, but might also have a contribution of the E-type. The related $\mathrm{Sn}_{\mathrm{Cu}}$, $\mathrm{Zn}_{\mathrm{Sn}}$ anti-sites, and V_{Zn} vacancies form detrimental states in the band gap and likely increase the carrier

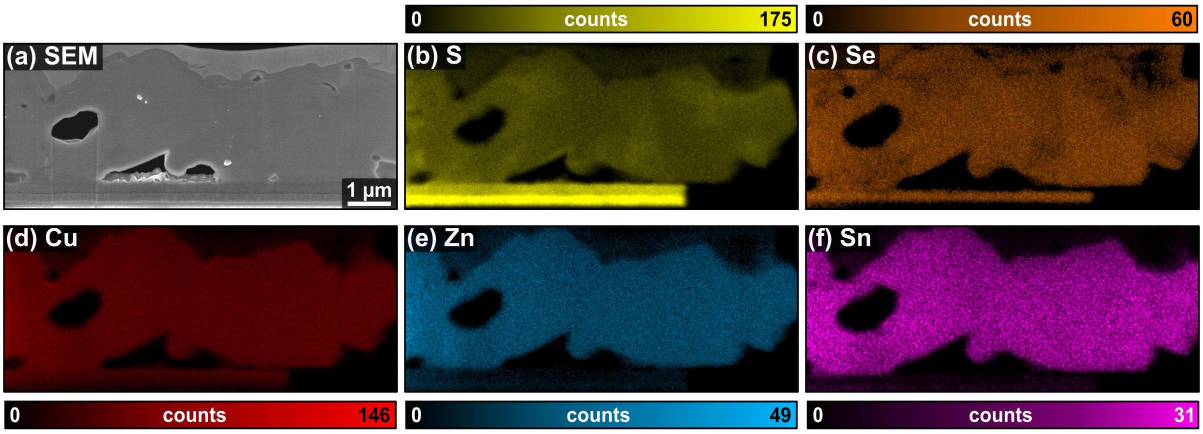

Figure 6.4.: SEM image (a) and EDS intensity maps for the five absorber elements (b-f) of the CZTSSe absorber with the nominal composition C3. A segment of the lamella (bottom right corner) broke after the nano-XRF measurement and is therefore not visible in the EDS image. The average thickness of this lamella was approximately 280 nm.

recombination probability [32, 184, 187]. In addition, the Zn-poor L-type condition might facilitates the formation of harmful ($2Cu_{Zn}^{-}$ + Sn_{Zn}^{2+}) defect complexes [32]. The evaluated composition of C3 shows the smallest deviation between nominal and evaluated average values. The latter almost coincides with the stoichiometry in conformity with the absence of ZnS(Se) secondary phase segregations for this composition, as shown in figure 6.4. Consequently, they only form when the Zn/Sn ratio exceeds a critical value and/or the Cu concentration falls below a critical amount. These findings are in excellent agreement with Just et al. who proposed a critical value of approximately 1.09 for the Zn/Sn ratio [35]. On average, the CZTSSe composition is close to stoichiometry, thus no off-stoichiometry type would be assigned. On the other hand, the standard deviations especially for the Zn/Sn ratio are significantly increased. Accordingly, real spatial variations in the local kesterite composition can be observed associated with B, E and G off-stoichiometry types for the Cu-poor domains, and F- and I-type for the Cu-rich ones. Thus, the related point defects are Zn_{Sn}, Cu_{Sn} anti-sites, Cu_i, Zn_i interstitials, in addition to the already mentioned defects for the Cu-poor off-stoichiometry types [184, 187]. Overall, several of these defects form deep donor and acceptor levels where electrons can recombine [32]. Furthermore, an exponential increase of ($2Cu_{Zn}^{-}$ + Sn_{Zn}^{2+}) defect complexes can be expected due to the Cu-rich and/or Zn-poor spots, which presumably reduce the effective band gap and therefore the V_{OC} [32].

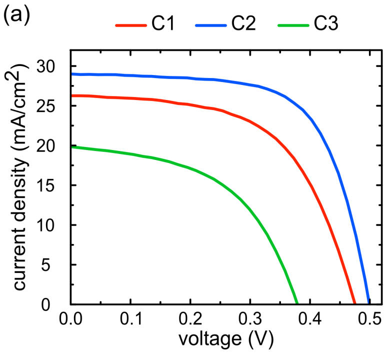

(b)

sample	C1	C2	C3
η (%)	7.15	9.5	3.8
J_{SC} (mA/cm^2)	26.2	29.0	19.8
V_{OC} (mV)	475	499	379
FF (%)	57.3	65.6	50.8
R_{shunt} (Ωcm^2)	330	798	134
R_{series} (mΩcm^2)	1297	407	834

Figure 6.5.: Illuminated JV curves of the samples with nominal composition C1-C3 (a) and selected electrical device parameter (b).

6.3. Correlation of the absorber properties with the conversion efficiency

In the previous section secondary phases and multiple collateral point defects were observed in dependence on the intended nominal composition. It is therefore of particular interest to correlate these findings with electrical device parameters. Absorbers, produced in the same run and with the same nominal composition were processed to completed solar cells and electrically characterized. For details see section 3.1.3.

Figure 6.5 shows the illuminated JV curves and selected electrical parameters of the most efficient cells for all three compositions. The solar cell with composition C2 shows the highest conversion efficiency despite the formation of many and large resistive secondary phases as well as mixture of A and L off-stoichiometry types. This demonstrates that at the current performance level ZnS(Se) phase segregations are not necessarily the main limitation in CZTSSe devices, even when they are located at the interface of the absorber, as indicated by the lowest series resistance. Moreover, the highest amount of Cu vacancies V_{Cu} and the least variation of the off-stoichiometry type lead to the lowest V_{OC} deficit and highest J_{SC}. The device with composition C1 owns a lower efficiency, which might be a consequence of a higher amount of different off-stoichiometry types and a higher series resistance caused by a lower doping level. Despite the absence of secondary phases, C3 yields the lowest conversion efficiency. The reason is likely the formation of Cu-rich and/or Zn-poor kesterite, which features detrimental deep defects acting as electron recombination centers. Furthermore, the significantly lower V_{OC} can presumably be explained by the formation of $(2Cu^-_{Zn} + Sn^{2+}_{Zn})$ defect complexes, which reduce the effective band gap.

These findings clearly demonstrate the importance of Cu-poor and Zn-rich conditions leading to less harmful defects and to overall higher conversion efficiencies. Thus, the suppression of ZnS(Se) secondary phase segregations in combination with an improved CZTSSe homogeneity might further enhance the conversion efficiency.

6.4. Imaging of nanoscale compositional fluctuations and variations at grain boundaries

Section 6.2 discussed the formation of secondary phases and revealed a heterogeneous elemental distribution leading to multiple off-stoichiometry types. To examine these variations on an even smaller scale, synchrotron-based nano-XRF measurements were conducted on the same lamellae shown in section 6.2. The strength of this technique is the improved elemental sensitivity at higher energies but also the excellent detection limits. This allows the determination of much lower compositional variations at nanometer scale as already shown in section 5.5.4. The only disadvantage is that the experiments were conducted under ambient conditions. This causes a significant low-Z absorption by air and the detectors Be window, which precludes the detection of S.

Figure 6.6a shows the SEM micrograph of the same lamella of sample C1 as shown in figure 6.1, but from a slightly different area. The respective nano-XRF maps, shown in figure 6.6b-f, validate the formation of the Mo-Cu-(S,Se) interface layer between the Mo and CZTSSe layer. Within the absorber similar characteristics can be observed as in the EDS measurements but even more and smaller details become apparent. Zinc hotspots accompanied by the depletion of the remaining cations corroborate the coexistence of CZTSSe and ZnS(Se) secondary phases in the absorber. Especially the size and appearance of the secondary phases are much better defined in these intensity maps than in the EDS intensity maps in figure 6.1. Furthermore, strong spatial fluctuations in the Se map can be observed and confirm the formation of local band gap fluctuations.

The acquired fluorescence radiation was influenced by attenuation of the lamellae ridges and the Ni grid (for details see section 3.2.1). Thus, relative maps of the cation ratios were calculated in the orange marked area in figure 6.6 in an analogous manner as presented in sections 4.3 and 5.5.1. Figure 6.7 illustrates the relative cation ratio maps for sample C1-C3 and for the CZTSe reference. Note, the colorbar was adjusted to -0.2 to 0.2 compared to -0.1 to 0.1 for figure 4.3 and 5.10. All areas without absorber are light gray overdrawn.

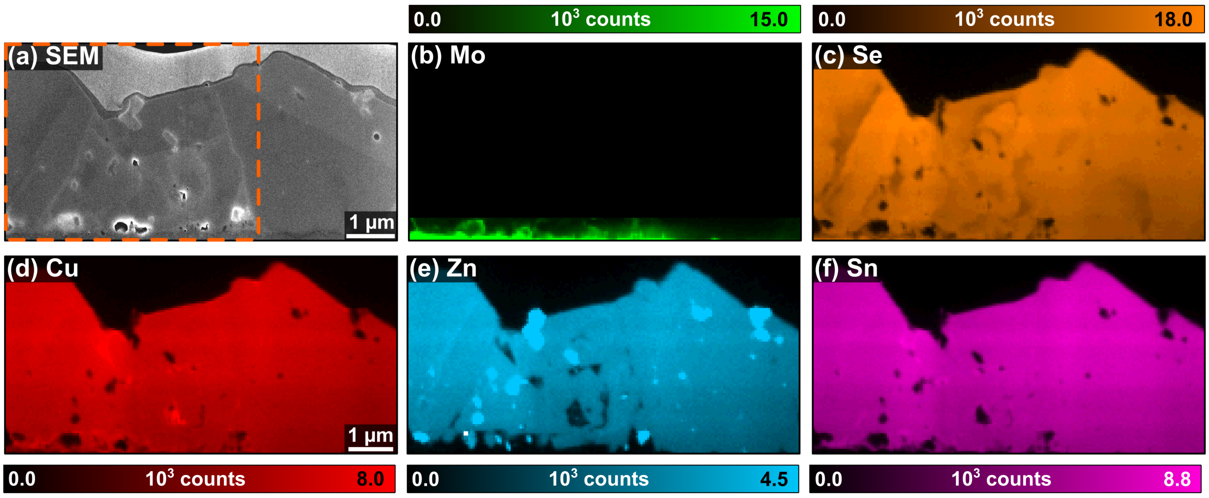

Figure 6.6.: SEM image and fitted nano-XRF intensity maps of the Mo back contact (b) and the four absorber elements (c-f) of the same lamella C1 shown in figure 6.1, but of a slightly different area. The intensity maps show the integrated counts of each element for each pixel, obtained by fitting the corresponding spectrum with the software PyMCA [211]. A slightly increased Mo signal within the voids is an artifact from the lamella preparation. The orange rectangle mark the region which is suited to calculate the relative maps in figure 6.7. The average thickness of this lamella was approximately 170 nm.

In certain areas of figures 6.7c and d a clear anti-correlation pattern, i.e., an increase of the Zn/Sn ratio and a Cu/(Zn+Sn) ratio that is significantly decreased, confirms the formation ZnS(Se) secondary phase segregations. The size of the secondary phases severely fluctuate and decreases down to the resolution limit of the synchrotron nanobeam (figure 6.7c and d black circles). The most striking new characteristic is the contrast variation between the left and right side in figure 6.7d, which could not be observed in the intensity maps in figure 6.6 and is also not present in the Δ(Cu/(Zn+Sn)) ratio map in figure 6.7c. In this particular case, the findings verify the presence of real spatial fluctuations of the local CZTSSe composition and off-stoichiometry types deduced from the EDS measurements. Moreover, the variations mainly concern the Zn-Sn disorder, as indicated by the higher standard deviation of the Zn/Sn ratio compared to the Cu/(Zn+Sn) ratio in table 6.1 and figure 6.2. On the other hand, the purple circles in the subtraction maps reveal domains with an increased Cu and a decreased Zn concentration, while the Sn content is unchanged or slightly increased (see also figure A.7 in the appendix). An interface layer featuring similar less Cu-poor and less Zn-rich conditions can be observed on top of the Mo-Cu-(S,Se) layer. A detailed analysis of the layer and of the domains reveal variations exceeding 0.05 for both cation ratios, and excludes an explanation based on the experimental uncertainty. As a consequence, a lateral, non-uniform p-type conductivity caused by a reduced number of V_{Cu} vacancies prevails in the absorber. However, the effect of the Cu-enriched layer close to the back

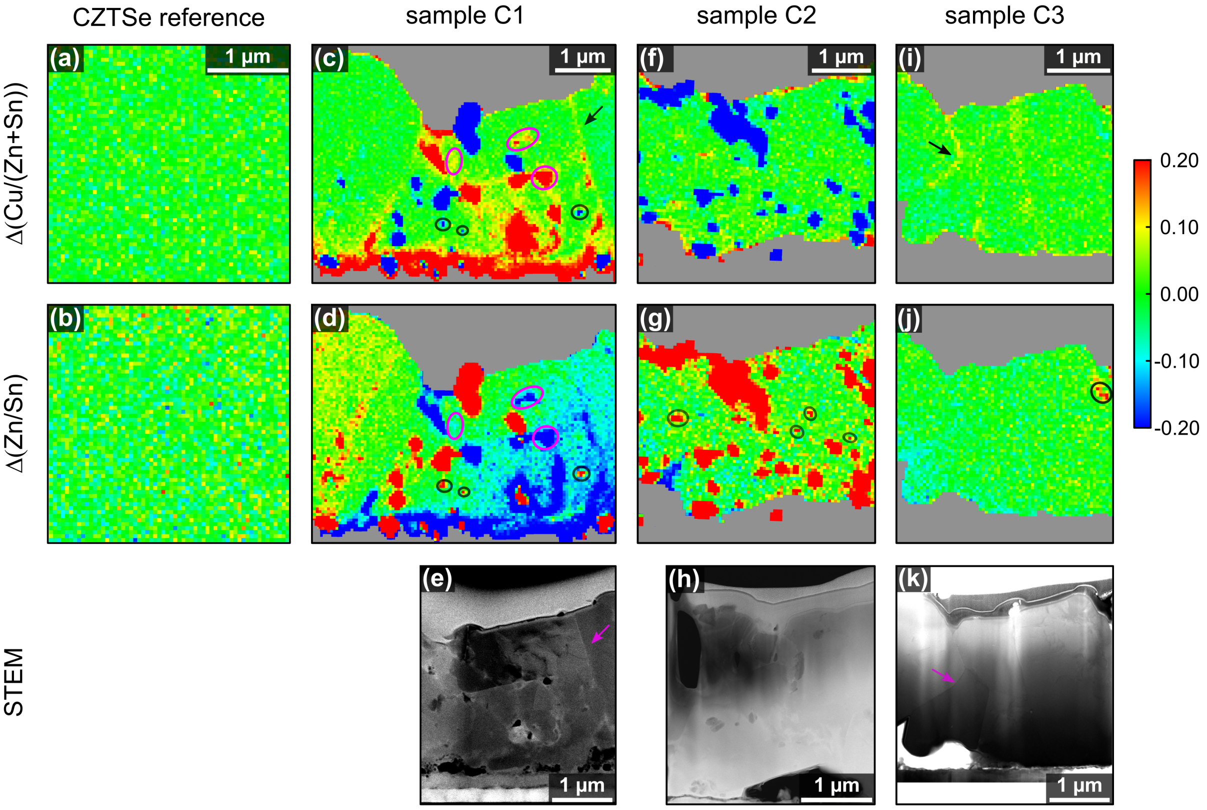

Figure 6.7.: Deviation of the cation ratio from the respective mean value for the Cu/(Zn+Sn) and Zn/Sn ratio. These maps were calculated by subtracting the mean value of a particular map from the actual value of every individual pixel for the CZTSe reference and the three different compositions C1-C3. The black circles highlight nanoscale secondary phases, while the purple ones mark less Cu-poor domains. The black circle in (j) points a Zn-enriched domain out. Gray areas mark the regions where no CZTSSe absorber was present, such as the Mo back contact, the Mo-Cu-(S,Se) layer, voids, Pt, and air. The color bar is the same for all maps. HAADF- (e,h) and BF-STEM (k) images reveal the grain boundaries of the absorbers. Prior to the STEM measurements, the lamellae of C2 and C3 were thinned down to enhance the contrast, which explains the hole in the upper left corner in (h) and the partly missing Pt layer in (k).

contact on the performance is likely not very detrimental, because the width of the space-charge region ($\sim 200\,\text{nm}$ [303]) plus the diffusion length ($< 900\,\text{nm}$ [244]) is smaller than the distance from the absorber surface to the less Cu-poor layer.

Indeed, a similar evaluation is also possible for the EDS measurements, but as shown in section 4.2, only with a spatial resolution of $200 \times 200\,\text{nm}^2$ to keep the related low standard deviation. Such a spatial resolution averages small deviations out and the access to the here investigated fluctuations is not possible. A detailed comparison that highlights the new features compared to the EDS maps can also be found in figure A.6 (appendix).

Figure 6.7e shows a section of the STEM-HAADF image revealing the grain boundaries of the polycrystalline absorber. The comparison with with the ratio maps in figure 6.7c and d reveals that selected grain boundaries exhibit a less Cu-poor and less Zn-rich composition, while Sn shows no obvious trend (see also figure A.7 in the appendix).

In fact, the beam dimension of roughly 50 nm is much bigger than chemical variations at grain boundaries (1 nm [38, 40, 304]), thus the actual Cu concentration can be expected to be much higher at the boundary. Previous studies observed similar Cu-enriched grain boundaries and their likely detrimental effects for pure selenide and sulfide absorbers by TEM-EDS [268, 293] and by atom probe tomography [40]. The Cu enrichment likely reduces the amount of Cu vacancies V_{Cu} and might even promote the formation of detrimental Cu_{Zn} anti-site defects, thus enhancing the carrier recombination [305, 306]. In contrast, literature also observed Zn- [40] and Sn-enriched [269] grain boundaries, which were not observed in this absorber.

Figure 6.7f and g show the deviation maps for absorber C2 (for intensity maps see figure A.8 in the appendix). The same secondary phase segregations as observed for EDS can be identified and even smaller features become present as highlighted by black circles. In contrast to C1, no less Cu-poor interface layer is formed at the back contact. Moreover, the grain boundaries reveal no compositional variations and no compositional gradient can be observed as well. For C3 no secondary phases or the formation of a interface layer on top of the Mo-Cu-(S,Se) layer can be identified in figure 6.7i and j, which is in excellent agreement to the EDS results in figure 6.4 (for intensity maps see figure A.9 in the appendix). The only exception is observed in the upper right area of the absorber marked by a black circle. Here the Zn/Sn ratio increases by roughly 0.12 compared to the surrounding, which points to a variation in the local CZTSSe stoichiometry rather than a ZnS(Se) secondary phase. Nevertheless, the formation of a secondary phase can no be completely ruled out. Finally, the STEM image in figure 6.7k reveals the grain boundaries. Selected grain boundaries exhibit an increased Cu accumulation accompanied by a slightly decreased Zn concentration and an unchanged Sn content (see black arrow and figure A.7 in the appendix).

6.5. Compositional variations for six different lamellae

The evaluated areas show only a very small section of the solar cells. Thus, two lamellae, called I and II, were prepared from different positions on the sample and characterized by nano-XRF. Table 6.2 summarizes the results addressing the formation of secondary phase segregations, compositional fluctuations of the CZTSSe absorber, compositional variations at grain boundaries, and elemental changes close to and at the back contact.

For the Cu-poor and Zn-rich absorbers C1 and C2 ZnS(Se) secondary phases were observed in both lamellae and none were found for composition C3 close to stoichiom-

Table 6.2.: Summary of the observed compositional variations for the six investigated lamellae with the three different compositions C1, C2, and C3.

composition	C2		C1		C3	
nominal Cu/(Zn+Sn)	0.77		0.83		0.94	
nominal Zn/Sn	1.25		1.10		1.04	
lamella	I	II	I	II	I	II
secondary phase segregations						
ZnS(Se)	✓	✓	✓	✓	X	X
elemental Cu	X	X	X	✓	X	X
CZTSSe compositional fluctuations						
less Cu poor, Zn rich domains	✓	✓	✓	✓	X	X
horizontal gradients	X	X	✓	X	X	X
grain boundaries						
Cu increased, Zn reduced, Sn unchanged	X	X	✓	✓	✓	✓
back contact						
less Cu poor, Zn rich region	X	X	✓	✓	X	X
Mo-Cu-(S,Se) interface layer	✓	✓	✓	✓	✓	✓

etry. High numbers of small secondary phases have been found in the absorbers closer to the back contact, while a few large ones accumulate at the surface. By decreasing the nominal Cu/(Zn+Sn) and increasing nominal Zn/Sn ratio the number and size of the ZnS(Se) increases as well. The most surprising observation is the formation of elemental Cu at the back contact observed only for lamella C1-II. The CZTSSe homogeneity strongly depends on the nominal composition and on the position within the absorber. Here, lamella C1-I reveals a gradient in vertical direction. The inhomogeneity is also apparent at selected grain boundaries. Some tend to be less Cu-poor, less Zn-rich, whereas the Sn content is mostly unchanged, but only for lamellae with composition C1 and C3. Close to the back contact a less Cu-poor, less Zn-rich layer like region formed, but only for the intermediate composition C1. Finally, all lamellae possessed the Mo-Cu-(S,Se) interface layer between the CZTSSe absorber and the Mo back contact.

6.6. Summary

In this chapter a combination of electron and X-ray microscopy techniques at the nanoscale gave access to the spatially resolved composition and microstructure of CZTSSe solar cell absorbers. The absorbers were grown by IMRA Europe using a hydrazine free spray coating technique followed by a 2-step annealing process. In total 3 absorbers with different nominal compositions and level of performance were fabricated and 6 cross-sectional lamellae, 2 for each composition, were prepared at different positions out of the absorbers using a FIB system.

By evaluating the local chemical composition of the absorbers by EDS and nano-XRF the coexistence of CZTSSe kesterite material and ZnS(Se) secondary phase segregations was detected for Cu-poor and Zn-rich growth conditions. The size and number of the secondary phases severely fluctuate within the absorber and increase when the synthesis conditions become Cu-poorer and Zn-richer. In contrast, the sample preparation close to stoichiometry reveals no secondary phase segregation. Furthermore, the anion distribution showed strong fluctuations leading to a reduced effective band gap and V_{OC}. A detailed analysis of the cation distribution reveled local compositional variations with respect to each other and to the nominal content. The overall composition of the CZTSSe phase is less Cu-poor and less Zn-rich than the nominal composition when ZnS(Se) segregations are present, although it still remains Cu-poor and Zn-rich. Certain deviations from stoichiometry are associated with different off-stoichiometry types, which possesses point defects. Under Cu-poor and Zn-rich conditions the absorber exhibits a broad variety of off-stoichiometry types and harmful defects, but overall the beneficial A-type is dominant. On the other hand, close to stoichiometry an almost absence of the A off-stoichiometry type was observed and a much broader variety of harmful point defects likely accompanied by detrimental ($2Cu_{Zn}^{-}$ + Sn_{Zn}^{2+}) defect complexes, which reduce the effective band gap. In this context, the highest power conversion efficiency achieved the Cu-poorest and Zn-richest composition in good agreement to the lowest variation of the off-stoichiometry types. In the same way, this absorber showed the highest number of ZnS(Se) secondary phases indicating that they are not the main limitation at the current level of performance. The high sensitivity of the hard X-ray nanobeam enabled the observation of even smaller ZnS(Se) secondary phases, whose sizes decrease down to the resolution limit of the beam. Moreover, less Cu-poor and less Zn-rich domains were identified, but also selected grain boundaries with increased Cu, decreased Zn, and unchanged Sn content for some absorber compositions. Overall, these findings demonstrate that the integral measured composition can be misleading and does not completely represent the true picture of this complex quaternary material system. Accordingly, the estimation of the present defects in off-stoichiometric CZTSSe absorbers are not reliable and care has to be taken when correlating them with electrical properties or conversion efficiencies.

7. Local electrical properties of Rb-enriched grain boundaries in Cu(In,Ga)Se_2 solar cells

This chapter reports on an effective strategy for spatially resolved tracking of the local composition of RbF post-deposition treated CIGS solar cells on a nanometer scale during operation. Thereby, compositional gradients of In and Ga were found to enhance the collection efficiency, whereas Rb-enriched random grain boundaries were predominantly benign. The solar cells were fabricated by Dr. Philip Jackson and provided by Dr. Roland Würz (Zentrum für Sonnenenergie- und Wasserstoff-Forschung, ZSW). Combined nano-XRF and nano-XBIC measurements were performed in collaboration with Christian Plass (see his master's thesis [70]), Dr. Sven Schönherr, Dr. Philipp Schöppe, Maximilian Zapf, Martin Hafermann, as well as Dr. Jaime Segura-Ruiz, Dr. Andreas Johannes, Dr. Damien Salomon (European Synchrotron Radiation Facility, ESRF) and Dr. Gema Martínez-Criado (Instituto de Ciencia de Materiales de Madrid, CSIC). Parts of this chapter are published in reference [69].

7.1. Motivation

Among all thin film photovoltaics chalcogenide Cu(In,Ga)Se_2 solar cells achieve one of the highest efficiencies [22]. The main breakthroughs in recent years were achieved by applying an alkali fluoride PDT after the absorber synthesis [25, 53–55, 307]. The current world record efficiency of 23.35 % [25] uses a CsF treatment, whereas RbF is only slightly less efficient [55]. So far the mechanism behind this efficiency improvement is not fully understood and controversially discussed. Several groups reported on alkali agglomeration at detrimental, random grain boundaries and at the interfaces between front and back contact [56–62, 158, 159, 308]. Complementary DFT calculations proposed a reduced recombination probability of the generated charge carriers at these interfaces and grain boundaries by a possible passivation of the detect states [58, 65]. In contrast, other studies claimed that there is no evidence for passivation at grain boundaries by alkalis [63]. Therefore, it is of great interest to determine the local composition and the electrical activity of the absorber under operando conditions

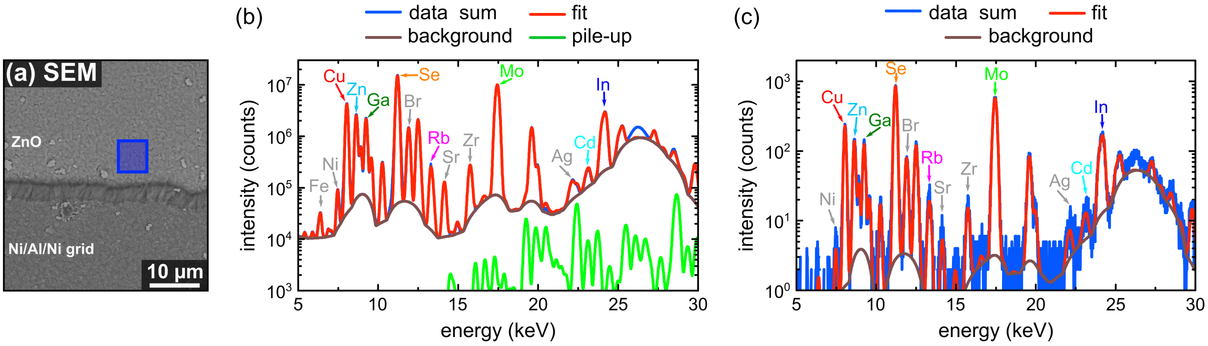

Figure 7.1.: (a) SEM image of the CIGS solar cell surface with a schematic drawing of the measuring positions (blue area). Nano-XRF spectra including the fit, background and pile-up of the whole investigated (b) and for a single pixel (c) with a size of 50 × 50 nm^2. The data were evaluated using the PyMCA code [211].

at the same time. Advanced synchrotron-based techniques provide the possibility to investigate the local composition by XRF and the collection efficiency by XBIC on a nanometer scale and are sensitive to subtle variations at grain boundaries [217, 219, 220, 309].

To gain detailed insights in the local functionality, a highly efficient CIGS solar cell subjected to a RbF-PDT, which was grown in the same run as a previous world record device [55], was investigated in-operando by simultaneous nano-XRF and nano-XBIC measurements in top-view geometry. The electrical parameters of the CIGS solar cell were determined to be: $\mu = 20.1\,\%$, $J_{SC} = 36.4\,\mathrm{mA/cm^2}$, $V_{OC} = 753.0\,\mathrm{mV}$, fill factor = 73.3 %. Prior, the local composition of this particular solar cell was investigated by nano-XRF on a cross-sectional lamella revealing Rb agglomerations at random grain boundaries [57]. For details about the solar cell synthesis and measurement see section 3.1.4 and 3.2.3, respectively.

7.2. Detection of Rb

The SEM image in figure 7.1a shows the surface of the CIGS solar cell consisting of the ZnO front contact and the Ni/Al/Ni grid. The corresponding nano-XRF spectra taken in the blue highlighted area and for a single pixel (50 × 50 nm^2) are depicted in figure 7.1b and c, respectively. A variety of peaks representing the different elements of the front contact, the CIGS absorber, and back contact can be identified. The most interesting peak is visible at roughly 13.4 keV, which coincides with the Rb K_α-line at 13.395 keV. This highlights the possibility to detect smalls amounts of Rb even when measuring through the front contact and averaging over of the whole absorber. Gray colored elements in figure 7.1b and c stem either from the contact grid (Ni), the

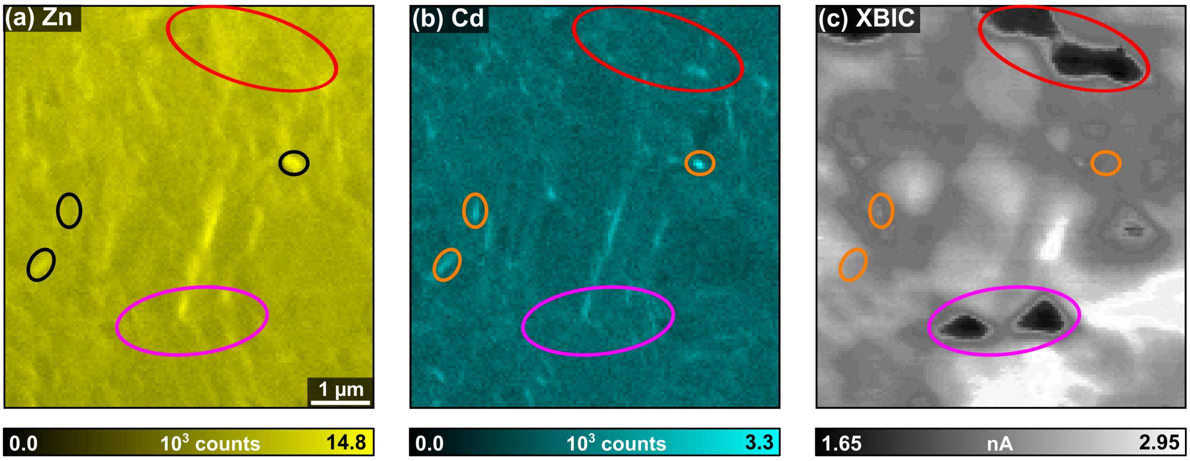

Figure 7.2.: Fitted nano-XRF intensity maps of Zn (a) and Cd (b) representing the front contact and buffer layer of the CIGS solar cell, respectively, as well as the corresponding nano-XBIC signal (c). Selected areas are marked by colored ovals.

conducive silver used to contact the solar cell, or from the experimental setup, such as the sample holder, piezo stage, etc., excited by secondary excitation or scattered X-rays. In the high energy region - roughly starting at 21 keV - the background drastically increases because the 7 element silicon drift detector suffered from electronic noise for higher fluorescence energies. Nevertheless, this increase does not drastically influence the data evaluation since the PyMCA software code [211] is able to model a suitable background.

7.3. Influence of the window layer on the current signal

Plotting the number of fitted counts associated with a certain florescence line as a function of the beam position yields two-dimensional top-view projections of Zn and Cd in figure 7.2a and b representing the ZnO front contact and CdS buffer layer. Both maps exhibit characteristic point and line like shapes that likely reflect the surface topography of the underlying CIGS absorber. Valleys on the absorber surface are commonly caused by grain boundaries. The chemical bath deposited buffer layer and magnetron sputtered front contact usually fill these valleys, thus forming thicker regions with higher fluorescence intensities compared to the deposition on elevated areas. However, it is worth noting that not all grain boundaries form valleys. The simultaneously measured nano-XBIC map is illustrated in figure 7.2c. It allows to investigate whether inhomogeneities in the window layer such as thickness variations influence the locally generated current signal. In accordance with the Zn and Cd elemental map, no clear correlation can be observed (see ovals). Especially the large characteristic dark areas with a significantly reduced current signal (see violet and red ovals) cannot be explained by variations of the front contact or buffer layer, respectively. Thus, the locally induced current is not influenced by the window layer.

7.4. Impact of the local absorber composition to the collection efficiency

Fitting the spectrum of every individual pixel enables the quantification of the local atomic concentration. Figure 7.3a-e shows the concentration maps for the elements in the CIGS absorber (for intensity maps see figure A.10 in the appendix). A slight compositional gradient is present in vertical direction (see white rectangle in figure 7.3a), which can be explained by partial attenuation of the CIGS fluorescence signal by the contact grid. Indeed this effect is pretty low, as shown by an almost homogeneous Se distribution in figure 7.3d, which coincides with the expected stoichiometry of 50 at.% of Se in Cu(In,Ga)Se_2. Nevertheless, the following data analysis focuses on relative variations on a very small scale.

Figure 7.3e shows Rb segregations in specific regions featuring a net-like distribution with line and point-like shapes. In previous investigations on CIGS solar cells and especially on cross-sectional lamella prepared out of the same solar cell, Rb agglomerations were found at random grain boundaries [57, 59]. Therefore, the line like features can be attributed to Rb-enriched random grain boundaries, which are almost perpendicular to the solar cell layers. Accumulations of very small grains with random orientation of adjacent grains were found close to the back contact for this cell [57] and explain the point-like characteristics in figure 7.3e. At the interfaces to the front and back contact an increased Rb content was observed as well [57]. In the presented top view geometry, the hard X-ray beam enters the solar cell perpendicular, thus slight variations at the interfaces and at random grain boundaries, which are parallel or exhibit a shallow angle to the layer interfaces cannot be detected.

By comparing the Rb distribution with the remaining absorber elements, a clear anti-correlation pattern to the Cu map can be observed in figure 7.3a, i.e., higher Rb concentrations correspond to Cu depletion. These findings are in excellent agreement to the lamella investigations [57], but also to atom probe tomography measurements [59]. A similar inverse anti-correlation pattern can also be identified for In and Ga in figure 7.3c and d. The white ovals indicate regions where In is enriched while the Ga concentration is depleted. In fact, this vice versa behavior of In and Ga is

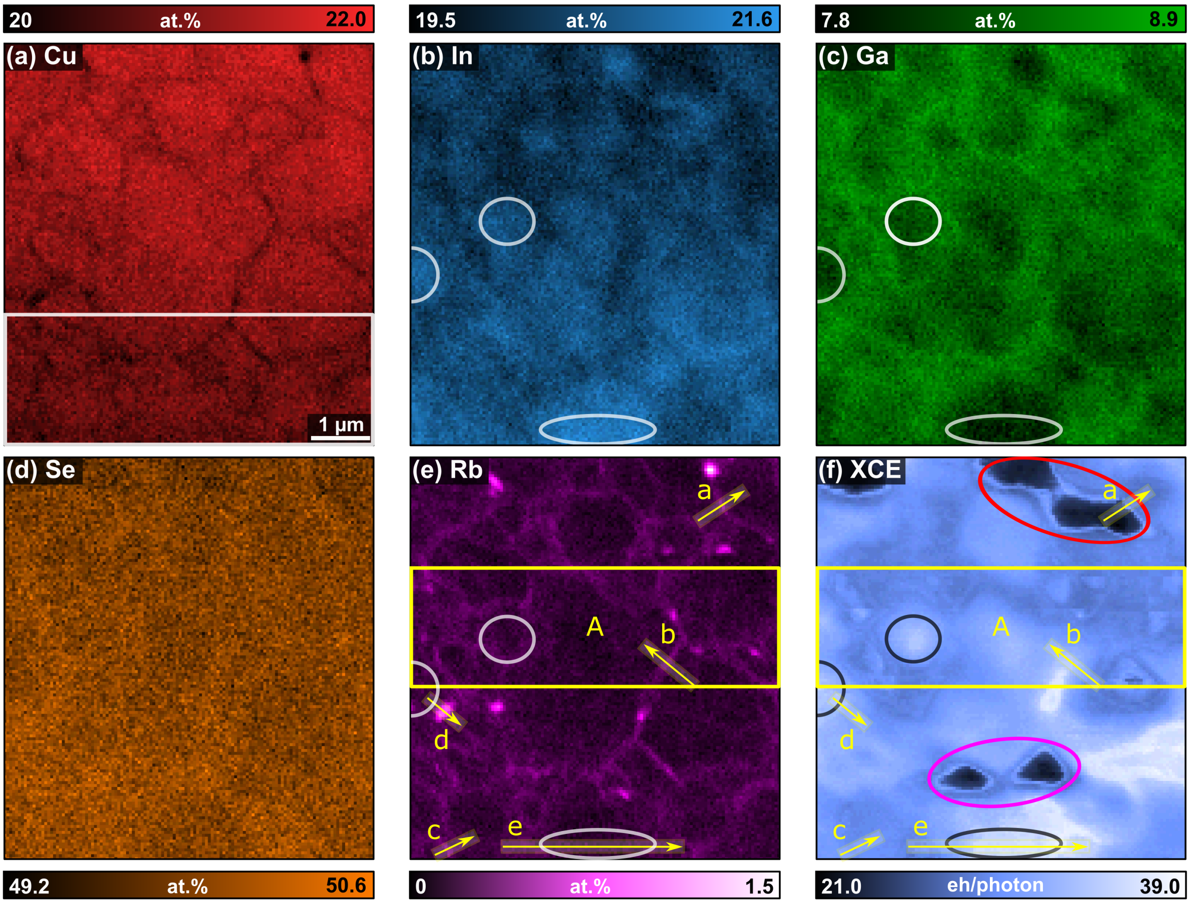

Figure 7.3.: Atomic concentration maps for the elements present in the CIGS absorber (a-e) obtained by fitting the nano-XRF spectrum of each individual pixel using the PYMCA code [211]. (f) XCE map calculated from the XBIC signal in figure 7.2c. The red and violet ovals mark regions with a reduced XCE, while the white/black ovals mark regions with an increased XCE, In enrichment, and Ga depletion. The yellow arrows indicate the positions of the line profiles shown in figure 7.4.

expected, since both elements share one lattice site. Finally, the Se map owns an almost homogeneous distribution with a concentration of approximately 50 at.% in excellent agreement to the initial growth conditions and the nominal stoichiometry.

Variations in composition, especially of the incorporated Rb, can influence the local efficiency. The latter is reflected in the simultaneous measured XBIC signal. Compositional dependent electron-hole pair generation efficiencies and thickness variations influence the XBIC signal. Therefore, the X-ray collection efficiency was calculated for each pixel according to section 2.3.4 and plotted in figure 7.3f. In particular, the XCE is a measure for the number of electron-hole pairs that are collected per absorbed photon. The most striking areas in figure 7.3f (see red and violet ovals) are the same as already deduced in figure 7.2c, showing a significantly reduced collection efficiencies, which do not correlate with the elemental distribution. It is indeed difficult to deduce the origin, as several options have to be taken into account such as defects, interface recombination, local shunts, or a locally enhanced series resistance of particular grains. Furthermore, void formation or the delamination of the absorber or buffer layer causing a missing contact towards the front or back contact is rather unlikely, since it was not observed in the respective cross-sectional STEM investigation [57].

The areas marked by white and black circles/ovals in figure 7.3b,c, and f exhibit an anti-correlation pattern between the In and Ga concentrations correlating with an enhanced XCE. Following the Rb distribution in figure 7.3e and accordingly the grain boundary positions, these areas seem to be grains with an increased In concentrations. Several aspects could contribute to this interrelation: A change in the In/Ga ratio introduces a band bending by decreasing the conduction band minimum towards the grain interior [76, 77]. The resulting force drags the electrons away from the grain boundaries where the recombination probability is expected to be higher [33, 34, 108] and explains the local increase in efficiency. However, even though the XCE is corrected for different absorption probabilities, subsequent effects of the hot electrons generating electron-hole pairs (such as electron-scattering, Auger-effects, etc.) might not be fully addressed by the formula derived by Stuckelberger et al. [217].

Lateral variations within the composition and XCE maps make it difficult to observe small changes at grain boundaries. Therefore, figure 7.4a-c shows three line profiles extracted perpendicular across representative random grain boundaries (see yellow arrows in figure 7.3e and f). Here, narrow and bright Rb accumulations were used, as they are very likely perpendicular to the cell surface/scanning plane. The line profiles corroborate the previous mentioned anti-correlation of Cu and Rb deduced from the 2D maps. An increased Rb concentration is accompanied by a Cu reduction at the grain boundaries, whereas the reaming cations are homogeneously distributed. Additionally, a slight enhancement of the Se content in line profile a and c might be visible within the noise level of the experimental approach. The impact of the grain boundaries on the electrical signal is reflected in the XCE signal, which is dominated by the adjacent grains due to varying efficiencies. However, the scans reveal different features for the grain boundaries. In figure 7.4a the XCE signal is slightly enhanced, whereas in figure 7.4b the signal is smooth within the experimental uncertainty. Therefore, the Rb-enriched grain boundaries do no influence the local collection efficiency and might even have a positive effect. Previous EBIC and cathodoluminescence studies on CIGS solar cells without Rb-PDT reported on detrimental effects of random grain boundaries caused by defect states [33, 34, 108]. Thus, these findings strongly indicate a partial passivation of defects at random grain boundaries by Rb. In contrast, the XCE signal in figure 7.4c has a dip at the grain boundary position. Furthermore, point-like

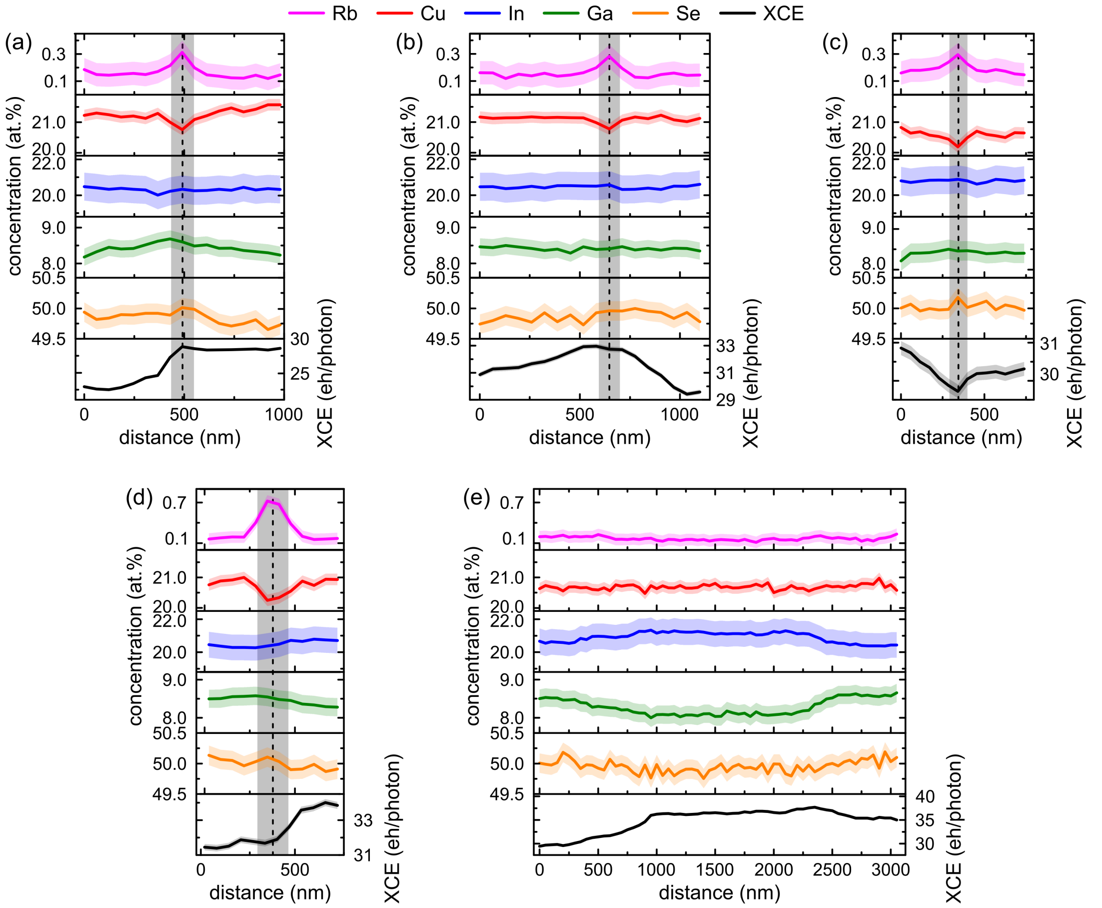

Figure 7.4.: Five lines profiles extracted along the yellow marked arrows in figure 7.3. The line profiles were averaged over a width of 250 nm (5 pixel). The black dashed line in (a-d) marks the Rb-enriched grain boundary, while the the gray background roughly marks the full width half maximum of the Rb signal. The measurement uncertainty is illustrated by the colored shades (covered by the line thickness in the XCE for a and e).

shapes in the Rb map were assigned to agglomerations of small grains with random orientation to each other. A representative line profile of such a spot is shown in figure 7.4d and shows a slightly reduced signal as well. Thus, these features seem to be still detrimental because not all grain boundaries are sufficient passivated by Rb. Therefore, further knowledge about the different grain boundary types is of exceptional interest. Additionally, it should be beneficial to avoid small grains at the back contact during the absorber synthesis. The last line profile in figure 7.4e again highlights the inverse In/Ga gradient towards the grain interior and corroborates the band bending likely causing an increased XCE signal.

To investigate the general impact of lateral variations on the overall efficiency correlation plots were generate out of area A (see figure 7.3e and f). In figure 7.5 the concentration of the different absorber elements are plotted as a function of the corresponding XCE signal for every pixel independently. The area was defined in a way to

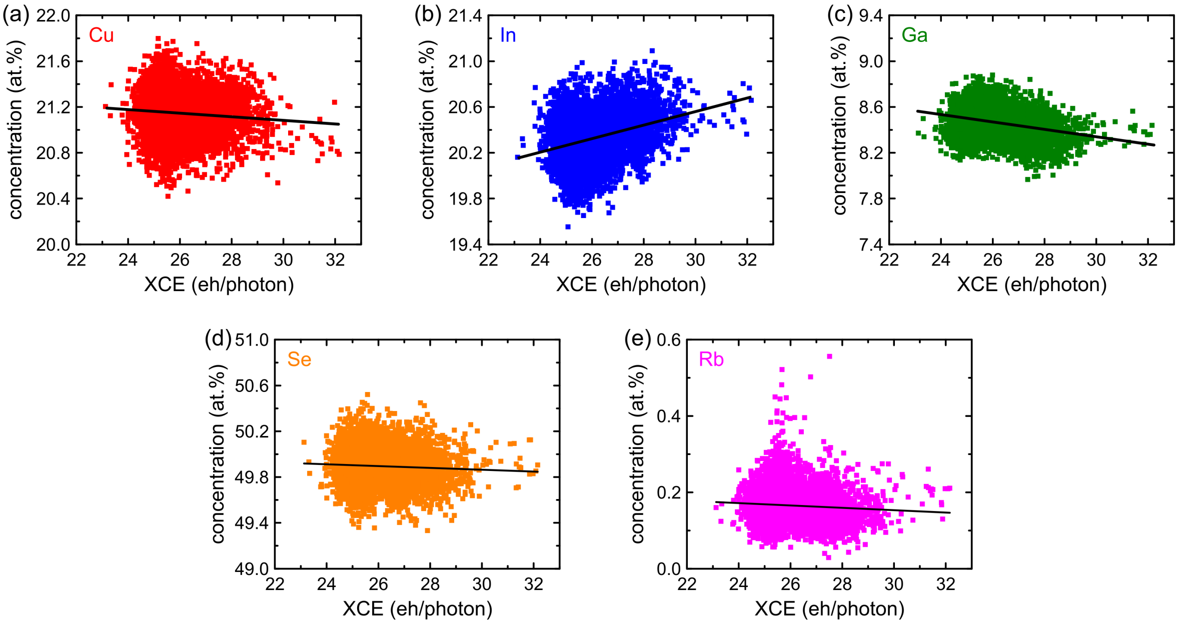

Figure 7.5.: Correlation plots, showing the concentrations of the absorber elements as a function of the XCE signal in the yellow marked area A in figure 7.3e and f. The black lines represent the respective fit through all data points, to guide the eye on the trend.

mostly exclude the bright spots in the Rb map, as they showed a reduced collection efficiency. The most conspicuous trend can be observed in the concentration of In and Ga. However, the syllogism ”more In results in a higher collection efficiency” is misleading when applied to the integral concentration, considering the previously discussed microstructural view. Consequently, the increase in the local collection efficiency for higher In content is not necessarily attributed to a better solar cell efficiency for In-richer absorbers but likely to the band bending in individual grains and their interfaces. For the remaining elements no distinct correlation can be observed. Indeed, this was expected for Se, since it is almost homogeneously distributed within the absorber. Accordingly, the fluctuations in figure 7.5d is almost random with no significant influence on the local collection efficiency. The most interesting compositional correlations are those of Cu and Rb, as they are direct indicators of random grain boundaries. In the case of a detrimental effect of these grain boundaries a clear correlation with the local collection efficiency for both elements should be present, as Cu is depleted and Rb is enriched. Furthermore, the interrelations should have opposite trends. However, neither of the two elements shows such a behavior. Especially, the Rb correlation plot in figure 7.5e, which is the best indicator for the grain boundaries, shows no correlation with the local collection efficiency. Therefore, most Rb-enriched grain boundaries have no detrimental effect on the overall collection efficiency. In consequence, the random grain boundaries are most likely passivated to a large extend, explaining the conversion efficiency boost achieved by RbF-PDT.

7.5. Summary

In-operando investigations of a highly efficient CIGS solar cell subjected to a RbF-PDT gave access to the local composition and local collection efficiency by simultaneous nano-XRF and nano-XBIC measurements in top-view geometry. The front contact elements covered the complete investigated area and slight fluctuations were identified, which were assigned to the surface morphology. However, these fluctuations had no influence on the locally induced current. Despite probing in top-view geometry the technique allowed to detect the Rb distribution spatially resolved on a nanometer scale within the absorber. It agglomerates in selected areas, forming line and point-like shapes. The Rb accumulation is accompanied by Cu depletion, while the remaining absorber components remain unchanged. Furthermore, an increased In concentration within the grains was identified accompanied by Ga depletion, while a vice versa trend towards the grain boundaries was observed. Independent on the cation distribution, Se was found to be almost homogeneously distributed. The observed compositional variations beneficially affect the collection efficiency. Generated electrons are dragged towards the grain interior by the In gradient, which induces a band bending. Finally, the random grain boundaries, identified by Rb, mainly showed no significant correlation with the collection efficiency. This strongly indicates partial or complete passivation of these grain boundaries by Rb.

8. Conclusion and outlook

Thin film chalcogenide and kesterite solar cells are promising technologies being part of the solution for climate change. They are, above all, characterized by the low material expenditure, energy-efficient production, and non-toxic constituents [14–16]. Furthermore, they show long-term stability and have a short energy payback time [14, 15, 17–20]. However, their efficiency is lower than the theoretically predicted limit. Thus, it is of particular interest to explore the performance-limiting features of these emerging materials. Therefore, three key challenges were considered within this thesis: (i) The local absorber composition along with possible compositional and structural inhomogeneities on different length scales were investigated to understand the performance-limiting properties in thin film solar cells. (ii) The presence, localization and role of Ge after the synthesis of Ge-doped CZTSe absorbers was analyzed, to understand the beneficial effect of Ge. (iii) Investigations of the electrical properties of Rb-enriched random grain boundaries in CIGS solar cells were conducted to examine whether they have a negative influence on the efficiency. Advanced synchrotron nanoprobe-based and electron microscope techniques as well as in-operando electrical characterizations provided insights to these challenges.

Chapter 5 addressed the first two key challenges. Highly efficient Ge-doped CZTSe solar cells with three different nominal compositions and levels of performance were synthesized in a sequential process by IREC. The preparation of cross-sectional lamellae enabled to determine the spatially resolved composition and their correlation with structural and microstructural properties. Morphological STEM investigations revealed large grains but also detrimental voids at the back contacts interface. For the main absorber components, an almost homogeneous elemental distribution, independent of the nominal composition, was identified by EDS and XRF. The quantification of the local composition by EDS almost coincided with the nominal off-stoichiometric composition; however, small variations could be identified for the Zn/Sn ratio. Thus, most regions in the absorbers were assigned to the off-stoichiometry type A featuring the beneficial Cu vacancies and only a few regions exhibited off-stoichiometry types with performance-limiting defects. This highlights the possibility to grow off-stoichiometric CZTSe free of secondary phases for a wide compositional range using the sequential process. Furthermore, XRF analysis showed subtle compositional variations at the hetero-interfaces. In consequence, the varying performances were assigned to different doping levels and the formation of detrimental defect complexes, while the main performance limitation was found at the interfaces.

Additionally, it was demonstrated by nano-XRF analysis that Ge remains in the absorber after the synthesis where it is heterogeneously distributed. While small amounts incorporated within the grains likely have a negligible impact on the V_{OC}, the absence of Ge at random grain boundaries was detected, which leads to an attractive force for electrons and likely slightly lessens the overall beneficial effect of Ge. Moreover, nano-XANES measurements revealed detrimental nanoscale GeO_2 secondary phases, which should be avoided during the growth process, even though the improvement in the conversion efficiency might be rather small due to their low concentration and small size.

Based on these new insights, future work should focus on the minimization of holes at the back contact to decrease the series resistance. The main compositional non-uniformity associated with detrimental point defects was detected at the interfaces. Thus, an effective strategy needs to be developed to either avoid these fluctuations, remove this transition layer, or passivate the detrimental defects, present in this layer. Although the absorber does not seem to be the main limitation, detrimental Ge-poor random grain boundaries were found, which likely limit the efficiency. To elucidate their impact, complementary measurement methods like EBIC, XBIC, or CL measurements should be applied to the same lamellae, which allows for a comprehensive understanding on the carrier recombination.

Chapter 6 addressed the first key challenge and investigated compositional and microstructural properties of highly efficient CZTSSe absorbers, prepared by IMRA Europe in a non-toxic spray coating process. Compositional investigations by EDS and nano-XRF on absorbers with a nominal Cu-poor and Zn-rich composition revealed the formation of a Mo-Cu-(S,Se) interface layer between Mo and CZTSSe. Furthermore, compositional analysis showed the coexistence of ZnS(Se) secondary phases along with CZTSSe. The kesterite composition remained Cu-poor and Zn-rich although, on average, less Cu-poor and Zn-rich compared to the initial conditions. This proved the possibility to grow off-stoichiometric CZTSSe and that the cation ratios are not constrained to 1. Synthesis conditions close to stoichiometry showed no secondary phase segregations and the smallest deviation between nominal and integral measured composition. Despite the absence of ZnS(Se), the stoichiometric grown sample possessed the lowest conversion efficiency. This could be linked to local compositional variations within the absorber, connected to detrimental defects and the formation of Cu-rich domains, featuring detrimental defect complexes. In contrast, Cu-poor and Zn-rich absorbers showed less detrimental defects, more domains with the A off-stoichiometry type, and no indication for harmful defect complexes. In this context, the Cu-poorest and Zn-richest growth condition lead to the highest conversion efficiency, despite the formation of the highest amount of ZnS(Se) secondary phases that were also the biggest in size. This indicates that ZnS(Se) secondary phases are not the main limitation at the current level of performance. Furthermore, an increased Cu content and reduced Zn content was identified by nano-XRF at specific grain boundaries, which likely reduces the p-type conductivity and enhances the carrier recombination. In addition to the variations in the cation distribution, fluctuations in the cation concentrations were identified, resulting in a reduced effective band gap, harming the V_{OC}.

To overcome the efficiency limitation, future research should focus on a more homogeneous elemental distribution in Cu-poor and Zn-rich absorbers but also on the suppression of ZnS(Se) secondary phases, as they are the reason for the discrepancy between nominal and realized composition. In fact, growth of homogeneous absorbers that are free from secondary phases is one of the biggest challenges for kesterite. Changing the growth conditions from a tri-molecular process towards mainly bi-molecular might help to enhance the absorber quality similar to the findings in chapter 5 and reference [50]. This might be achieved either using tri-molecular colloids or by small amounts of Ge. Moreover, the diffusion of Cu into the Mo(S,Se) might promote the formation of ZnS(Se) secondary phases as well as voids and should be avoided.

In chapter 7, the first and third key challenge were addressed in a combinatorial approach by tracking the local composition and collection efficiency at the nanometer scale. The measurements were performed in top view geometry on a RbF post deposition treated CIGS solar cell prepared in a multi stage co-evaporation process from the ZSW. Fluctuations of the collection efficiency between different areas on the solar cell were observed. The most prominent areas possessed a strongly decreased collection efficiency, which could not be explained by non-uniformity of the window layer and did not correlate with the local composition. It was also demonstrated that an increased XCE is present in In-enriched grains. This was attributed to the band bending and the related force dragging the electrons towards the grain interior. The high sensitivity of nano-XRF and nano-XBIC also enabled to detect the Rb agglomerations at random grain boundaries and the effect on the collection efficiency. Rb agglomerations were detected in selected regions forming line and point-like structures. The line shapes could

be assigned to single grain boundaries perpendicular to the solar cell layer and showed mostly no significant correlation with the XCE. However, point-like structures, which are most likely accumulations of small grains with random orientation to each other, showed a reduced XCE. These results indicate that most random grain boundaries are partially or completely passivated by Rb, whereas the agglomerations of small grains are detrimental to the performance.
Based on these new findings, agglomerations of small grains should be avoided to further enhance the efficiency. Additionally, a minor amount of grain boundaries that were not sufficiently passivated was found. Complementary measurement methods should be used to understand the difference to the passivated ones. Of particular interest are the areas where the XCE has drastically decreased, as these are likely to have a major impact on the efficiency. Here, it is also important to facilitate complementary techniques in order to understand the origin and to avoid such regions in future cells. Furthermore, it is interesting to expand this kind of characterization technique to CIGS solar cells treated with different alkali metals, but also to the kesterite-based solar cells. More insights into the local electrical characteristics will be gained by measuring XBIC voltage dependently, which then denotes as X-Ray beam induced voltage (XBIV) [216, 310]. This technique enables to measure complete I-V curves at the nanoscale and gives access to the local key photovoltaic parameters.

The experimental results on compositional, structural, and functional investigations of kesterite and chalcogenide thin film solar cells have successfully addressed the three key challenges. They provide a valuable contribution to the understanding of performance-limiting features on different length scales. This might help to develop future kesterite and chalcogenide solar cells with higher efficiencies, making them an energy and material-conserving complement to the widely used silicon solar cells. Both silicon and alternative solar cells are urgently needed to reach the objective of decarbonized energy production and thus compliance with the Paris Agreement.

Bibliography

[1] U.S. Energy Information Administration, International Energy Outlook 2019.

[2] UNFCCC., Historic Paris Agreement on Climate Change - 195 Nations Set Path to Keep Temperature Rise Well Below 2 Degrees Celsius. **2015**.

[3] 2020 (IEA), Global Energy Review 2019, IEA, Paris.

[4] R. B. Jackson, P. Friedlingstein, R. M. Andrew, J. G. Canadell, C. Le Quéré, G. P. Peters, *Environmental Research Letters* **2019**, *14*, 121001.

[5] Aligning-national-and-international-climate-targets, Grantham Research Institute on Climate Change, **2018**.

[6] Fridays For Future, **05.10.2020**, `https://fridaysforfuture.org/` (visited on 10/07/2020).

[7] C. Breyer, D. Bogdanov, A. Gulagi, A. Aghahosseini, L. S. Barbosa, O. Koskinen, M. Barasa, U. Caldera, S. Afanasyeva, M. Child, J. Farfan, P. Vainikka, *Progress in Photovoltaics: Research and Applications* **2017**, *25*, 727–745.

[8] D. Bogdanov, J. Farfan, K. Sadovskaia, M. Fasihi, M. Child, C. Breyer, *Japanese Journal of Applied Physics* **2018**, *57*, 08RJ01.

[9] European Technology and Innovation Platform for Photovoltaics. Photvoltaic Solar, ETIP PV, **2019**.

[10] S. Chu, A. Majumdar, *Nature* **2012**, *488*, 294–303.

[11] C. Philibert, *Solar energy perspectives*, OECD/IEA, Paris, **2011**.

[12] Philipps S., W. Warmuth, Photovoltaics Report, **2020**.

[13] *Handbook of photovoltaic science and engineering*, 2. ed., (Eds.: A. Luque López, S. Hegedus), Wiley, Chichester, **2011**.

[14] K. P. Bhandari, J. M. Collier, R. J. Ellingson, D. S. Apul, *Renewable and Sustainable Energy Reviews* **2015**, *47*, 133–141.

[15] A. Goetzberger, V. U. Hoffmann, *Photovoltaic solar energy generation*, Springer, Berlin, **2005**.

[16] D. C. Jordan, S. R. Kurtz, K. VanSant, J. Newmiller, *Progress in Photovoltaics: Research and Applications* **2016**, *24*, 978–989.

[17] A. Chirilă, S. Buecheler, F. Pianezzi, P. Bloesch, C. Gretener, A. R. Uhl, C. Fella, L. Kranz, J. Perrenoud, S. Seyrling, R. Verma, S. Nishiwaki, Y. E. Romanyuk, G. Bilger, A. N. Tiwari, *Nature materials* **2011**, *10*, Letter, 857–861.

[18] A. Gerthoffer, F. Roux, F. Emieux, P. Faucherand, H. Fournier, L. Grenet, S. Perraud, *Thin Solid Films* **2015**, *592*, 99–104.

[19] S. Khelifi, A. Belghachi, J. Lauwaert, K. Decock, J. Wienke, R. Caballero, C. Kaufmann, M. Burgelman, *Energy Procedia* **2010**, *2*, 109–117.

[20] J. Poortmans, V. Archipov, *Thin film solar cells, Fabrication, characterization and applications*, Wiley, Chichester, **2006**.

[21] J. Ramanujam, D. M. Bishop, T. K. Todorov, O. Gunawan, J. Rath, R. Nekovei, E. Artegiani, A. Romeo, *Flexible CIGS, CdTe and a-Si:H based thin film solar cells: A review*, *Vol. 110*, **2020**.

[22] M. A. Green, E. D. Dunlop, J. Hohl–Ebinger, M. Yoshita, N. Kopidakis, X. Hao, *Progress in Photovoltaics: Research and Applications* **2020**, *28*, 629–638.

[23] W. Shockley, H. J. Queisser, *Journal of Applied Physics* **1961**, *32*, 510–519.

[24] S. Rühle, *Solar Energy* **2016**, *130*, 139–147.

[25] Solar Frontier GmbH, Ed., Solar Frontier Achieves World Record Thin-Film Solar Cell Efficiency of 23.35%, Tokyo.

[26] J.-F. Guillemoles, T. Kirchartz, D. Cahen, U. Rau, *Nature Photonics* **2019**, *13*, 501–505.

[27] G. Phipps, C. Mikolajczak, T. Guckes, *Indium and Gallium: long-term supply*, *Vol. 9*, **2008**.

[28] *The environmental geochemistry of mineral deposits*, (Ed.: L. H. Filipek), Soc. of Economic Geologists, Chelsea, Mich., **1999**.

[29] W. Wang, M. T. Winkler, O. Gunawan, T. Gokmen, T. K. Todorov, Y. Zhu, D. B. Mitzi, *Advanced Energy Materials* **2014**, *4*, 1301465.

[30] S. Siebentritt, *Solar Energy Materials and Solar Cells* **2011**, *95*, 1471–1476.

[31] H. J. Queisser, *Science* **1998**, *281*, 945–950.

[32] S. Chen, A. Walsh, X.-G. Gong, S.-H. Wei, *Advanced materials (Deerfield Beach Fla.)* **2013**, *25*, 1522–1539.

[33] D. Abou-Ras, J. Dietrich, J. Kavalakkatt, M. Nichterwitz, S. S. Schmidt, C. T. Koch, R. Caballero, J. Klaer, T. Rissom, *Solar Energy Materials and Solar Cells* **2011**, *95*, 1452–1462.

[34] D. Abou-Ras, N. Schäfer, T. Rissom, M. N. Kelly, J. Haarstrich, C. Ronning, G. S. Rohrer, A. D. Rollett, *Acta Materialia* **2016**, *118*, 244–252.

[35] J. Just, C. M. Sutter-Fella, D. Lützenkirchen-Hecht, R. Frahm, S. Schorr, T. Unold, *Physical chemistry chemical physics : PCCP* **2016**, *18*, 15988–15994.

[36] P. Schöppe, G. Gurieva, S. Giraldo, G. Martínez-Criado, C. Ronning, E. Saucedo, S. Schorr, C. S. Schnohr, *Applied Physics Letters* **2017**, *110*, 043901.

[37] Y. Yan, R. Noufi, K. M. Jones, K. Ramanathan, M. M. Al-Jassim, B. J. Stanbery, *Applied Physics Letters* **2005**, *87*, 121904.

[38] D. Abou-Ras, S. S. Schmidt, R. Caballero, T. Unold, H.-W. Schock, C. T. Koch, B. Schaffer, M. Schaffer, P.-P. Choi, O. Cojocaru-Mirédin, *Advanced Energy Materials* **2012**, *2*, 992–998.

[39] D. Keller, S. Buecheler, P. Reinhard, F. Pianezzi, B. Bissig, R. Carron, F. Hage, Q. Ramasse, R. Erni, A. N. Tiwari, *Applied Physics Letters* **2016**, *109*, 153103.

[40] T. Schwarz, O. Cojocaru-Mirédin, P. Choi, M. Mousel, A. Redinger, S. Siebentritt, D. Raabe, *Journal of Applied Physics* **2015**, *118*, 095302.

[41] S. Giraldo, M. Neuschitzer, T. Thersleff, S. López-Marino, Y. Sánchez, H. Xie, M. Colina, M. Placidi, P. Pistor, V. Izquierdo-Roca, K. Leifer, A. Pérez-Rodríguez, E. Saucedo, *Advanced Energy Materials* **2015**, *5*, 1501070.

[42] E. Cadel, N. Barreau, J. Kessler, P. Pareige, *Acta Materialia* **2010**, *58*, 2634–2637.

[43] O. Cojocaru-Mirédin, P. Choi, R. Wuerz, D. Raabe, *Applied Physics Letters* **2011**, *98*, 103504.

[44] S. Kim, J.-S. Park, S. N. Hood, A. Walsh, *Journal of Materials Chemistry A* **2019**, *7*, 2686–2693.

[45] K. Biswas, S. Lany, A. Zunger, *Applied Physics Letters* **2010**, *96*, 201902.

[46] A. Kolmakov, S. Potluri, A. Barinov, T. O. Menteş, L. Gregoratti, M. A. Niño, A. Locatelli, M. Kiskinova, *ACS nano* **2008**, *2*, 1993–2000.

[47] N. N. Greenwood, A. Earnshaw, *Chemistry of the elements*, 2. ed., Butterworth-Heinemann, Oxford, **1997**.

[48] A. D. Collord, H. W. Hillhouse, *Chemistry of Materials* **2016**, *28*, 2067–2073.

[49] S. Giraldo, T. Thersleff, G. Larramona, M. Neuschitzer, P. Pistor, K. Leifer, A. Pérez-Rodríguez, C. Moisan, G. Dennler, E. Saucedo, *Progress in Photovoltaics: Research and Applications* **2016**, *24*, 1359–1367.

[50] S. Giraldo, E. Saucedo, M. Neuschitzer, F. Oliva, M. Placidi, X. Alcobé, V. Izquierdo-Roca, S. Kim, H. Tampo, H. Shibata, A. Pérez-Rodríguez, P. Pistor, *Energy & Environmental Science* **2018**, *11*, 582–593.

[51] L. Stolt, J. Hedström, J. Kessler, M. Ruckh, K.-.-O. Velthaus, H.-.-W. Schock, *Applied Physics Letters* **1993**, *62*, 597–599.

[52] M. A. Contreras, B. Egaas, P. Dippo, J. Webb, J. Granata, K. Ramanathan, *Proceedings of the 26th IEEE Photovoltaic Specialists* **1997**, 359–362.

[53] A. Chirilă, P. Reinhard, F. Pianezzi, P. Bloesch, A. R. Uhl, C. Fella, L. Kranz, D. Keller, C. Gretener, H. Hagendorfer, D. Jaeger, R. Erni, S. Nishiwaki, S. Buecheler, A. N. Tiwari, *Nature materials* **2013**, *12*, 1107–1111.

[54] P. Jackson, D. Hariskos, R. Wuerz, O. Kiowski, A. Bauer, T. M. Friedlmeier, M. Powalla, *physica status solidi (RRL) – Rapid Research Letters* **2015**, *9*, 28–31.

[55] P. Jackson, R. Wuerz, D. Hariskos, E. Lotter, W. Witte, M. Powalla, *physica status solidi (RRL) – Rapid Research Letters* **2016**, *10*, 583–586.

[56] P. Schöppe, S. Schönherr, R. Wuerz, W. Wisniewski, G. Martínez-Criado, M. Ritzer, K. Ritter, C. Ronning, C. S. Schnohr, *Nano Energy* **2017**, *42*, 307–313.

[57] P. Schöppe, S. Schönherr, P. Jackson, R. Wuerz, W. Wisniewski, M. Ritzer, M. Zapf, A. Johannes, C. S. Schnohr, C. Ronning, *ACS applied materials & interfaces* **2018**, *10*, 40592–40598.

[58] P. Schöppe, S. Schönherr, M. Chugh, H. Mirhosseini, P. Jackson, R. Wuerz, M. Ritzer, A. Johannes, G. Martínez-Criado, W. Wisniewski, T. Schwarz, C. T. Plass, M. Hafermann, T. D. Kühne, C. S. Schnohr, C. Ronning, *Nano Energy* **2020**, *71*, 104622.

[59] A. Vilalta-Clemente, M. Raghuwanshi, S. Duguay, C. Castro, E. Cadel, P. Pareige, P. Jackson, R. Wuerz, D. Hariskos, W. Witte, *Applied Physics Letters* **2018**, *112*, 103105.

[60] N. Taguchi, S. Tanaka, S. Ishizuka, *Applied Physics Letters* **2018**, *113*, 113903.

[61] M. Raghuwanshi, A. Vilalta-Clemente, C. Castro, S. Duguay, E. Cadel, P. Jackson, D. Hariskos, W. Witte, P. Pareige, *Nano Energy* **2019**, *60*, 103–110.

[62] R. Wuerz, W. Hempel, P. Jackson, *Journal of Applied Physics* **2018**, *124*, 165305.

[63] D. Abou-Ras, A. Nikolaeva, S. Caicedo Dávila, M. Krause, H. Guthrey, M. Al-Jassim, M. Morawski, R. Scheer, *Solar RRL* **2019**, *3*, 1900095.

[64] N. Nicoara, R. Manaligod, P. Jackson, D. Hariskos, W. Witte, G. Sozzi, R. Menozzi, S. Sadewasser, *Nature communications* **2019**, *10*, 3980.

[65] M. Chugh, T. D. Kühne, H. Mirhosseini, *ACS applied materials & interfaces* **2019**, *11*, 14821–14829.

[66] M. Ritzer, S. Schönherr, P. Schöppe, W. Wisniewski, S. Giraldo, G. Gurieva, A. Johannes, C. T. Plass, K. Ritter, G. Martínez-Criado, S. Schorr, E. Saucedo, C. Ronning, C. S. Schnohr, *ACS Applied Energy Materials* **2020**, *3*, 558–564.

[67] M. Ritzer, S. Schönherr, P. Schöppe, G. Larramona, C. Choné, G. Gurieva, A. Johannes, K. Ritter, G. Martínez-Criado, S. Schorr, C. Ronning, C. S. Schnohr, *physica status solidi (a)* **2020**, 2000456.

[68] R. Fonoll-Rubio, J. Andrade-Arvizu, J. Blanco-Portals, I. Becerril-Romero, M. Guc, E. Saucedo, F. Peiró, L. Calvo-Barrio, M. Ritzer, C. S. Schnohr, M. Placidi, S. Estradé, V. Izquierdo-Roca, A. Pérez-Rodríguez, *Energy & Environmental Science* **2021**, *14*, 507–523.

[69] C. T. Plass, M. Ritzer, P. Schöppe, S. Schönherr, M. Zapf, M. Hafermann, A. Johannes, G. Martínez-Criado, J. Segura-Ruiz, R. Würz, P. Jackson, C. S. Schnohr, C. Ronning, *ACS applied materials & interfaces* **2020**, *12*, 57117–57123.

[70] Christian Tobias Plass, Master's thesis, Friedrich Schiller University Jena, **2019**.

[71] M. I. Alonso, M. Garriga, C. A. Durante Rincón, E. Hernández, M. León, *Applied Physics A: Materials Science & Processing* **2002**, *74*, 659–664.

[72] M. Edoff, *Ambio* **2012**, *41 Suppl 2*, 112–118.

[73] S. S. Hegedus, W. N. Shafarman, *Progress in Photovoltaics: Research and Applications* **2004**, *12*, 155–176.

[74] Y. Yan, C.-S. Jiang, R. Noufi, S.-H. Wei, H. R. Moutinho, M. M. Al-Jassim, *Physical review letters* **2007**, *99*, 235504.

[75] S. Siebentritt, L. Gütay, D. Regesch, Y. Aida, V. Deprédurand, *Solar Energy Materials and Solar Cells* **2013**, *119*, 18–25.

[76] S. Wei, A. Zunger, *Journal of Applied Physics* **1995**, *78*, 3846–3856.

[77] M. Turcu, I. M. Kötschau, U. Rau, *Applied Physics A: Materials Science & Processing* **2001**, *73*, 769–772.

[78] Y. Kumagai, Y. Soda, F. Oba, A. Seko, I. Tanaka, *Physical Review B* **2012**, *85*.

[79] T. Tinoco, C. Rincón, M. Quintero, G. Pérez, *physica status solidi (a)* **1991**, 427–434.

[80] W. Shockley, W. T. Read, *Physical Review* **1952**, *87*, 835–842.

[81] R. N. Hall, *Physical Review* **1952**, *87*, 387.

[82] R. F. Pierret, *Advanced semiconductor fundamentals*, 2. ed., Pearson Education, Upper Saddle River, NJ, **2003**.

[83] Qian, Martin, Chadi, *Physical review. B Condensed matter* **1988**, *38*, 7649–7663.

[84] Neugebauer, C. G. van de Walle, *Physical review. B Condensed matter* **1994**, *50*, 8067–8070.

[85] G. A. Baraff, E. O. Kane, M. Schlüter, *Physical review. B Condensed matter* **1980**, *21*, 5662–5686.

[86] S. B. Zhang, S.-H. Wei, A. Zunger, H. Katayama-Yoshida, *Physical Review B* **1998**, *57*, 9642–9656.

[87] F. A. Kröger, H. J. Vink in *Solid state physics, Advances in research and applications*, Solid State Physics, Academic Press, **1955**, pp. 307–435.

[88] A. Bauknecht, S. Siebentritt, J. Albert, M. C. Lux-Steiner, *Journal of Applied Physics* **2001**, *89*, 4391–4400.

[89] I. Dirnstorfer, D. M. Hofmann, D. Meister, B. K. Meyer, W. Riedl, F. Karg, *Journal of Applied Physics* **1999**, *85*, 1423–1428.

[90] S. Siebentritt, *Thin Solid Films* **2002**, *403-404*, 1–8.

[91] F. Werner, D. Colombara, M. Melchiorre, N. Valle, B. El Adib, C. Spindler, S. Siebentritt, *Journal of Applied Physics* **2016**, *119*, 173103.

[92] R. Noufi, R. Axton, C. Herrington, S. K. Deb, *Applied Physics Letters* **1984**, *45*, 668–670.

[93] J. Bekaert, R. Saniz, B. Partoens, D. Lamoen, *Physical chemistry chemical physics : PCCP* **2014**, *16*, 22299–22308.

[94] M. Gloeckler, Colorado State University, Fort Collins, **2005**.

[95] T. Maeda, T. Wada, *Journal of Physics and Chemistry of Solids* **2005**, *66*, 1924–1927.

[96] J. Pohl, K. Albe, *Physical Review B* **2013**, *87*.

[97] M. Ruckh, D. Schmid, M. Kaiser, T. Walter, H. W. Schock, *Solar Energy Materials and Solar Cells* **1996**, *41/42*, 335–343.

[98] D. Braunger, D. Hariskos, G. Bilger, U. Rau, H. W. Schock, *Thin Solid Films* **2000**, *361-362*, 161–166.

[99] P. T. Erslev, J. W. Lee, W. N. Shafarman, J. D. Cohen, *Thin Solid Films* **2009**, *517*, 2277–2281.

[100] M. Martínez, *Journal of Materials Processing Technology* **2003**, *143-144*, 326–331.

[101] D. Schmid, M. Ruckh, H. SCHOCK, *Solar Energy Materials and Solar Cells* **1996**, *41-42*, 281–294.

[102] T. Wada, N. Kohara, S. Nishiwaki, T. Negami, *Thin Solid Films* **2001**, *387*, 118–122.

[103] L. Assmann, J. C. Bernède, A. Drici, C. Amory, E. Halgand, M. Morsli, *Applied Surface Science* **2005**, *246*, 159–166.

[104] S. M. Delphine, M. Jayachandran, C. Sanjeeviraja, *Materials Research Bulletin* **2005**, *40*, 135–147.

[105] S. Rauf, M. A. Nicolet, *Thin Solid Films* **1991**, *201*, 361–371.

[106] R. Kamada, T. Yagioka, S. Adachi, A. Handa, K. F. Tai, T. Kato, H. Sugimoto, *IEEE 43rd Photovoltaic Specialists Conference (PVSC)*, 1287–1291.

[107] D. Abou-Ras, R. Caballero, C. A. Kaufmann, M. Nichterwitz, K. Sakurai, S. Schorr, T. Unold, H. W. Schock, *physica status solidi (RRL) – Rapid Research Letters* **2008**, *2*, 135–137.

[108] D. Abou-Ras, S. S. Schmidt, N. Schäfer, J. Kavalakkatt, T. Rissom, T. Unold, R. Mainz, A. Weber, T. Kirchartz, E. Simsek Sanli, P. A. van Aken, Q. M. Ramasse, H.-J. Kleebe, D. Azulay, I. Balberg, O. Millo, O. Cojocaru-Mirédin, D. Barragan-Yani, K. Albe, J. Haarstrich, C. Ronning, *physica status solidi (RRL) – Rapid Research Letters* **2016**, *10*, 363–375.

[109] D. Schmid, M. Ruckh, F. Grunwald, H. W. Schock, *Journal of Applied Physics* **1993**, *73*, 2902–2909.

[110] M. Morkel, L. Weinhardt, B. Lohmüller, C. Heske, E. Umbach, W. Riedl, S. Zweigart, F. Karg, *Applied Physics Letters* **2001**, *79*, 4482–4484.

[111] T. Schulmeyer, R. Hunger, A. Klein, W. Jaegermann, S. Niki, *Applied Physics Letters* **2004**, *84*, 3067–3069.

[112] X.-H. Tan, S.-L. Ye, X. Liu, *Optics express* **2011**, *19*, 6609–6615.

[113] C. Platzer-Björkman, J. Lu, J. Kessler, L. Stolt, *Thin Solid Films* **2003**, *431-432*, 321–325.

[114] N. Naghavi, D. Abou-Ras, N. Allsop, N. Barreau, S. Bücheler, A. Ennaoui, C.-H. Fischer, C. Guillen, D. Hariskos, J. Herrero, R. Klenk, K. Kushiya, D. Lincot, R. Menner, T. Nakada, C. Platzer-Björkman, S. Spiering, A. N. Tiwari, T. Törndahl, *Progress in Photovoltaics: Research and Applications* **2010**, *18*, 411–433.

[115] *Practical Handbook of Photovoltaics Fundamentals and Applications*, 2. Aufl., (Eds.: A. McEvoy, T. Markvart, L. Castaner), Elsevier professional, **2011**.

[116] M. A. Contreras, M. J. Romero, B. To, F. Hasoon, R. Noufi, S. Ward, K. Ramanathan, *Thin Solid Films* **2002**, *403-404*, 204–211.

[117] D. Abou-Ras, G. Kostorz, A. Romeo, D. Rudmann, A. N. Tiwari, *Thin Solid Films* **2005**, *480-481*, 118–123.

[118] C. Heske, D. Eich, R. Fink, E. Umbach, T. van Buuren, C. Bostedt, L. J. Terminello, S. Kakar, M. M. Grush, T. A. Callcott, F. J. Himpsel, D. L. Ederer, R. C. C. Perera, W. Riedl, F. Karg, *Applied Physics Letters* **1999**, *74*, 1451–1453.

[119] D. Liao, A. Rockett, *Journal of Applied Physics* **2003**, *93*, 9380–9382.

[120] D. Hariskos, S. Spiering, M. Powalla, *Thin Solid Films* **2005**, *480-481*, 99–109.

[121] J. S. Wellings, A. P. Samantilleke, P. Warren, S. N. Heavens, I. M. Dharmadasa, *Semiconductor Science and Technology* **2008**, *23*, 125003.

[122] J. C. Lee, K. H. Kang, S. K. Kim, K. H. Yoon, I. J. Park, J. Song, *Solar Energy Materials and Solar Cells* **2000**, *64*, 185–195.

[123] C. Guillén, J. Herrero, *physica status solidi (a)* **2009**, *206*, 1531–1536.

[124] D. Rudmann, G. Bilger, M. Kaelin, F.-J. Haug, H. Zogg, A. N. Tiwari, *Thin Solid Films* **2003**, *431-432*, 37–40.

[125] P. Salomé, H. Rodriguez-Alvarez, S. Sadewasser, *Solar Energy Materials and Solar Cells* **2015**, *143*, 9–20.

[126] K. Granath, M. Bodegård, L. Stolt, *Solar Energy Materials and Solar Cells* **2000**, *60*, 279–293.

[127] M. A. Contreras, B. Egaas, D. King, A. Swartzlander, T. Dullweber, *Thin Solid Films* **2000**, *361-362*, 167–171.

[128] M. Bodeg Ård, K. Granath, L. Stolt, *Thin Solid Films* **2000**, *361-362*, 9–16.

[129] B. M. Keyes, Hasson, F., Dippo P., Balcioglu, A., Abulfotuh, F., *IEEE Electron Devices Society Staff; IEEE Institute of Electrical and Electronics Engineers Inc. Staff* **1997**.

[130] W. Thongkham, A. Pankiew, K. Yoodee, S. Chatraphorn, *Solar Energy* **2013**, *92*, 189–195.

[131] D. Rudmann, D. Brémaud, A. F. da Cunha, G. Bilger, A. Strohm, M. Kaelin, H. Zogg, A. N. Tiwari, *Thin Solid Films* **2005**, *480-481*, 55–60.

[132] D. Rudmann, A. F. da Cunha, M. Kaelin, F. Kurdesau, H. Zogg, A. N. Tiwari, G. Bilger, *Applied Physics Letters* **2004**, *84*, 1129–1131.

[133] D. Braunger, D. Hariskos, G. Bilger, U. Rau, H. W. Schock, *Thin Solid Films* **2000**, *361-362*, 161–166.

[134] D. W. Niles, M. Al-Jassim, K. Ramanathan, *Journal of Vacuum Science & Technology A: Vacuum Surfaces and Films* **1999**, *17*, 291–296.

[135] A. Rockett, J. S. Britt, T. Gillespie, C. Marshall, M. M. Al Jassim, F. Hasoon, R. Matson, B. Basol, *Thin Solid Films* **2000**, *372*, 212–217.

[136] F. Couzinie-Devy, E. Cadel, N. Barreau, L. Arzel, P. Pareige, *Applied Physics Letters* **2011**, *99*, 232108.

[137] S.-H. Wei, S. B. Zhang, A. Zunger, *Journal of Applied Physics* **1999**, *85*, 7214–7218.

[138] D. W. Niles, K. Ramanathan, F. Hasoon, R. Noufi, B. J. Tielsch, J. E. Fulghum, *Journal of Vacuum Science & Technology A: Vacuum Surfaces and Films* **1997**, *15*, 3044–3049.

[139] L. Kronik, D. Cahen, H. W. Schock, *Advanced Materials* **1998**, *10*, 31–36.

[140] Z.-K. Yuan, S. Chen, Y. Xie, J.-S. Park, H. Xiang, X.-G. Gong, S.-H. Wei, *Advanced Energy Materials* **2016**, *6*, 1601191.

[141] L. E. Oikkonen, M. G. Ganchenkova, A. P. Seitsonen, R. M. Nieminen, *Journal of Applied Physics* **2013**, *114*, 083503.

[142] A. Laemmle, R. Wuerz, T. Schwarz, O. Cojocaru-Mirédin, P.-P. Choi, M. Powalla, *Journal of Applied Physics* **2014**, *115*, 154501.

[143] A. Laemmle, R. Wuerz, M. Powalla, *physica status solidi (RRL) - Rapid Research Letters* **2013**, *7*, 631–634.

[144] T. Lepetit, S. Harel, L. Arzel, G. Ouvrard, N. Barreau, *Progress in Photovoltaics: Research and Applications* **2017**, *25*, 1068–1076.

[145] J. M. Raguse, C. P. Muzzillo, J. R. Sites, L. Mansfield, *IEEE Journal of Photovoltaics* **2017**, *7*, 303–306.

[146] D. Shin, J. Kim, T. Gershon, R. Mankad, M. Hopstaken, S. Guha, B. T. Ahn, B. Shin, *Solar Energy Materials and Solar Cells* **2016**, *157*, 695–702.

[147] C. P. Muzzillo, *Solar Energy Materials and Solar Cells* **2017**, *172*, 18–24.

[148] S. Karki, P. K. Paul, G. Rajan, T. Ashrafee, K. Aryal, P. Pradhan, R. W. Collins, A. Rockett, T. J. Grassman, S. A. Ringel, A. R. Arehart, S. Marsillac, *IEEE Journal of Photovoltaics* **2017**, *7*, 665–669.

[149] I. Khatri, H. Fukai, H. Yamaguchi, M. Sugiyama, T. Nakada, *Solar Energy Materials and Solar Cells* **2016**, *155*, 280–287.

[150] S. A. Jensen, S. Glynn, A. Kanevce, P. Dippo, J. V. Li, D. H. Levi, D. Kuciauskas, *Journal of Applied Physics* **2016**, *120*, 063106.

[151] E. Handick, P. Reinhard, J.-H. Alsmeier, L. Köhler, F. Pianezzi, S. Krause, M. Gorgoi, E. Ikenaga, N. Koch, R. G. Wilks, S. Buecheler, A. N. Tiwari, M. Bär, *ACS applied materials & interfaces* **2015**, *7*, 27414–27420.

[152] P. Reinhard, B. Bissig, F. Pianezzi, E. Avancini, H. Hagendorfer, D. Keller, P. Fuchs, M. Döbeli, C. Vigo, P. Crivelli, S. Nishiwaki, S. Buecheler, A. N. Tiwari, *Chemistry of Materials* **2015**, *27*, 5755–5764.

[153] E. Handick, P. Reinhard, R. G. Wilks, F. Pianezzi, T. Kunze, D. Kreikemeyer-Lorenzo, L. Weinhardt, M. Blum, W. Yang, M. Gorgoi, E. Ikenaga, D. Gerlach, S. Ueda, Y. Yamashita, T. Chikyow, C. Heske, S. Buecheler, A. N. Tiwari, M. Bär, *ACS applied materials & interfaces* **2017**, *9*, 3581–3589.

[154] T. Lepetit, PhD thesis, Universite de Nantes, Nantes, **2015**.

[155] F. Pianezzi, P. Reinhard, A. Chirilă, B. Bissig, S. Nishiwaki, S. Buecheler, A. N. Tiwari, *Physical chemistry chemical physics : PCCP* **2014**, *16*, 8843–8851.

[156] B. Ümsür, W. Calvet, A. Steigert, I. Lauermann, M. Gorgoi, K. Prietzel, D. Greiner, C. A. Kaufmann, T. Unold, M. C. Lux-Steiner, *Physical chemistry chemical physics : PCCP* **2016**, *18*, 14129–14138.

[157] T. M. Friedlmeier, P. Jackson, D. Kreikemeyer-Lorenzo, D. Hauschild, O. Kiowski, D. Hariskos, L. Weinhardt, C. Heske, M. Powalla, *Proceedings of the 26th IEEE Photovoltaic Specialists* **2016**, 457–461.

[158] S. Ishizuka, N. Taguchi, J. Nishinaga, Y. Kamikawa, S. Tanaka, H. Shibata, *The Journal of Physical Chemistry C* **2018**, *122*, 3809–3817.

[159] T. Kodalle, M. D. Heinemann, D. Greiner, H. A. Yetkin, M. Klupsch, C. Li, P. A. van Aken, I. Lauermann, R. Schlatmann, C. A. Kaufmann, *Solar RRL* **2018**, *2*, 1800156.

[160] S. Karki, S. Marsillac, P. Paul, G. Rajan, B. Belfore, D. Poudel, A. Rockett, E. Danilov, F. Castellano, A. Arehart, *IEEE Journal of Photovoltaics* **2019**, *9*, 313–318.

[161] E. Avancini, R. Carron, T. P. Weiss, C. Andres, M. Bürki, C. Schreiner, R. Figi, Y. E. Romanyuk, S. Buecheler, A. N. Tiwari, *Chemistry of Materials* **2017**, *29*, 9695–9704.

[162] M. Malitckaya, H.-P. Komsa, V. Havu, M. J. Puska, *The Journal of Physical Chemistry C* **2017**, *121*, 15516–15528.

[163] T. Kodalle, T. Bertram, R. Schlatmann, C. A. Kaufmann, *IEEE Journal of Photovoltaics* **2019**, *9*, 1839–1845.

[164] T. P. Weiss, S. Nishiwaki, B. Bissig, R. Carron, E. Avancini, J. Löckinger, S. Buecheler, A. N. Tiwari, *Advanced Materials Interfaces* **2018**, *5*, 1701007.

[165] T. Kodalle, L. Choubrac, L. Arzel, R. Schlatmann, N. Barreau, C. A. Kaufmann, *Solar Energy Materials and Solar Cells* **2019**, *200*, 109997.

[166] "Communication from the Commission to the European Parliament, the Council, the European Economic and Social Committee and the Committee of the Regions on the 2017 list of Critical Raw Materials for the EU", **2017**, `https://eur-lex.europa.eu/legal-content/EN/TXT/?uri=CELEX%3A52017DC0490` (visited on 09/07/2020).

[167] S. Chen, X. G. Gong, A. Walsh, S.-H. Wei, *Applied Physics Letters* **2009**, *94*, 041903.

[168] J. Jean, P. R. Brown, R. L. Jaffe, T. Buonassisi, V. Bulović, *Energy & Environmental Science* **2015**, *8*, 1200–1219.

[169] K. Ramasamy, M. A. Malik, P. O'Brien, *Chemical communications (Cambridge England)* **2012**, *48*, 5703–5714.

[170] M. T. Winkler, W. Wang, O. Gunawan, H. J. Hovel, T. K. Todorov, D. B. Mitzi, *Energy & Environmental Science* **2014**, *7*, 1029–1036.

[171] L. P. I.V. Dudchak, *Journal of Alloys and Compounds* **2003**, *351*, 145–150.

[172] I. D. Olekseyuk, I. V. Dudchak, L. V. Piskach, *Journal of Alloys and Compounds* **2004**, *368*, 135–143.

[173] S. Delbos, *EPJ Photovoltaics* **2012**, *3*, 35004.

[174] J. Márquez, M. Neuschitzer, M. Dimitrievska, R. Gunder, S. Haass, M. Werner, Y. E. Romanyuk, S. Schorr, N. M. Pearsall, I. Forbes, *Solar Energy Materials and Solar Cells* **2016**, *144*, 579–585.

[175] K. Sun, C. Yan, F. Liu, J. Huang, F. Zhou, J. A. Stride, M. Green, X. Hao, *Advanced Energy Materials* **2016**, *6*, 1600046.

[176] D. Han, Y. Y. Sun, J. Bang, Y. Y. Zhang, H.-B. Sun, X.-B. Li, S. B. Zhang, *Physical Review B* **2013**, *87*.

[177] A. Nagoya, R. Asahi, R. Wahl, G. Kresse, *Physical Review B* **2010**, *81*.

[178] A. Walsh, S. Chen, S.-H. Wei, X.-G. Gong, *Advanced Energy Materials* **2012**, *2*, 400–409.

[179] S. Chen, J.-H. Yang, X. G. Gong, A. Walsh, S.-H. Wei, *Physical Review B* **2010**, *81*.

[180] S. Siebentritt, S. Schorr, *Progress in Photovoltaics: Research and Applications* **2012**, *20*, 512–519.

[181] S. Schorr, G. Gurieva, M. Guc, M. Dimitrievska, A. Pérez-Rodríguez, V. Izquierdo-Roca, C. S. Schnohr, J. Kim, W. Jo, J. M. Merino, *Journal of Physics: Energy* **2020**, *2*, 012002.

[182] R. Gunder, J. A. Márquez-Prieto, G. Gurieva, T. Unold, S. Schorr, *CrystEngComm* **2018**, *20*, 1491–1498.

[183] G. Gurieva, M. Dimitrievska, S. Zander, A. Pérez-Rodríguez, V. Izquierdo-Roca, S. Schorr, *physica status solidi (c)* **2015**, *12*, 588–591.

[184] L. E. Valle Rios, K. Neldner, G. Gurieva, S. Schorr, *Journal of Alloys and Compounds* **2016**, *657*, 408–413.

[185] G. Gurieva, R. Ferreira, P. Knoll, S. Schorr, *physica status solidi (a)* **2018**, *215*, 1700957.

[186] A. Lafond, L. Choubrac, C. Guillot-Deudon, P. Deniard, S. Jobic, *Zeitschrift für anorganische und allgemeine Chemie* **2012**, *638*, 2571–2577.

[187] G. Gurieva, L. E. Valle Rios, A. Franz, P. Whitfield, S. Schorr, *Journal of Applied Physics* **2018**, *123*, 161519.

[188] K. Kaur, M. Sood, N. Kumar, H. H. Nazari, G. S. Gudavalli, T. P. Dhakal, M. Kumar, *Solar Energy Materials and Solar Cells* **2018**, *179*, 22–30.

[189] M. Kumar, A. Dubey, N. Adhikari, S. Venkatesan, Q. Qiao, *Energy & Environmental Science* **2015**, *8*, 3134–3159.

[190] C. M. Fella, Y. E. Romanyuk, A. N. Tiwari, *Solar Energy Materials and Solar Cells* **2013**, *119*, 276–277.

[191] T. Ericson, J. J. Scragg, A. Hultqvist, J. T. Watjen, P. Szaniawski, T. Torndahl, C. Platzer-Bjorkman, *IEEE Journal of Photovoltaics* **2014**, *4*, 465–469.

[192] D. Hironiwa, N. Matsuo, N. Sakai, T. Katou, H. Sugimoto, J. Chantana, Z. Tang, T. Minemoto, *Japanese Journal of Applied Physics* **2014**, *53*, 106502.

[193] X. Cui, K. Sun, J. Huang, J. S. Yun, C.-Y. Lee, C. Yan, H. Sun, Y. Zhang, C. Xue, K. Eder, L. Yang, J. M. Cairney, J. Seidel, N. J. Ekins-Daukes, M. Green, B. Hoex, X. Hao, *Energy & Environmental Science* **2019**, *12*, 2751–2764.

[194] H. Kim, C. M. Gilmore, A. Piqué, J. S. Horwitz, H. Mattoussi, H. Murata, Z. H. Kafafi, D. B. Chrisey, *Journal of Applied Physics* **1999**, *86*, 6451–6461.

[195] M. S. Grover, P. A. Hersh, H. Q. Chiang, E. S. Kettenring, J. F. Wager, D. A. Keszler, *Journal of Physics D: Applied Physics* **2007**, *40*, 1335–1338.

[196] Y. Chen, *IOP Conference Series: Materials Science and Engineering* **2018**, *423*, 012170.

[197] K. Utsumi, O. Matsunaga, T. Takahata, *Thin Solid Films* **1998**, *334*, 30–34.

[198] C. H. Yi, Y. Shigesato, I. Yasui, S. Takaki, *Japanese Journal of Applied Physics* **1995**, *34*, L244–L247.

[199] Q. Shu, J.-H. Yang, S. Chen, B. Huang, H. Xiang, X.-G. Gong, S.-H. Wei, *Physical Review B* **2013**, *87*.

[200] E. Garcia-Llamas, J. M. Merino, R. Serna, X. Fontané, I. A. Victorov, A. Pérez-Rodríguez, M. León, I. V. Bodnar, V. Izquierdo-Roca, R. Caballero, *Solar Energy Materials and Solar Cells* **2016**, *158*, 147–153.

[201] M. Grossberg, K. Timmo, T. Raadik, E. Kärber, V. Mikli, J. Krustok, *Thin Solid Films* **2015**, *582*, 176–179.

[202] D. B. Khadka, J. Kim, *The Journal of Physical Chemistry C* **2015**, *119*, 1706–1713.

[203] C. J. Hages, S. Levcenco, C. K. Miskin, J. H. Alsmeier, D. Abou-Ras, R. G. Wilks, M. Bär, T. Unold, R. Agrawal, *Progress in Photovoltaics: Research and Applications* **2015**, *23*, 376–384.

[204] S. Kim, K. M. Kim, H. Tampo, H. Shibata, K. Matsubara, S. Niki, *Solar Energy Materials and Solar Cells* **2016**, *144*, 488–492.

[205] S. Kim, K. M. Kim, H. Tampo, H. Shibata, S. Niki, *Applied Physics Express* **2016**, *9*, 102301.

[206] Y. E. Romanyuk, S. G. Haass, S. Giraldo, M. Placidi, D. Tiwari, D. J. Fermin, X. Hao, H. Xin, T. Schnabel, M. Kauk-Kuusik, P. Pistor, S. Lie, L. H. Wong, *Journal of Physics: Energy* **2019**, *1*, 044004.

[207] R. Haight, X. Shao, W. Wang, D. B. Mitzi, *Applied Physics Letters* **2014**, *104*, 033902.

[208] A. L. Ulery, L. R. Drees, *Methods of soil analysis*, Repr, SSSA Soil Science Soc. of America, Madison, Wis., **2012**, 387–463.

[209] R. van Grieken, A. Markowicz, *Handbook of X-ray spectrometry*, 2nd ed., rev. and expanded., Marcel Dekker, New York, **2002**.

[210] E. P. Bertin, *Principles and Practice of X-Ray Spectrometric Analysis*, Second Edition, Springer US, Boston, MA, **1975**.

[211] V. A. Solé, E. Papillon, M. Cotte, P. Walter, J. Susini, *Spectrochimica Acta Part B: Atomic Spectroscopy* **2007**, *62*, 63–68.

[212] Al Thompson and Doug Vaughan, *X-RAY DATA BOOKLET*, **2009**.

[213] M. Newville, *Reviews in Mineralogy and Geochemistry* **2014**, *78*, 33–74.

[214] S. Calvin, *XAFS for Everyone*, CRC Press, Hoboken, **2013**.

[215] L. Chayanun, V. Dagytė, A. Troian, D. Salomon, M. Borgström, J. Wallentin, *Nanotechnology* **2018**, *29*, 454001.

[216] C. Ossig, T. Nietzold, B. West, M. Bertoni, G. Falkenberg, C. G. Schroer, M. E. Stuckelberger, *Journal of visualized experiments : JoVE* **2019**.

[217] M. Stuckelberger, B. West, T. Nietzold, B. Lai, J. M. Maser, V. Rose, M. I. Bertoni, *Journal of Materials Research* **2017**, *32*, 1825–1854.

[218] V. I. Orlov, O. V. Feklisova, E. B. Yakimov, *Solid State Phenomena* **2013**, *205-206*, 142–147.

[219] O. F. Vyvenko, T. Buonassisi, A. A. Istratov, H. Hieslmair, A. C. Thompson, R. Schindler, E. R. Weber, *Journal of Applied Physics* **2002**, *91*, 3614–3617.

[220] O. F. Vyvenko, T. Buonassisi, A. A. Istratov, E. R. Weber, *Journal of Physics: Condensed Matter* **2004**, *16*, 141–151.

[221] C. A. Klein, *Journal of Applied Physics* **1968**, *39*, 2029–2038.

[222] B. M. West, M. Stuckelberger, A. Jeffries, S. Gangam, B. Lai, B. Stripe, J. Maser, V. Rose, S. Vogt, M. I. Bertoni, *Journal of synchrotron radiation* **2017**, *24*, 288–295.

[223] G. Larramona, S. Bourdais, A. Jacob, C. Choné, T. Muto, Y. Cuccaro, B. Delatouche, C. Moisan, D. Péré, G. Dennler, *RSC Adv* **2014**, *4*, 14655–14662.

[224] R. M. Langford, *Microscopy research and technique* **2006**, *69*, 538–549.

[225] P. Schöppe, Friedrich-Schiller-Universität Jena, Jena, **2018**.

[226] P. Schöppe, C. S. Schnohr, M. Oertel, A. Kusch, A. Johannes, S. Eckner, M. Burghammer, G. Martínez-Criado, U. Reislöhner, C. Ronning, *Applied Physics Letters* **2015**, *106*, 013909.

[227] G. Martínez-Criado, J. Villanova, R. Tucoulou, D. Salomon, J.-P. Suuronen, S. Labouré, C. Guilloud, V. Valls, R. Barrett, E. Gagliardini, Y. Dabin, R. Baker, S. Bohic, C. Cohen, J. Morse, *Journal of synchrotron radiation* **2016**, *23*, 344–352.

[228] B. Ravel, M. Newville, *Journal of synchrotron radiation* **2005**, *12*, 537–541.

[229] L. Reimer, *Scanning Electron Microscopy, Physics of Image Formation and Microanalysis*, Second Completely Revised and Updated Edition, Springer Berlin Heidelberg, Berlin, Heidelberg, **1998**.

[230] R. F. Egerton, *Physical Principles of Electron Microscopy, An Introduction to TEM, SEM, and AEM*, Corr. 3. print, Springer Science+Business Media Inc, Boston, MA, **2005**.

[231] S. Martin, H. Berek, C. G. Aneziris, U. Martin, D. Rafaja, *Journal of Applied Crystallography* **2012**, *45*, 1136–1144.

[232] D. Abou-Ras, K. Pantleon, *physica status solidi (RRL) – Rapid Research Letters* **2007**, *1*, 187–189.

[233] A. J. Schwartz, *Electron backscatter diffraction in materials science*, 2. ed., Springer, New York, NY, **2009**.

[234] J. L. Pouchou, F. I. Pichoir, K. F. J. Heinrich, D. E. Newbury, *Electron probe quantitation*, Plenum Press, **1991**.

[235] J. C. Russ, M. A. Frs, R. Kiessling, J. Charles, *Fundamentals of Energy Dispersive X-Ray Analysis, Butterworths Monographs in Materials*, Elsevier Science, Burlington, **1984**.

[236] S. Giraldo, M. Neuschitzer, M. Placidi, P. Pistor, A. Perez-Rodriguez, E. Saucedo, *IEEE Journal of Photovoltaics* **2016**, *6*, 754–759.

[237] M. Neuschitzer, J. Marquez, S. Giraldo, M. Dimitrievska, M. Placidi, I. Forbes, V. Izquierdo-Roca, A. Pérez-Rodriguez, E. Saucedo, *The Journal of Physical Chemistry C* **2016**, *120*, 9661–9670.

[238] B. Shin, Y. Zhu, N. A. Bojarczuk, S. Jay Chey, S. Guha, *Applied Physics Letters* **2012**, *101*, 053903.

[239] A. Fairbrother, X. Fontané, V. Izquierdo-Roca, M. Espíndola-Rodríguez, S. López-Marino, M. Placidi, L. Calvo-Barrio, A. Pérez-Rodríguez, E. Saucedo, *Solar Energy Materials and Solar Cells* **2013**, *112*, 97–105.

[240] S.-Y. Kim, D.-H. Son, Y.-I. Kim, S.-H. Kim, S. Kim, K. Ahn, S.-J. Sung, D.-K. Hwang, K.-J. Yang, J.-K. Kang, D.-H. Kim, *Nano Energy* **2019**, *59*, 399–411.

[241] J. J. Scragg, P. J. Dale, D. Colombara, L. M. Peter, *Chemphyschem : a European journal of chemical physics and physical chemistry* **2012**, *13*, 3035–3046.

[242] S. López-Marino, M. Placidi, A. Pérez-Tomás, J. Llobet, V. Izquierdo-Roca, X. Fontané, A. Fairbrother, M. Espíndola-Rodríguez, D. Sylla, A. Pérez-Rodríguez, E. Saucedo, *Journal of Materials Chemistry A* **2013**, *1*, 8338.

[243] V. Karade, A. Lokhande, P. Babar, M. G. Gang, M. Suryawanshi, P. Patil, J. H. Kim, *Solar Energy Materials and Solar Cells* **2019**, *200*, 109911.

[244] C. J. Hages, A. Redinger, S. Levcenko, H. Hempel, M. J. Koeper, R. Agrawal, D. Greiner, C. A. Kaufmann, T. Unold, *Advanced Energy Materials* **2017**, *7*, 1700167.

[245] T. Thersleff, S. Giraldo, M. Neuschitzer, P. Pistor, E. Saucedo, K. Leifer, *Materials & Design* **2017**, *122*, 102–109.

[246] T. Gokmen, O. Gunawan, T. K. Todorov, D. B. Mitzi, *Applied Physics Letters* **2013**, *103*, 103506.

[247] J. J. S. Scragg, J. K. Larsen, M. Kumar, C. Persson, J. Sendler, S. Siebentritt, C. Platzer Björkman, *physica status solidi (b)* **2016**, *253*, 247–254.

[248] M. Paris, L. Choubrac, A. Lafond, C. Guillot-Deudon, S. Jobic, *Inorganic chemistry* **2014**, *53*, 8646–8653.

[249] G. Rey, G. Larramona, S. Bourdais, C. Choné, B. Delatouche, A. Jacob, G. Dennler, S. Siebentritt, *Solar Energy Materials and Solar Cells* **2018**, *179*, 142–151.

[250] S. Schorr, *Solar Energy Materials and Solar Cells* **2011**, *95*, 1482–1488.

[251] M. Neuschitzer, Y. Sanchez, T. Olar, T. Thersleff, S. Lopez-Marino, F. Oliva, M. Espindola-Rodriguez, H. Xie, M. Placidi, V. Izquierdo-Roca, I. Lauermann, K. Leifer, A. Pérez-Rodriguez, E. Saucedo, *Chemistry of Materials* **2015**, *27*, 5279–5287.

[252] S. López-Marino, Y. Sánchez, M. Placidi, A. Fairbrother, M. Espindola-Rodríguez, X. Fontané, V. Izquierdo-Roca, J. López-García, L. Calvo-Barrio, A. Pérez-Rodríguez, E. Saucedo, *Chemistry (Weinheim an der Bergstrasse Germany)* **2013**, *19*, 14814–14822.

[253] A. Fairbrother, X. Fontané, V. Izquierdo-Roca, M. Placidi, D. Sylla, M. Espindola-Rodriguez, S. López-Mariño, F. A. Pulgarín, O. Vigil-Galán, A. Pérez-Rodríguez, E. Saucedo, *Progress in Photovoltaics: Research and Applications* **2014**, *22*, 479–487.

[254] A. Fairbrother, E. García-Hemme, V. Izquierdo-Roca, X. Fontané, F. A. Pulgarín-Agudelo, O. Vigil-Galán, A. Pérez-Rodríguez, E. Saucedo, *Journal of the American Chemical Society* **2012**, *134*, 8018–8021.

[255] J. Timo Wätjen, J. Engman, M. Edoff, C. Platzer-Björkman, *Applied Physics Letters* **2012**, *100*, 173510.

[256] N. Vora, J. Blackburn, I. Repins, C. Beall, B. To, J. Pankow, G. Teeter, M. Young, R. Noufi, *Journal of Vacuum Science & Technology A: Vacuum Surfaces and Films* **2012**, *30*, 051201.

[257] M. Ganchev, J. Iljina, L. Kaupmees, T. Raadik, O. Volobujeva, A. Mere, M. Altosaar, J. Raudoja, E. Mellikov, *Thin Solid Films* **2011**, *519*, 7394–7398.

[258] W.-C. Hsu, I. Repins, C. Beall, C. DeHart, B. To, W. Yang, Y. Yang, R. Noufi, *Progress in Photovoltaics: Research and Applications* **2014**, *22*, 35–43.

[259] A. Redinger, K. Hönes, X. Fontané, V. Izquierdo-Roca, E. Saucedo, N. Valle, A. Pérez-Rodríguez, S. Siebentritt, *Applied Physics Letters* **2011**, *98*, 101907.

[260] A. Redinger, S. Siebentritt, *Applied Physics Letters* **2010**, *97*, 092111.

[261] T. Taskesen, J. Neerken, J. Schoneberg, D. Pareek, V. Steininger, J. Parisi, L. Gütay, *Advanced Energy Materials* **2018**, *8*, 1703295.

[262] M. Neuschitzer, M. E. Rodriguez, M. Guc, J. A. Marquez, S. Giraldo, I. Forbes, A. Perez-Rodriguez, E. Saucedo, *Journal of Materials Chemistry A* **2018**, *6*, 11759–11772.

[263] S. Giraldo, S. Kim, J. A. Andrade–Arvizu, X. Alcobé, C. Malerba, M. Valentini, H. Tampo, H. Shibata, V. Izquierdo–Roca, A. Pérez–Rodríguez, E. Saucedo, *Progress in Photovoltaics: Research and Applications* **2019**, *27*, 779–788.

[264] D. A. R. Barkhouse, O. Gunawan, T. Gokmen, T. K. Todorov, D. B. Mitzi, *Progress in Photovoltaics: Research and Applications* **2012**, *20*, 6–11.

[265] O. Gunawan, T. K. Todorov, D. B. Mitzi, *Applied Physics Letters* **2010**, *97*, 233506.

[266] J. J. Scragg, T. Ericson, X. Fontané, V. Izquierdo-Roca, A. Pérez-Rodríguez, T. Kubart, M. Edoff, C. Platzer-Björkman, *Progress in Photovoltaics: Research and Applications* **2014**, *22*, 10–17.

[267] K. Sardashti, R. Haight, T. Gokmen, W. Wang, L.-Y. Chang, D. B. Mitzi, A. C. Kummel, *Advanced Energy Materials* **2015**, *5*, 1402180.

[268] S. Bag, O. Gunawan, T. Gokmen, Y. Zhu, T. K. Todorov, D. B. Mitzi, *Energy & Environmental Science* **2012**, *5*, 7060.

[269] L. Guo, Y. Zhu, O. Gunawan, T. Gokmen, V. R. Deline, S. Ahmed, L. T. Romankiw, H. Deligianni, *Progress in Photovoltaics: Research and Applications* **2014**, *22*, 58–68.

[270] E. Ojeda-Durán, K. Monfil-Leyva, J. Andrade-Arvizu, I. Becerril-Romero, Y. Sánchez, R. Fonoll-Rubio, M. Guc, Z. Jehl, J. A. Luna-López, A. L. Muñoz-Zurita, J. La Hernández-de Luz, V. Izquierdo-Roca, M. Placidi, E. Saucedo, *Solar Energy* **2020**, *198*, 696–703.

[271] J. Kim, S. Park, S. Ryu, J. Oh, B. Shin, *Progress in Photovoltaics: Research and Applications* **2017**, *25*, 308–317.

[272] M. E. Erkan, V. Chawla, M. A. Scarpulla, *Journal of Applied Physics* **2016**, *119*, 194504.

[273] H. Tampo, S. Kim, T. Nagai, H. Shibata, S. Niki, *ACS applied materials & interfaces* **2019**, *11*, 13319–13325.

[274] S. Wang, S. Gao, D. Wang, Z. Jiang, J. Ao, Z. Zhou, S. Liu, Y. Sun, Y. Zhang, *Solar RRL* **2019**, *3*, 1800236.

[275] A. Somogyi, M. Drakopoulos, L. Vincze, B. Vekemans, C. Camerani, K. Janssens, A. Snigirev, F. Adams, *X-Ray Spectrometry* **2001**, *30*, 242–252.

[276] O. Engler, V. Randle, *Introduction to texture analysis, Macrotexture, microtexture, and orientation mapping*, 2. ed., CRC Press, Boca Raton, Fla., **2010**.

[277] H.-R. Wenk, *Preferred orientation in deformed metals and rocks, An introduction to modern texture analysis*, Academic Press, Orlando, **1985**.

[278] D. Abou-Ras, S. Schorr, H. W. Schock, *Journal of Applied Crystallography* **2007**, *40*, 841–848.

[279] W. Wisniewski, S. Saager, A. Böbenroth, C. Rüssel, *Ultramicroscopy* **2017**, *173*, 1–9.

[280] M. Morihama, F. Gao, T. Maeda, T. Wada, *Japanese Journal of Applied Physics* **2014**, *53*.

[281] M. J. Ward, P. A. Rupar, M. W. Murphy, Y.-M. Yiu, K. M. Baines, T. K. Sham, *Chemical communications (Cambridge England)* **2010**, *46*, 7016–7018.

[282] Weiqing Zhou, Michael Paesler, and Dale E. Sayers.

[283] A. Johannes, D. Salomon, G. Martinez-Criado, M. Glaser, A. Lugstein, C. Ronning, *Science advances* **2017**, *3*, eaao4044.

[284] O. Majérus, L. Cormier, J.-P. Itié, L. Galoisy, D. R. Neuville, G. Calas, *Journal of Non-Crystalline Solids* **2004**, *345-346*, 34–38.

[285] M. Backman, F. Djurabekova, O. H. Pakarinen, K. Nordlund, L. L. Araujo, M. C. Ridgway, *Physical Review B* **2009**, *80*, 795.

[286] V. V. Atuchin, V. v. Kaichev, I. v. Korolkov, A. A. Saraev, I. B. Troitskaia, T. v. Perevalov, V. A. Gritsenko, *The Journal of Physical Chemistry C* **2014**, *118*, 3644–3650.

[287] Sevik, Cem and Bulutay, Ceyhun, *Journal of Materials Science* **2007**, *42*, 6555–6565.

[288] C. V. Ramana, G. Carbajal-Franco, R. S. Vemuri, I. B. Troitskaia, S. A. Gromilov, V. V. Atuchin, *Materials Science and Engineering: B* **2010**, *174*, 279–284.

[289] M. Zhou, L. Shao, L. Miao, *The Journal of Physical Chemistry A* **2002**, *106*, 6483–6486.

[290] S. Adachi, *Earth-abundant materials for solar cells, Cu2-II-IV-VI4 semiconductors*, John Wiley & Sons Inc, Chichester, West Sussex, United Kingdom, **2015**.

[291] A. Kanevce, I. Repins, S.-H. Wei, *Solar Energy Materials and Solar Cells* **2015**, *133*, 119–125.

[292] J. Timo Wätjen, J. J. Scragg, M. Edoff, S. Rubino, C. Platzer-Björkman, *Applied Physics Letters* **2013**, *102*, 051902.

[293] K. Wang, B. Shin, K. B. Reuter, T. Todorov, D. B. Mitzi, S. Guha, *Applied Physics Letters* **2011**, *98*, 051912.

[294] G. Larramona, S. Bourdais, A. Jacob, C. Choné, T. Muto, Y. Cuccaro, B. Delatouche, C. Moisan, D. Péré, G. Dennler, *The journal of physical chemistry letters* **2014**, *5*, 3763–3767.

[295] K. Woo, Y. Kim, W. Yang, K. Kim, I. Kim, Y. Oh, J. Y. Kim, J. Moon, *Scientific reports* **2013**, *3*, 3069.

[296] J. Just, D. Lützenkirchen-Hecht, R. Frahm, S. Schorr, T. Unold, *Applied Physics Letters* **2011**, *99*, 262105.

[297] *Springer Handbook of Electronic and Photonic Materials*, 2nd Edition, (Eds.: S. Kasap, P. Capper), Springer International Publishing, Cham, **2017**.

[298] P. P. Hankare, P. A. Chate, D. J. Sathe, P. A. Chavan, V. M. Bhuse, *Journal of Materials Science: Materials in Electronics* **2009**, *20*, 374–379.

[299] W. Li, J. Chen, C. Yan, X. Hao, *Journal of Alloys and Compounds* **2015**, *632*, 178–184.

[300] D. A. R. Barkhouse, R. Haight, N. Sakai, H. Hiroi, H. Sugimoto, D. B. Mitzi, *Applied Physics Letters* **2012**, *100*, 193904.

[301] S. Bourdais, C. Choné, B. Delatouche, A. Jacob, G. Larramona, C. Moisan, A. Lafond, F. Donatini, G. Rey, S. Siebentritt, A. Walsh, G. Dennler, *Advanced Energy Materials* **2016**, *6*, 1502276.

[302] K. E. Roelofs, Q. Guo, S. Subramoney, J. V. Caspar, *Journal of Materials Chemistry A* **2014**, *2*, 13464.

[303] K.-J. Yang, D.-H. Son, S.-J. Sung, J.-H. Sim, Y.-I. Kim, S.-N. Park, D.-H. Jeon, J. Kim, D.-K. Hwang, C.-W. Jeon, D. Nam, H. Cheong, J.-K. Kang, D.-H. Kim, *Journal of Materials Chemistry A* **2016**, *4*, 10151–10158.

[304] D. Abou-Ras, B. Schaffer, M. Schaffer, S. S. Schmidt, R. Caballero, T. Unold, *Physical review letters* **2012**, *108*, 075502.

[305] N. A. Kattan, I. J. Griffiths, D. Cherns, D. J. Fermín, *Nanoscale* **2016**, *8*, 14369–14373.

[306] K. Kaur, K. Arora, B. Behzad, Q. Qiao, M. Kumar, *Nanotechnology* **2019**, *30*, 065706.

[307] T. Kato, J.-L. Wu, Y. Hirai, H. Sugimoto, V. Bermudez, *IEEE Journal of Photovoltaics* **2019**, *9*, 325–330.

[308] D. Kreikemeyer-Lorenzo, D. Hauschild, P. Jackson, T. M. Friedlmeier, D. Hariskos, M. Blum, W. Yang, F. Reinert, M. Powalla, C. Heske, L. Weinhardt, *ACS applied materials & interfaces* **2018**, *10*, 37602–37608.

[309] Y. L. Shabel'nikova, E. B. Yakimov, *Journal of Surface Investigation. X-ray Synchrotron and Neutron Techniques* **2012**, *6*, 894–896.

[310] M. Stuckelberger, T. Nietzold, B. West, B. Lai, J. Maser, V. Rose, M. Bertoni, *2017 IEEE 44th Photovoltaic Specialists Conference (PVSC)* **2017**, 2179–2184.

A. Appendix

The appendix contains additional information, which is not necessary for the understanding of the main part of this thesis. However, the figures and tables shown below provide a valuable contribution for a comprehensive presentation of the results.

A.1 SEM image and EDS intensity maps of the CZTSe reference sample

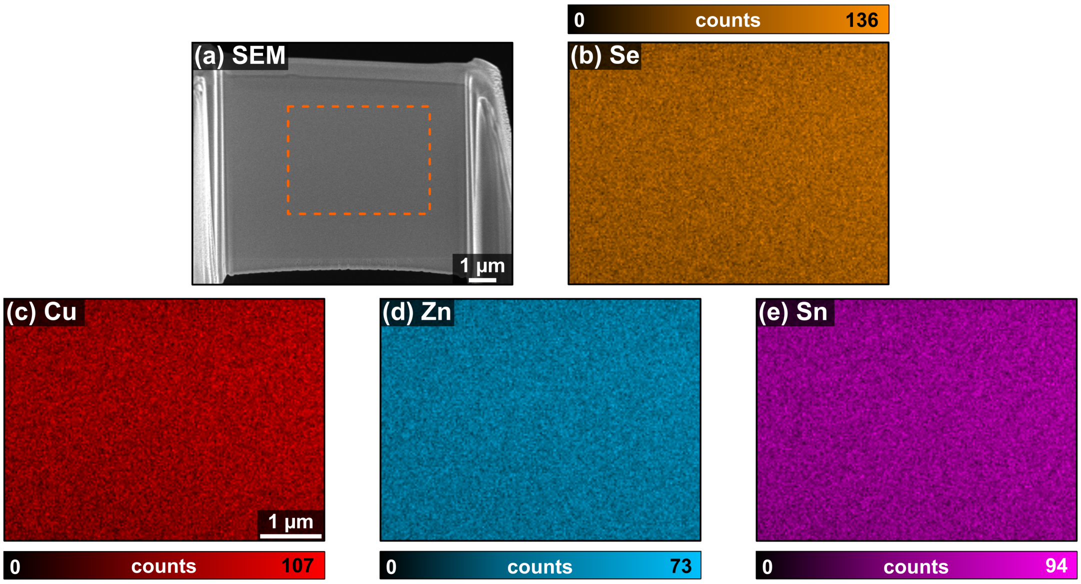

Figure A.1.: SEM image (a), and EDS intensity maps (b-e) of a lamella, taken of a stoichiometric, single-phase powder grain. The orange rectangle in (a) mark the area where EDS measurements were conducted. The average thickness of this lamella was approximately 310 nm.

A.2 SEM image and nano-XRF intensity maps of the CZTSe reference sample

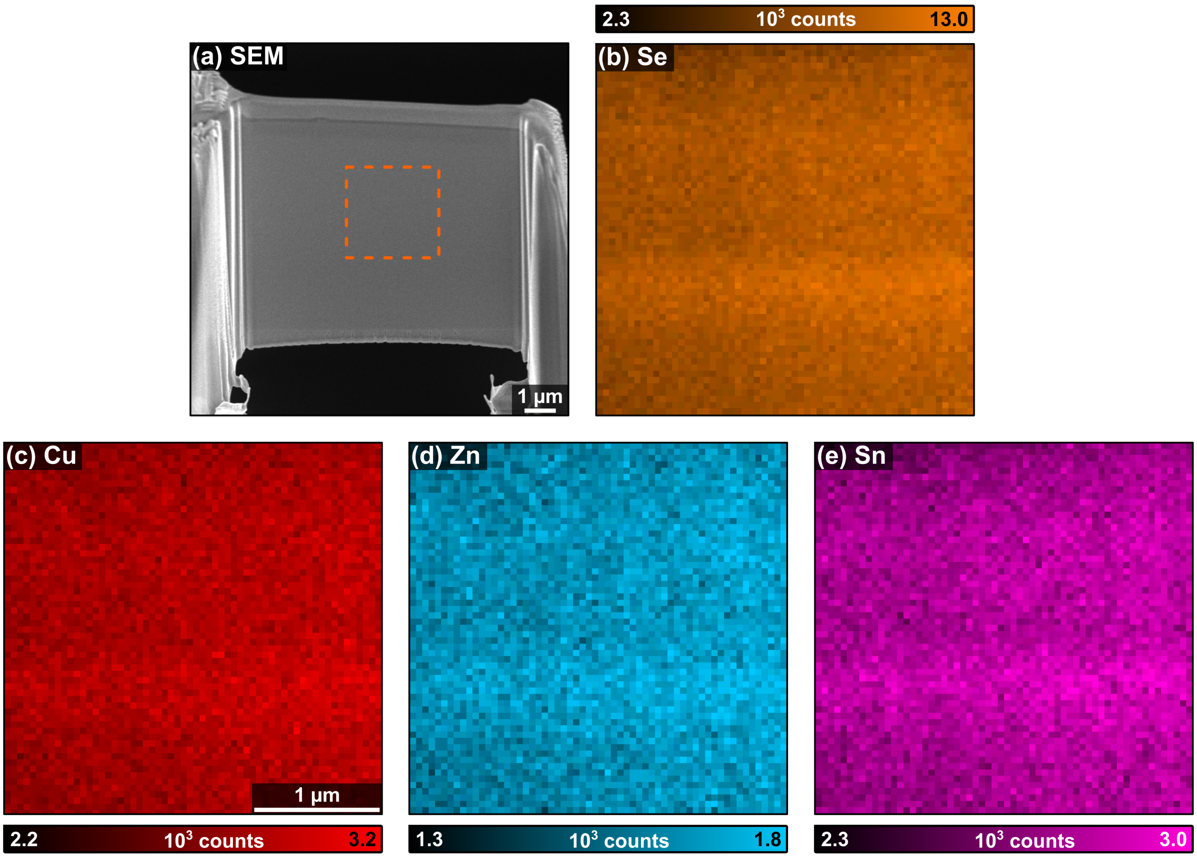

Figure A.2.: SEM image (a), and fitted nano-XRF intensity maps (b-e) of a lamella, taken from a stoichiometric, single-phase powder grain. The orange rectangle in (a) mark the area where XRF measurements were conducted. The average thickness of this lamella was approximately 160 nm.

A.3 Region of interests of AZtec®

Table A.1.: ROI's AZtec® uses to determine the fluorescence intensity of an element.

element	line	ROI energy (keV)
Cu	K_α	7.960 - 8.135
Zn	K_α	8.549 - 8.729
Sn	L_α	3.384 - 3.504
S	K_α	2.255 - 2.360
Se	K_α	11.120 - 11.324
Mo	K_α	2.241 - 2.345
Cd	L_α	3.074 - 3.192
In	L_α	3.224 - 3.346

A.4 SEM image and nano-XRF intensity maps of the CZTSe:Ge solar cell S2

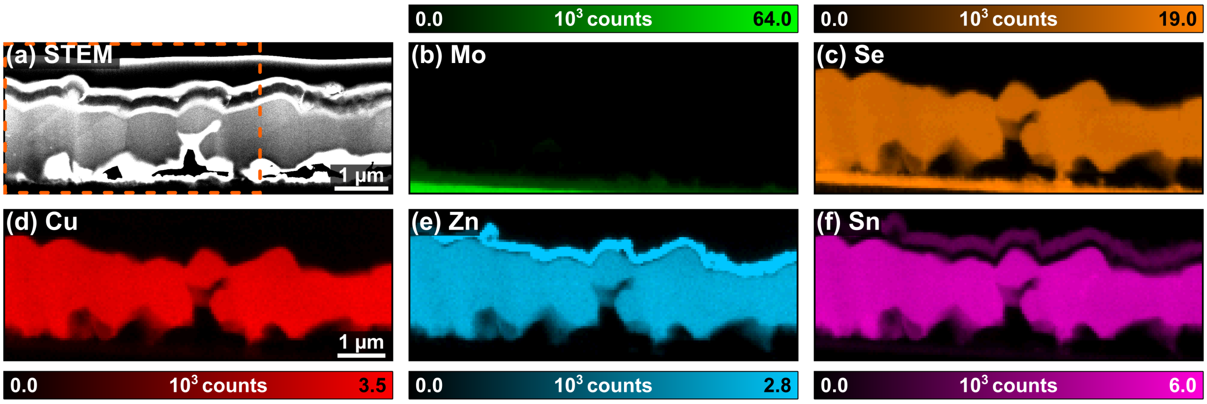

Figure A.3.: STEM-DF image and fitted nano-XRF intensity maps of the Mo back contact (b) and the four absorber elements (c-f) with nominal composition S2. The orange rectangle mark the region which is suited to calculate the relative maps in figure 5.10. The average thickness of this lamella was approximately 260 nm.

A.5 SEM image and nano-XRF intensity maps of the CZTSe:Ge solar cell S3

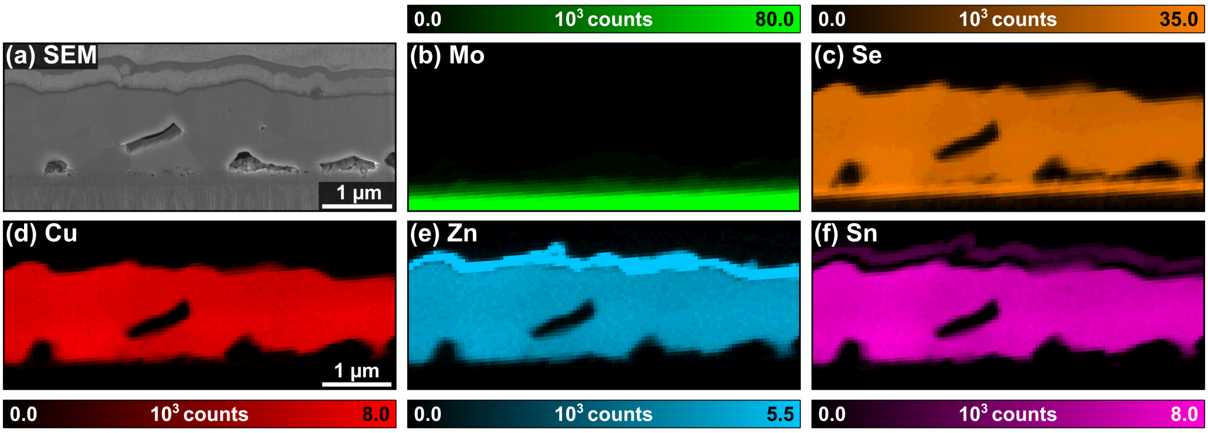

Figure A.4.: SEM image and fitted nano-XRF intensity maps of the Mo back contact (b) and the four absorber elements (c-f) with nominal composition S3. The average thickness of this lamella was approximately 250 nm.

A.6 All-Euler+BC and IPF+BC map taken on the CZTSe:Ge solar cell S1

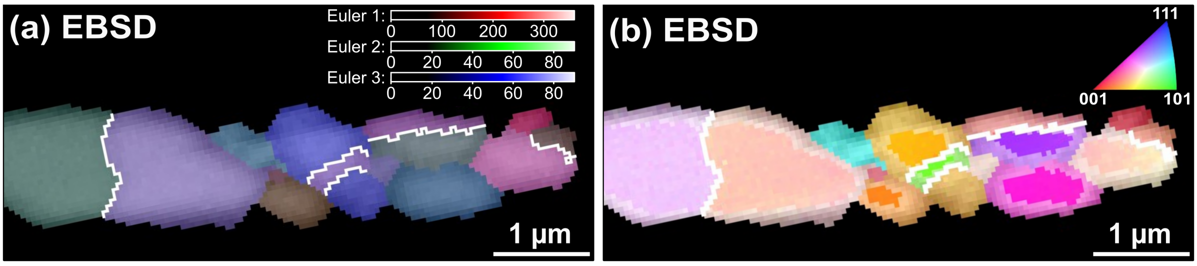

Figure A.5.: (a) all-Euler+BC map obtained from an EBSD scan. The Euler angels of each grain were used to calculated the different grain orientations in (b), where the IPF+BC map is shown. The highly symmetrical Σ3 twin boundaries are highlighted by white lines in both maps.

A.7 Comparison between nano-XRF and EDS measurements

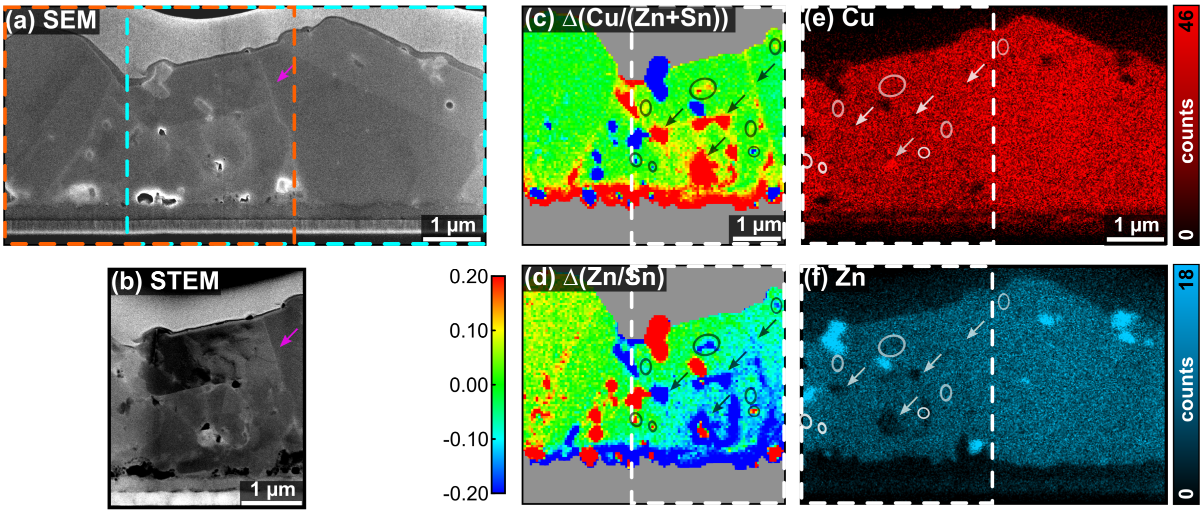

Figure A.6.: (a) SEM image of the same lamella as shown in figure 6.1 and 6.6. The orange and cyan rectangles mark the regions where nano-XRF and EDS measurements were performed. (b) HAADF-STEM image revealing different grain boundaries in the absorber layer. Deviation of the cation ratio from the respective mean value for the Cu/(Zn+Sn) and Zn/Sn ratio (c,d) and EDS intensity maps (e,f). The white rectangle marks the region which was investigated by both techniques, whereas the circles and arrows indicate new features in the deviation maps which are not or not clearly visible in the EDS maps.

A.8 Deviation of the cation atomic concentration of the CZTSSe absorbers C1, C2, and C3

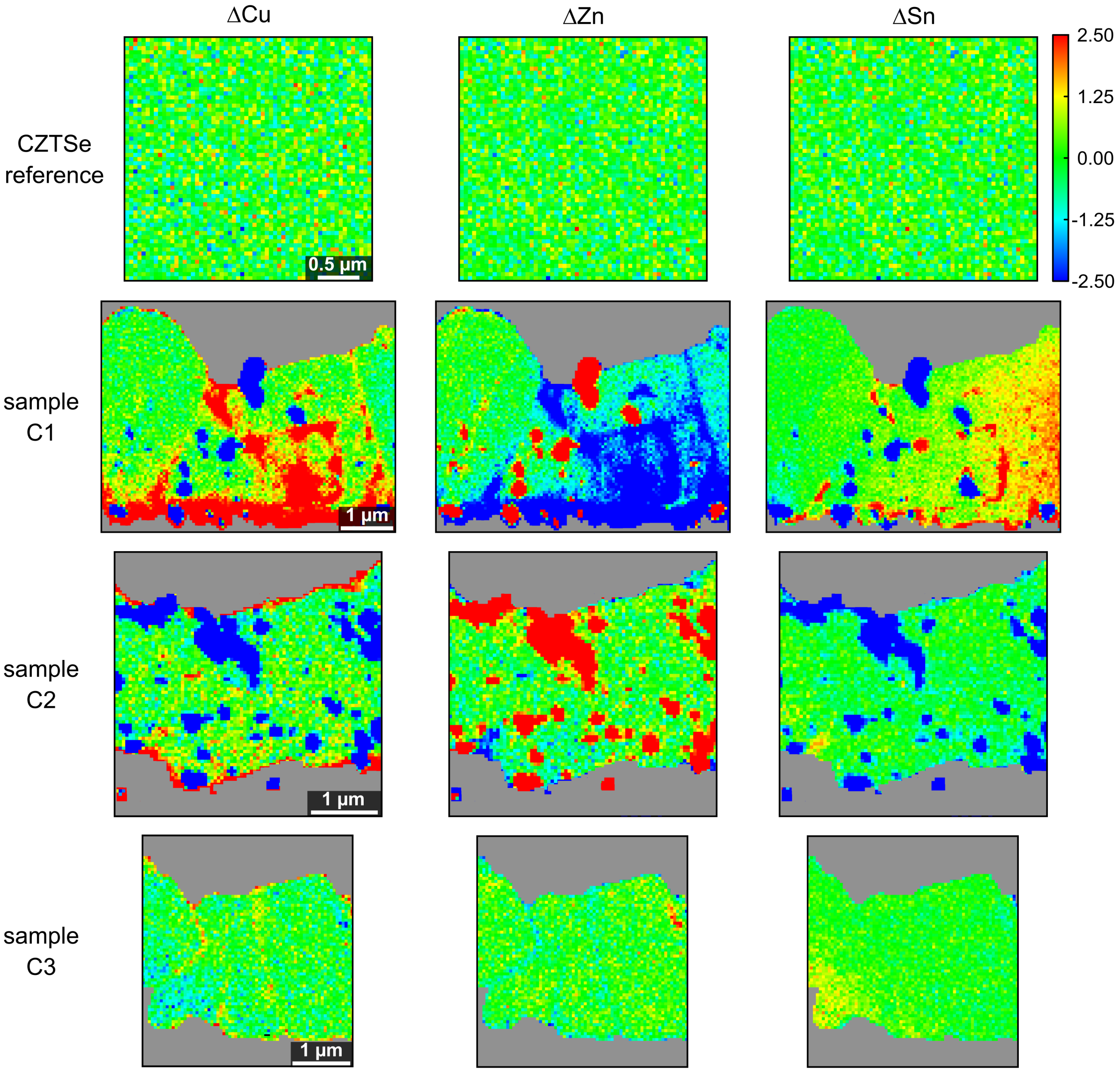

Figure A.7.: Deviation of the cation atomic concentration for Cu, Zn and Sn from the respective mean value. These maps were calculated by subtracting the mean value of a particular map from the actual value of every individual pixel for the CZTSe reference and the three different compositions C1-C3. Here, cation atomic concentration denotes the percentage of a particular cation with respect to all cations, e.g., Cu/(Cu+Zn+Sn). The gray areas mark the regions where no CZTSSe absorber was present, such as the Mo back contact, the Mo-Cu-(S,Se) layer, voids, Pt and air. The color bar is the same for all maps.

A.9 SEM image and nano-XRF intensity maps of the CZTSSe absorber C2

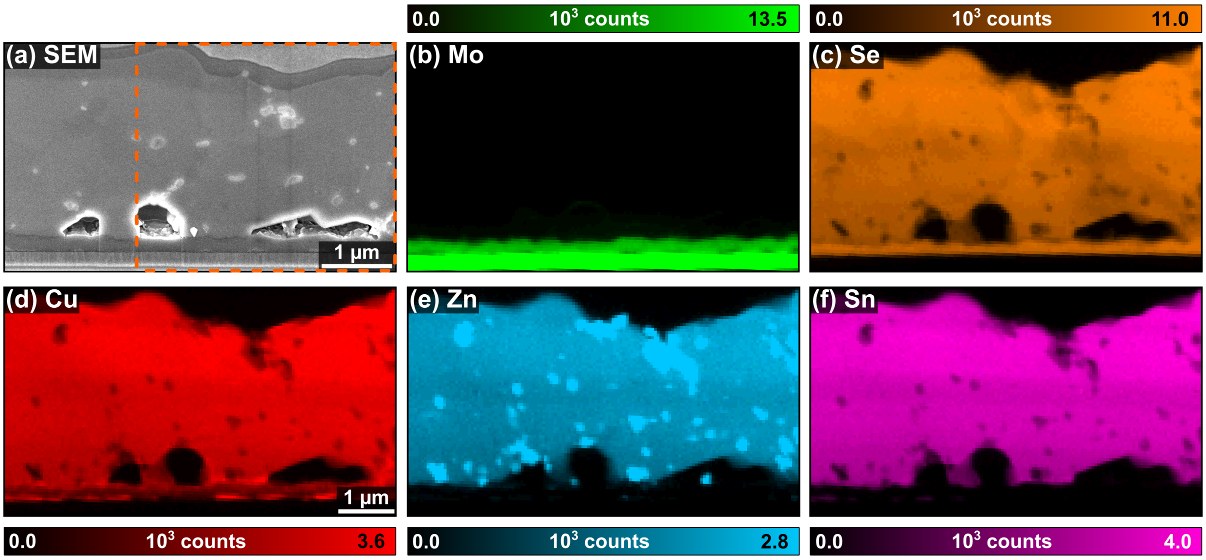

Figure A.8.: SEM image and fitted nano-XRF intensity maps of the Mo back contact (b) and the four absorber elements (c-f) of the same lamella C2 shown in figure 6.3. The orange rectangle mark the region which is suited to calculate the relative maps in figure 6.7.

A.10 SEM image and nano-XRF intensity maps of the CZTSSe absorber C3

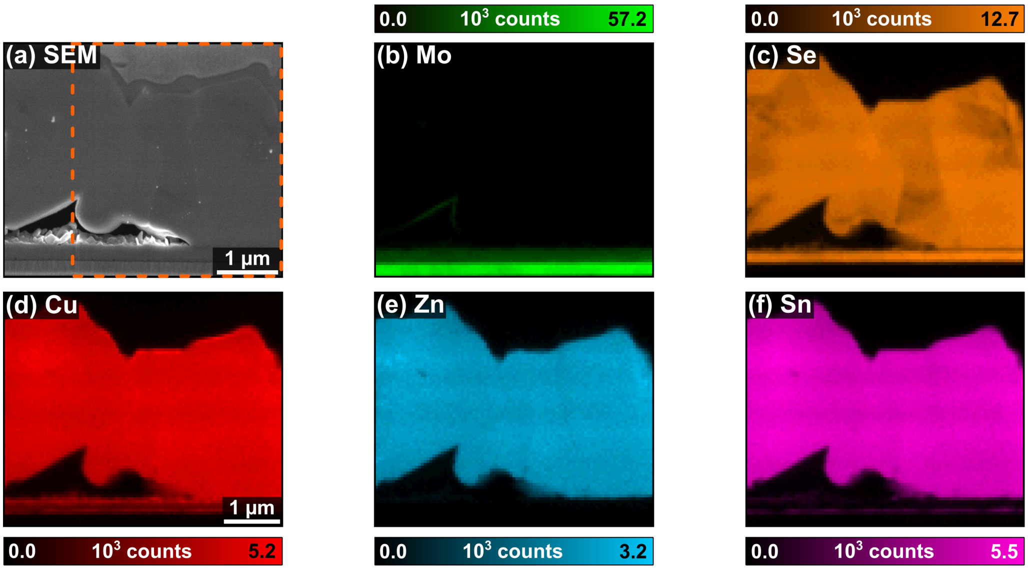

Figure A.9.: SEM image and fitted nano-XRF intensity maps of the Mo back contact (b) and the four absorber elements (c-f) of the same lamella C3 shown in figure 6.4. The orange rectangle mark the region which is suited to calculate the relative maps in figure 6.7.

A.11 Nano-XRF intensity maps and nano-XBIC signal of the RbF post-deposition treated CIGS solar cell

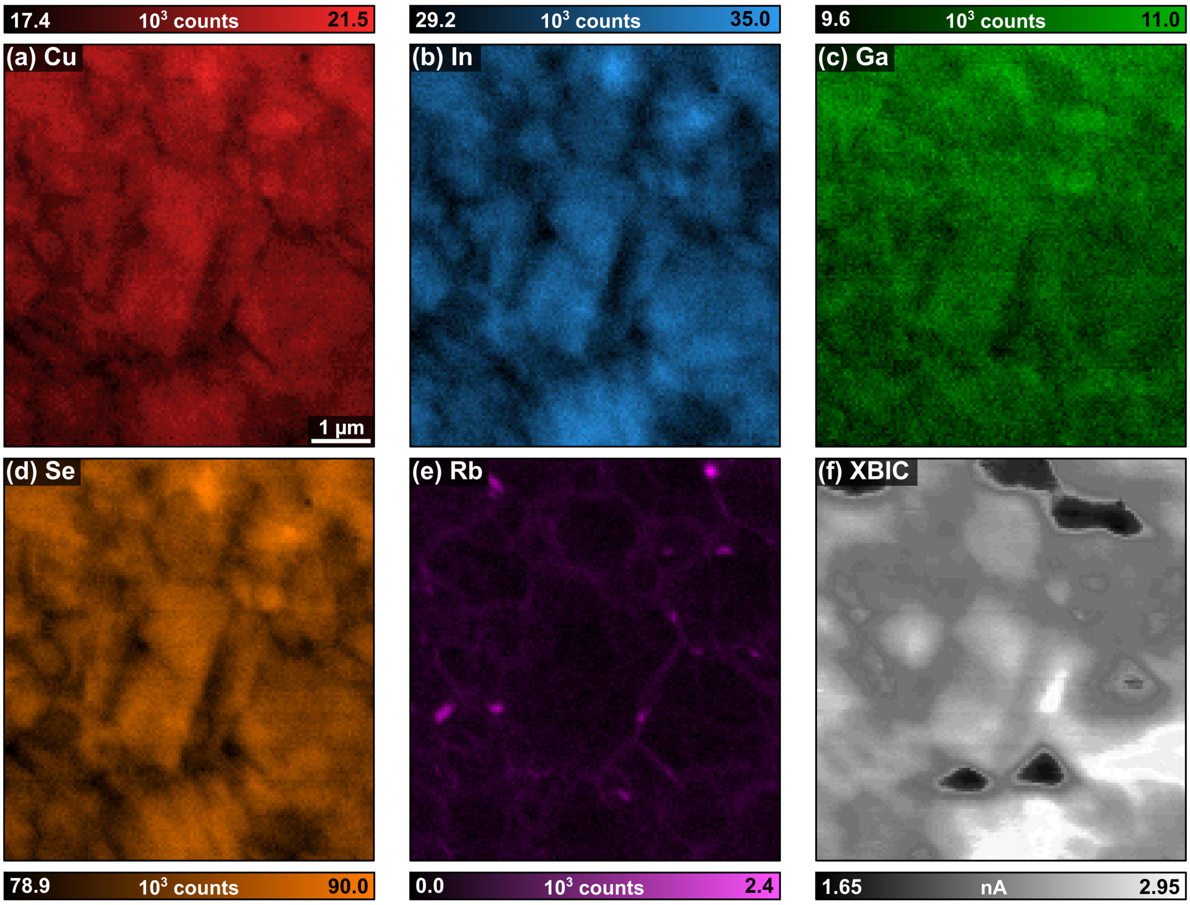

Figure A.10.: Fitted nano-XRF intensity maps of the five absorber elements (a-e) and the simultaneous measured nano-XBIC signal.

B. List of publications

Publications directly related to this thesis

1. M. Ritzer, S. Schönherr, P. Schöppe, W. Wisniewski, S. Giraldo, G. Gurieva, A. Johannes, C. T. Plass, K. Ritter, G. Martínez-Criado, S. Schorr, E. Saucedo, C. Ronning, C. S. Schnohr, On the Germanium Incorporation in $Cu_2ZnSnSe_4$ Kesterite Solar Cells Boosting Their Efficiency. *ACS Applied Energy Materials* **2020**, 3, 558–564.
2. M. Ritzer, S. Schönherr, P. Schöppe, G. Larramona, C. Choné, G. Gurieva, A. Johannes, K. Ritter, G. Martínez-Criado, S. Schorr, C. Ronning, C. S. Schnohr, Interplay of Performance-Limiting Nanoscale Features in $Cu_2ZnSn(S,Se)_4$ Solar Cells. *physica status solidi (a)* **2020**, 2000456.
3. R. Fonoll-Rubio, J. Andrade-Arvizu, J. Blanco-Portals, I. Becerril-Romero, M. Guc, E. Saucedo, F. Peiró, L. Calvo-Barrio, M. Ritzer, C. S. Schnohr, M. Placidi, S. Estradé, V. Izquierdo-Roca, A. Pérez-Rodrígueza, Insights into interface and bulk defects in a high efficiency kesterite-based device. *Energy & Environmental Science* **2021**, 14, 507-523.
4. C. T. Plass, M. Ritzer, P. Schöppe, S. Schönherr, M. Zapf, M. Hafermann, A. Johannes, G. Martínez-Criado, J. Segura-Ruiz, R. Würz, P. Jackson, C. S. Schnohr, C. Ronning, In-operando Nanoscale X-ray Analysis revealing the local electrical properties of Rubidium enriched Grain Boundaries in $Cu(In,Ga)Se_2$ Solar Cells. *ACS Applied Materials & Interfaces* **2020**, 12, 57117-57123.

Further publications

1. P. Schöppe, S. Schönherr, R. Wuerz, W. Wisniewski, G. Martínez-Criado, M. Ritzer, K. Ritter, C. Ronning, C. S, Schnohr. Rubidium segregation at random grain boundaries in Cu(In,Ga)Se_2 absorbers. *Nano Energy* **2017**, 42, 307–313.
2. P. Schöppe, S. Schönherr, P. Jackson, R. Wuerz, W. Wisniewski, M. Ritzer, M. Zapf, A. Johannes, C. S. Schnohr, C. Ronning, Overall Distribution of Rubidium in Highly Efficient Cu(In,Ga)Se_2 Solar Cells. *ACS applied materials & interfaces* **2018**, 10, 40592–40598.
3. A. Johannes, J. Rensberg, T. A. Grünewald, P. Schöppe, M. Ritzer, M. Rosenthal, C. Ronning, M. Burghammer, Determination of the full deformation tensor by multi-Bragg fast scanning nano X-ray diffraction. *Journal of Applied Crystallography* **2020**, 53, 99-106.
4. M. Hafermann, M. Zapf, M. Ritzer, A. Printschler, Y. Luo, A. Ambrosio, W. L. Wilson, C. Ronning, Grayscale Nanopatterning of Phase-Change Materials for Subwavelength-Scaled, Inherently Planar, Nonvolatile, and Reconfigurable Optical Devices. *ACS Applied Nano Materials* **2020**, 3, 4486-4493.
5. P. Schöppe, S. Schönherr, M. Chugh, H. Mirhosseini, P. Jackson, R. Wuerz, M. Ritzer, A. Johannes, G. Martínez-Criado, W. Wisniewski, T. Schwarz, C. T. Plass, M. Hafermann, T. D. Kühne, C. S. Schnohr, C. Ronning, Revealing the origin of the beneficial effect of cesium in highly efficient Cu(In,Ga)Se_2 solar cells. *Nano Energy* **2020**, 71, 104622.
6. A. Schottelius, F. Mambretti, A. Kalinin, B. Beyersdorff, A. Rothkirch, C. Goy, J. Müller, N. Petridis, M. Ritzer, F. Trinter, J. M. Fernández, T. A. Ezquerra, D. E. Galli, R. E. Grisenti, Crystal growth rates in supercooled atomic liquid mixtures. *Nature Materials* **2020**, 19, 512-516.
7. M. Zapf, M. Ritzer, L. Liborius, A. Johannes, M. Hafermann, S. Schönherr, J. Segura-Ruiz, G. Martínez-Criado, W. Prost, C. Ronning, Hot electrons in a nanowire hard X-ray detector. *Nature Communications* **2020**, 11, 1-7.

List of oral and poster presentations

1. Poster: Spatially resolved composition and functionality of thin film solar cells
   EXSA Quantitative Methods in X-ray Spectrometry, Berlin 2017
2. Poster: Spatially resolved composition and functionality of thin film solar cells
   ESRF User Meeting, Grenoble 2018
3. Talk: Compositional inhomogeneity in kesterite thin film solar cell absorbers
   DGP Spring Meeting, Berlin 2018
4. Talk: Compositional inhomogeneity in kesterite absorber layers on a submicrometer scale
   EMRS Spring Meeting, Strasbourg 2018
5. Poster: Spatially resolved composition and functionality of thin film solar cells
   SNI, München 2018
6. Poster: Spatially resolved distribution and structure of Ge in $Cu_2ZnSnSe_4$ thin film solar cells
   ESRF User Meeting, Grenoble 2019
7. Poster: Spatially resolved distribution and structure of Ge in $Cu_2ZnSnSe_4$ thin film solar cells
   ESRF User Meeting, Grenoble 2020

C. Ehrenwörtliche Erklärung

Ich erkläre hiermit ehrenwörtlich, dass ich die vorliegende Arbeit selbständig, ohne unzulässige Hilfe Dritter und ohne Benutzung anderer als der angegebenen Hilfsmittel und Literatur angefertigt habe. Die aus anderen Quellen direkt oder indirekt übernommenen Daten und Konzepte sind unter Angabe der Quelle gekennzeichnet. Bei der Auswahl und Auswertung folgenden Materials haben mir die nachstehend aufgeführten Personen in der jeweils beschriebenen Weise geholfen:

- Die untersuchten Lamellen wurden von Dr. Sven Schönherr präpariert.
- Die EDX Untersuchungen wurden teilweise in Zusammenarbeit mit Dr. Philipp Schöppe durchgeführt.
- Die TEM Bilder wurden am Otto Schott Institut für Materialforschung der FSU Jena von Dr. Philipp Schöppe aufgenommen.
- Die nano-XRF Messungen an Lamellen wurden durch Unterstützung von Dr. Sven Schönherr, Konrad Ritter, Prof. Claudia S. Schnohr, Dr. Andreas Johannes, Dr. Damien Salomon und Dr. Gema Martínez-Criado durchgeführt.
- Das in Kapitel 4 untersuchte CZTSe Pulver und das in Kapitel 5 untersuchte CZGeSe Pulver wurde von Dr. Galina Gurieva in der Gruppe von Prof. Susan Schorr am Helmholtz-Zentrum Berlin für Materialien und Energie hergestellt. Die Zusammensetzung und Phase wurden ebenfalls von Dr. Galina Gurieva bestimmt.
- Die SEM Bilder der CZTSe Referenz wurden von Dr. Sven Schönherr aufgenommen.
- Die in Kapitel 5 untersuchten Ge dotierten CZTSe Solarzellen wurden von Dr. Sergio Giraldo in der Gruppe von Dr. Edgardo Saucedo am Catalonia Institute for Energy Research hergestellt und elektrisch charakterisiert.
- Die nano-XANES Messungen in Kapitel 5 wurden durch Unterstützung von Dr. Sven Schönherr, Christian T. Plass, Dr. Andreas Johannes, Dr. Damien Salomon und Dr. Gema Martínez-Criado durchgeführt.
- Die von Dr. Sven Schönherr präparierten Lamellen in Kapitel 5 wurden von Dr. Philipp Schöppe für die EBSD Messungen gereinigt und für die TEM Messungen ausgedünnt.
- Die EBSD Messungen in Kapitel 5 wurden von Dr. Wolfgang Wisniewski an der Alexander Dubček University in Trenčín durchgeführt und ausgewertet.

- Die SEM und STEM Bilder in Kapitel 5 wurden in Zusammenarbeit mit Dr. Sven Schönherr und Oliver Rüger aufgenommen.
- Die CZTSSe Absorber und Solarzellen in Kapitel 6 wurden von Dr. Gerardo Larramona im Unternehmen IMRA Europe hergestellt und elektrisch charakterisiert.
- Die Auswertung der elektrischen Kenndaten in Kapitel 6 erfolgten teilweise durch Dr. Udo Reislöhner.
- Die SEM und STEM Bilder in Kapitel 6 wurden in Zusammenarbeit mit Dr. Sven Schönherr und Oliver Rüger aufgenommen.
- Die in Kapitel 7 mit RbF nachbehandelte CIGS Solarzelle wurde von Dr. Philip Jackson am Zentrum für Sonnenenergie- und Wasserstoff-Forschung hergestellt und von Dr. Roland Würz zur Verfügung gestellt.
- Die kombinierten nano-XRF und nano-XBIC Messungen wurden durch Unterstützung von Christian Plass, Dr. Sven Schönherr, Dr. Philipp Schöppe, Maximilian Zapf, Martin Hafermann, Dr. Andreas Johannes, Dr. Damien Salomon, Dr. Jaime Segura-Ruiz und Dr. Gema Martínez-Criado durchgeführt.
- Die jeweiligen Koautoren der angeführten Veröffentlichungen (siehe Anhang List of publications) waren an der Interpretation und der Darstellung der Ergebnisse beteiligt.

Weitere Personen waren an der inhaltlich-materiellen Erstellung der vorliegenden Arbeit nicht beteiligt. Insbesondere habe ich hierfür nicht die entgeltliche Hilfe von Vermittlungs- bzw. Beratungsdiensten (Promotionsberater oder andere Personen) in Anspruch genommen. Niemand hat von mir unmittelbar oder mittelbar geldwerte Leistungen für die Arbeiten erhalten, die im Zusammenhang mit dem Inhalt der vorgelegten Dissertation stehen. Die Arbeit wurde bisher weder im In- noch im Ausland in gleicher oder ähnlicher Form einer anderen Prüfungsbehörde vorgelegt. Die geltende Prüfungsordnung der Physikalisch-Astronomischen Fakultät ist mir bekannt. Ich versichere ehrenwörtlich, dass ich nach bestem Wissen die reine Wahrheit gesagt und nichts verschwiegen habe.

Jena, den 11.03.2020

Maurizio Ritzer